Experimental and modelling studies of the adsorption of acetone on ice surfaces at temperatures around 200 K

Dissertation

submitted to

Fachbereich Chemie
University of Duisburg-Essen

in partial fulfilment of the
requirements for a

Doctor of Natural Sciences
(Dr. rer. nat.)

Atanas Terziyski
from
Plovdiv / Bulgaria

March 2006

Acknowledgements

I would like to thank all the people who have helped me on my thesis and my nearly five years' stay in Germany. Time does fly but you all made this period of time the best experience in my life. Especially the people I mention below, without them this thesis will never exist.

I would like to thank Prof. Reinhard Zellner who allowed me to join his group and to carry out this work. I hope my achievements here would be appreciated, although sometimes my English is blurred. I do hope that you could accept my deep respect to you.

I would like to thank Prof. George Andreev, my Bulgarian chief. He is the first person who got the idea of obtaining my Ph.D. degree in Germany, and then began the discussion with Prof. Zellner. He also allowed me to take a quite long leave from my employment at the University of Plovdiv. Prof. Andreev, I think you will be quite satisfied by the result (it is worth to wait for).

And I would also like to thank Dr. Peter Behr, who was my supervisor and was like my father during my stay in Germany. We have become friends before we were colleagues. Thank you Peter for all your help in these years.

I received help from Prof. Anton Iliev (University of Plovdiv) for my theoretical efforts and understanding of the differential equations and Maple. Petar Dimov, a student in University of Dusiburg-Essen (one of my best friends in Germany) helped me with programming and mathematical algorithms. Chelsea Lai, from the same university who read and polished my English, and I also want to mention Ani and Yanka, who provided disinterested support during the years.

Contents

1. Introduction

This introductory chapter is intended to provide general background information related to the present work. It is separated into several chapters each of which aims to present a more detailed literature overview of the topic, as well as our motivation for the relevance to it.

1.1. Heterogeneous processes in the atmosphere

Studies of the interaction of atmospheric trace gases with surfaces have become an important subject of atmospheric chemistry ever since the discovery of larger regional atmospheric changes such as the springtime Antarctic ozone hole (Crutzen and Lelieveld, 2001; Farman, 1985; Lelieveld et al., 1999; Solomon, 1999) or tropospheric ozone depletion in the Artic (Lorenzen-Schmidt et al., 1998; Platt and Honninger, 2003; Wessel et al., 1998). The characteristics of each of these events is the rapid change of gas phase chemical composition due to the adsorption and chemical reaction of halogen and/or nitrogen containing trace gases with the surfaces of liquid or solid particles leading to the release of so called activated trace gases which upon submission to solar radiation are transferred into ozone depleting free radicals (Zellner, 1999).

The rates of heterogeneous reactions in the atmosphere are generally expressed by a collision number with the available surface area multiplied by a reactive uptake coefficient. The latter is a composite of all individual processes that are sequentially encountered in a heterogeneous reaction, i.e. adsorption, thermal equilibration, desorption, surface reaction, phase boundary transition and bulk reaction (Dankwerts, 1951; Kolb, 1995). The concept of a reactive uptake coefficient is driven by experimental studies since it is this quantity which can be determined by selected experimental techniques using either analysis of the gas or the condensed phase (Kolb,

1995; Zondlo et al., 1998). The separation of the individual elementary processes of a reactive uptake coefficient has only been possible in selective cases (Behr et al., 2001; Nathanson et al., 1996; Rudich, 1996; Wagner, 2004). Moreover, the theoretical framework has just begun to be developed (Galashev et al., 2002; Marx, 2000; Slovak et al., 2003).

An important part of heterogeneous interaction in the atmosphere, apart from chemical reaction, is the adsorption of trace gases on surfaces. The extent to which this may occur depends on the amount of surface area available and the strength of the interaction, i.e. the adsorption enthalpies.

1.2. Importance of ice surfaces

In recent years ice surfaces in the atmosphere have received considerable attention. The reason is that these surfaces are more common than hitherto expected and that they may play an important role in some of the reactive trace gas modifications encountered in large scale perturbations of atmospheric chemical composition. Ice surfaces occur as polar stratospheric clouds (PSCs) at temperatures below the lower stratospheric frost point (Fahey, 1989; Larsen et al., 2002; Toon, 1989) in the form of cirrus clouds (Pruppacher and Klett, 1996; Seinfeld, 1998) as well as condensation trails (contrails) of commercial jet aircraft (Gierens, 2003; Gleitsmann and Zellner, 1998) both at temperatures in the regime 190 – 220 K as appropriate to the upper troposphere / lower stratosphere (Seinfeld, 1998). Moreover, ice surfaces are generated regularly during strong precipitation events of thunderstorms where rapid vertical motions of air masses lead to super cooling events in which ice nucleation becomes the favourite form of condensation (Blyth et al., 2001; Dash and Wettlaufer, 2003).

As a result of their increased importance, studies of chemical reactions and adsorption on ice surfaces have received substantial interest. This interest focuses on reactive uptake coefficient on one hand (see review by Abbatt, (Abbatt, 2003)) as well as on the kinetics and thermodynamics of adsorption processes. The latter have recently been suggested to impact on oxygenated trace gases such as CH_2O, CH_3OH, C_2H_5OH, CH_3COCH_3 and others due to the

expected strong interactions with ice surfaces at the low temperatures of the UTLS region and because of the occurrence of these compounds at surprisingly high concentrations in this part of the atmosphere (Arnold et al., 1997; Singh et al., 2000). Since such compounds are expected to impact on the concentration levels of the HOx oxidation system (Bedjanian and Poulet, 2003; Jaegle, 2001; Mckeen et al., 1997), investigations of their phase partitioning are important prerequisites of the assessment of their atmospheric chemical behaviours.

Studies of gas adsorption on surfaces have a long tradition (Duke, 1994; Ertl, 1991), both on well defined and well characterized surfaces in ultra-low pressure systems (Lass, 2004; Wang, 2003; Zambelli, 1997) as well as on real surfaces with largely undefined surface properties (Grassian, 2001; Groen, 2003; Reinhardt, 2003). The aims of studies in each case, however, are largely identical with the focus being on the thermodynamics of adsorption (adsorption enthalpies, Langmuir constants, fractional surface coverages) as well as on kinetic quantities such as adsorption and desorption rate constants. More recently dynamical studies on surface collisions such as energy thermalization and dissipation (Isakson and Sitz, 1999; Klassen et al., 1997) as well as dynamic residence time studies (Behr et al., 2001; Ertl, 1991; Morris et al., 2000) have been added to the list of approaches to investigate surface / gas interactions. Needless to say that important contributions have also been provided by molecular configurational studies of adsorbat / surface structures using different levels of theory (Girardet and Toubin, 2001; Picaud and Hoang, 2000).

Ice surfaces represent a special kind of surface due to their relatively high vapour pressure. Under equilibrium conditions with the vapour phase ice surfaces are extremely dynamic with simultaneous condensation and evaporation events. This is particularly the case at temperatures above 200 K, where desorption of water molecules is sufficiently rapid. As a consequence, in this temperature region ice surfaces are constantly renewed and the

adsorption of trace gases occurs simultaneously with adsorbing and desorbing water molecules. Only at extremely low temperatures where the rate of desorption of water is low, ice surfaces become more stable and adsorption of trace gases occurs without simultaneous water condensation.

The uptake of atmospheric pollutants on ice surfaces has been extensively studied during the last years. However uptake coefficients and surface coverage reported from different groups are not in a good agreement and may differ by an order of magnitude i.e. HCl uptake on ice in temperature range 90-210K (Hanson, 1992; Abbatt, 1992; Leu et al., 1997b; Liang T. Chu, 1993). This shows that surface roughness and ice preparation may play an important role and influences the measured uptake coefficient.

Under these conditions ice surfaces have been found to be polycrystalline (Petrenko and Whitworth, 1999) with cubic (I_c) and hexagonal (I_h) ice being the most relevant structures. Both phases have very similar physical properties, i.e. density and interatomic distances (Hobbs, 1974; Dowell and Rinfret, 1960). However, cubic ice is a metastable phase which tends to transform into the thermodynamically stable hexagonal phase on a time scale of several 10 minutes at temperatures around 200 K (Chaix et al., 1998; Davy and Somorjai, 1971; Keyser and Leu, 1993; Dowell and Rinfret, 1960; Kumai, 1968).

1.3.   Experimental studies of gas uptake on ice surfaces

Adsorption studies on ice surfaces have frequently been performed in coated wall tube reactors (Behr et al., 2004; Journet et al., 2005; Sokolov, 2002; Winkler et al., 2002). The advantage of this technique is that, in addition to adsorption equilibrium, the exposure time can be varied and hence adsorption rate coefficients can also be determined. Moreover, the interaction of the gas phase with the surface can be kept kinetically controlled and is not diffusion limited, at least in the low pressure operational mode (Howard, 1979). It has been found (Behr et al., 2003; Winkler et al., 2002), that temporal profiles of gas phase components show complex shapes due to the interaction of adsorption and desorption processes. As a result the derivation of

thermodynamic and kinetic data is complicated and an un-biased theoretical framework is called for to facilitate such analysis.

Other methods, such as Knudsen cells (Hudson et al., 2002), volumetric (Domine and Rey-Hanot, 2002) and chromatographic (Guimbaud et al., 2003) are equally applicable for adsorption studies of acetone on ice. The Knudsen cell technique has been first described by Golden et al. (1973) and has been used in recent years to study the kinetics of chemical reactions of a wide variety of systems. The advantage of this technique is that it operates at very low pressures where collisions in the gas phase can be excluded. It is assumed that the measured signal is a result of heterogeneous interactions with the sample only. Chromatography in combination with QMS is a new and very sensitive technique which allows measurements under high pressure i.e. conditions closer to those in the atmosphere.

1.4. Motivation of present work

Ammann's group (Bartels-Rausch et al., 2005) have developed a kinetic model for adsorption of acetone on ice in coated flow tube reactors using a Monte Carlo simulation. Their model produces some discrepancies between measured and simulated data at low temperatures which they assign to changes of the ice structure. Another kinetic model has recently been published (Cox et al., 2005). These authors simulated adsorption processes of HNO_3 and HCl on ice in a flow tube reactor by a kinetic model powered by the Facsimile program.

In this thesis a model to derive kinetic and thermodynamic data of adsorption experiments in tubular flow reactors is presented. To our knowledge the effect of changing the adsorption capacity for acetone adsorption on ice surfaces as a result of ageing has not been reported before. We explain the higher adsorption rates at low temperature and for fresh ice with the presence of more cubic sites than at high temperatures and for aged ice i.e. the simple Langmuir model is not applicable in such cases. With the help of the model

we can extract kinetic parameters which describe our processes in terms of rate coefficients and maximal number of surface sites. Moreover, it is suggested that the ageing effect of the ice surfaces is due to the transformation of cubic to hexagonal ice structures. This process changes the total adsorption rate of acetone on ice by more than a factor of two. Together with the dependence of adsorption capacity on the ice thickness (Leu et al., 1997a) we provide a complete kinetic and thermodynamic overview of acetone adsorption on ice surfaces in the temperature range 190 to 230 K.

2. Experimental setup

The heterogeneous adsorption of acetone on ice surfaces has been studied in a coated wall flow tube reactor (CWFT) with quadruple mass spectrometry (QMS) as a detection method of the gaseous species at the end of the reactor tube.

The flow tube reactor consists of a stainless steel coated flow tube with inner diameter of 24mm and total length of 60 cm. A mixture of methanol and ethanol with mixing ratio 1:1 was used as a cooling liquid. A differential pumping technique, which reduces the pressure from typically 1 to 5 mbar in the flow system to less than 10^{-6} mbar in the mass chamber spectrometer was applied. The lowest accessible temperature is around 188 K using an Ultra Kryomat Lauda 90.

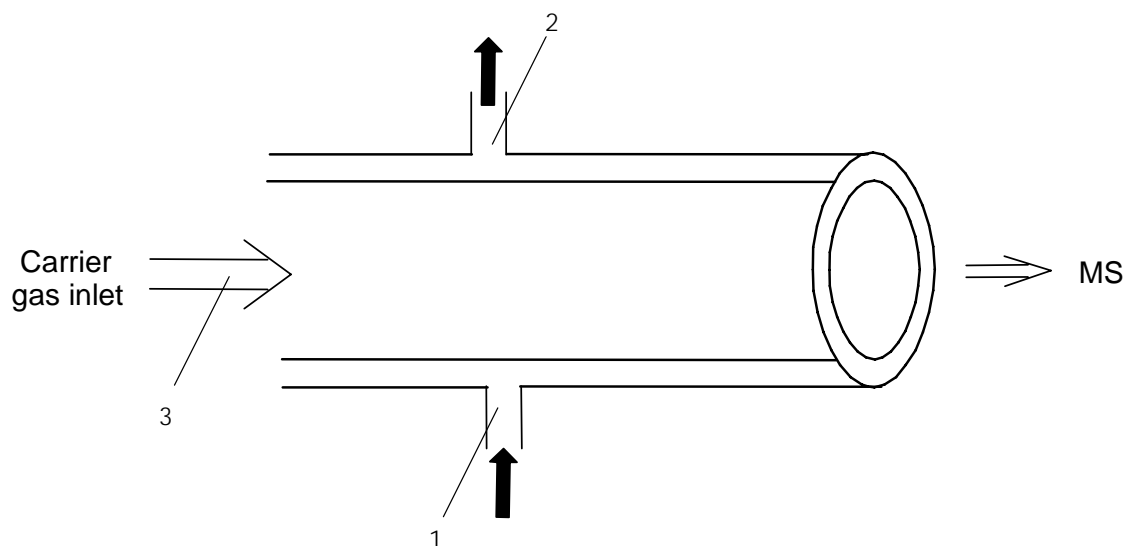The following figure (fig. 2.1) shows the scheme of the coated wall flow tube reactor:

Figure 2.1. Scheme of the coated wall flow tube reactor. 1 and 2 are the in- and outlets of a cooling liquid. 3 is the carrier gas flow.

An overview of the experimental set-up including three different pumping systems (P1, P2, and P3) is seen on the following figure (Fig. 2.2).
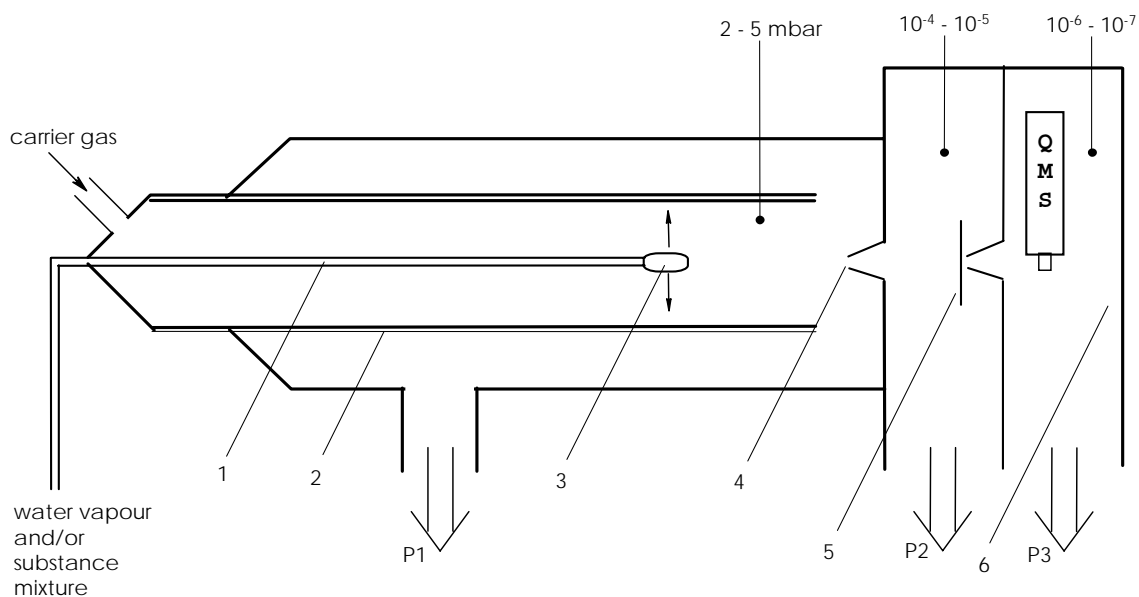
Figure 2.2. Extended scheme of the coated wall flow tube reactor. 1: movable injector, 2: coated flow tube, 3: head of the injector and injection flow, 4: 1 skimmer, 5: pre- vacuum chamber, the chopper and the 2 skimmer and 6: the mass spectrometer chamber. P1, P2 and P3 are the three pumping systems.

The trace gas (injection flow) was injected through a specially designed movable injector (Fig. 2.3).
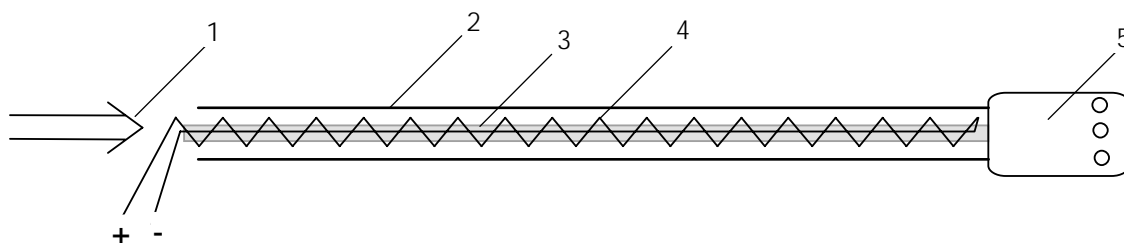
Figure 2.3. Scheme of the movable injector. 1: injection flow, 2: injector tube, 3: inner heating tube, 4: heating wire, 5: the injector head

The movable injector consists of a glass tube with the outer diameter of 6 mm and an injector head with a series of injection holes. In order to prevent the freezing of the trace gas (injection flow), the glass tube was externally wired by an inert metal wire (heating resistor). This wire was connected to a voltage of 35 V and a current of 0.5 A. A local injector temperature of about 40^0 C had been reached. This prevents the freezing the gas even at temperatures as low as -80^0 C of the coated flow tube.

The injection speed of the trace gas (injection flow) was varied from 0.25 to 10 standard cubic centimetres per minute (sccm); the carrier gas is Helium at a

flow between 100 to 800 sccm. In order to keep the reactor pressure constant at 1 to 5 mbar the total input flow must be pumped away (pumping system P1). Thus a rotary pump, (Pfeiffer Balzers Uni 120A) with high pumping speed at about 120 m³/min was used to maintain a steady state flow.

The first skimmer (Fig. 2.2 – 4) contains a small nozzle (radius of 1 mm) which forms a molecular beam downstream. The idea of skimming the flow is, on one hand, to stop the chemical processes at the end of the reactor, and on the other hand, to reduce the pressure of by about 4 to 5 orders of magnitude i.e. from 1 to 5 mbar to 10^{-4} to 10^{-5} mbar.

The pressure in the pre-vacuum chamber is kept constant by the pumping system P2. This has to have a similar pumping speed as the flow of molecules that enter the chamber from the reactor. Thus the turbomolecular pump Pfeiffer Vacuum MTH 1601P with pumping speed of 1380 L/s and the pre-pump Balzers Duo 065D with pumping speed of 65 m³/h and minimal reachable pressure of 10^{-4} mbar were used.

The mass spectrometer chamber (Fig. 2.2 – 6) is the chamber where the QMS is located. The pressure here must be kept in the range of 10^{-6} to 10^{-7} mbar since higher pressures will lead to filament burning. The system consists of a Preiffer Vacuum TMH 1601P turbomolecular pump with a pumping speed of 330 L/s and a minimum pressure of 10^{-8} mbar as well as a pre-pump Balzers Duo 016B with a pumping speed of 16 m³/h.

The final stage represents the detection of the molecules which left the tubular reactor and passed through the first and second skimmer in front of the mass spectrometer. A quadrupole mass spectrometer with electron ionization (Van Bramer, 1998) was used for detection. The main ionization reaction of acetone can be expressed by the following processes:

$$CH_3COCH_3 + e^- \rightarrow CH_3COCH_3^{*+} + 2e^-$$
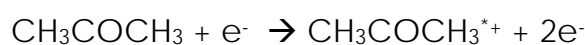
The ionized radical of the acetone molecule gives a signal at 58 in the mass spectrometer. Afterwards it may fragment with the following process:

$$CH_3COCH_3^{*+} \rightarrow CH_3^* + CH_3CO^+$$
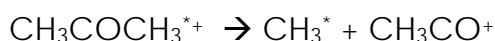
yielding a CH$_3$ radical and CH$_3$CO ionized fragment with mass peak of 43. The CH$_3$ radical can be ionized alternatively:

$$CH_3COCH_3^{*+} \rightarrow CH_3^+ + CH_3CO^*$$
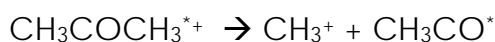
The intensity of the CH$_3$CO (mass 43) fragment is higher than that of CH$_3$ (mass 15) or even than that of the mother peak (mass 58). Thus the measurements discussed later in this thesis are taken at m/z ratio 43. The figure 2.4 presents the mass spectrum of acetone (NIST Webbook, 2005).
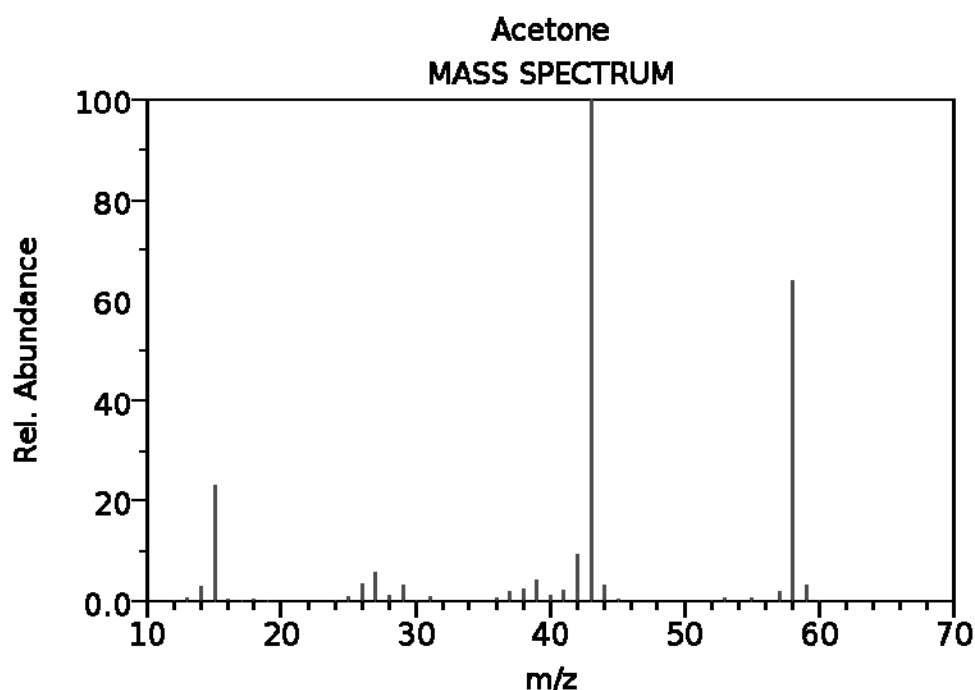
Figure 2.4. Mass spectrum of acetone for 70 eV electron ionization.(NIST Webbook, 2005)

The substance (acetone) molecules which entered the mass spectrometer chamber must be separated from the background molecules. As shown in figure 2.2 (5), a chopper interrupts the beam which entered through the second skimmer with a frequency of about 157 Hz. By subtracting the non-chopped signal from the chopped signal we can calculate the exact value of the acetone molecules. The system consisting of the QMS and the chopper is connected to a personal computer.

3. Experimental principles and performance of measurements

Based on the previous chapter, which explains briefly the experimental set-up and apparatus used in the experiment, this chapter will provide more details of the reactor as well as the approximations made for its operation as a tubular flow reactor.

3.1. Preparation of mixtures

As explained in the previous chapter, acetone is injected through the movable injector. The injector is connected through a flow controller to a mixture flask of 20 L volume.

The preparation procedure of the mixture in the flask is as follows: After the flask is pumped out, acetone was evaporated up to a certain pressure (about 10 mbar - p_b). After this Helium up to 2 bar (p_t) is added. In case a lower concentration is needed we dilute the mixture and add helium again.

The mixture is ready for use after 30 to 60 minutes where upon the helium-acetone mixture has been assumed to be homogeneously mixed.

3.2. Generation of ice films

Surface ice films were generated by deposition of gaseous water upon injection of water vapour through the sliding injector at temperatures of the reactor wall of around 200 K. During this procedure the injector is slowly moved in order to generate an approximately uniform surface film. It was estimated that the ice film depth is approximately 50 to 100 microns (about $4 \cdot 10^4$ mono-layers) for our flow of 150 sccm of water vapour at room temperature and a reactor pressure of about 3.5 mbar. The ice depth was varied by different coating times from 6 to 180 minutes of deposition.

During normal uptake studies additional water has not been added through the injector and the ice film is usable for a few hours of a day once it has

been prepared. Usually there are more than 30-40 single measurements performed on the same ice film.

Thus an important question arises: How stable is this ice film? And how to ensure that ice coverage for the reactor is still the same? To avoid/solve those problems, the tube has been coated on an additional length of about 3 to 5 cm which plays an important buffer role. The water evaporated from this buffer enters the region of the measuring area to keep the ice surface in equilibrium with its vapour (fig 3.1).
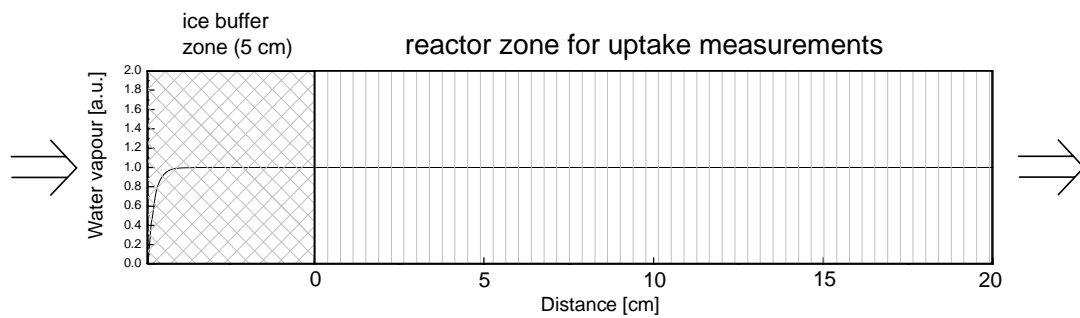
Figure 3.1. Water vapour distribution along the reactor tube.

The calculations show that under the experimental conditions the evaporation process will take a few hours for 1cm buffer length.

3.3. Flow profiles

The flow speed is given by the total volume flow rate passing through a cross section of the reactor tube as described by the following equation

$$V_{flow} = \frac{F_i + F_c}{\pi r^2} \frac{p_{st}T}{pT_{st}}$$

where F_c and F_i are carrier and injector gas flows, respectively, p_{st} and T_{st} are standard pressure and temperature, respectively (1013 mbar and 273.15 K), p is the reactor pressure and T is the coated wall temperature.

According to the experimental conditions, the flow speed in this experiment varies from about 80 to 600 cm s^{-1}. Assuming a reactor pressure of 3 mbar we can calculate the Reynolds number using the equation

$$Re = \frac{V_{flow}\ 2r\ \rho}{\eta}$$

where ρ is the density of the gas and η is the viscosity. If we assume that the flow in the experiments consists of about 99% of helium, the viscosity and density of helium (McCarty and Arp, 1990) can been used, and we calculate Reynolds number between 1 and 8. Since the lower limit in Re for laminar flow to exist is Re≤2300, we can assume that laminar flow is operative.

a)   b)
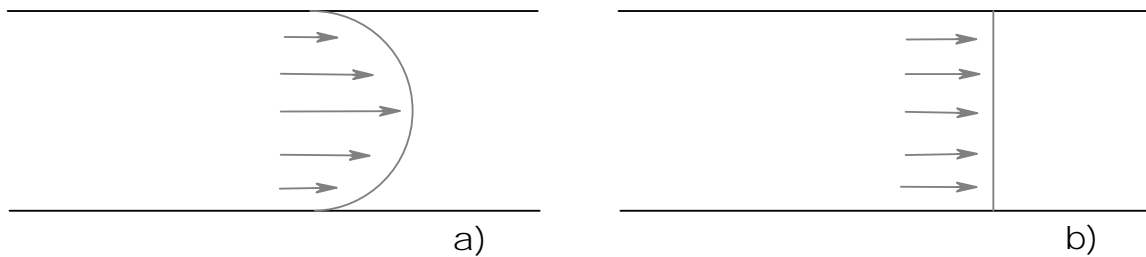
Figure 3.2. A scheme of flow profiles in a tubular reactor. a) Laminar and b) plug flow.

Laminar flow consists of separated parallel layers of flow, each with the same speed, forming a parabolic shape (fig 3.2 –a). A plug flow (fig 3.2 – b) is a more simple way to present flow tube systems. Essentially no back mixing is assumed and the fluid passes through the reactor with a constant averaged speed. Mathematical evidence for the plug flow approximation for our conditions is given by the absence of a radial concentration gradient (see next chapter 3.4).

3.4.   Concentration calculations

The gas phase concentration of acetone in the reactor has been calculated using the following equation:

$$c_g = \frac{N_a\ p_p}{R\ T}$$

where p_p is the ratio of the substance in the total flow, expressed by:

$$p_p = p\ \frac{p_b}{p_t}\ \frac{F_i}{F_i + F_c}$$

Typically the concentration was in the range from 10^{10} to 10^{13} cm^{-3}. In order to estimate whether a radial concentration gradient might build up as a result of wall adsorption, the total mass transferred radially from the gas phase to the

surface must be considered. To do this a segment has been separated from the tube reactor with fixed volume and area which has been assumed as a closed system. Typical conditions of concentration and temperature for the measurements in this experiment have been chosen and the resulting loss to the surface has been estimated. The result for fresh ice surfaces (the highest possible adsorption) showed that less than 2% of the absolute number of gas phase molecules in this segment have been adsorbed on the surface, which corresponds to insignificant radial mass transfer. Thus no difference in concentration between the centre of the tube and close to the wall has been assumed. Therefore a plug flow without radial concentration gradients will be assumed for further modelling calculations.

In case the wall loss would be larger one would have to consider the rate of mass transfer into the outer region of the flow reaction. The diffusion coefficient of acetone a estimated by interpolation in helium at temperature 200 K and 3 mbar of total pressure was found to be $D = 175\ cm^2/s$ (Reid et al., 1987). Hence, the characteristic time of diffusion ($t = <\Delta x>^2/2D$) for the reactor radius of 1.2 cm is estimated to be 4.11 ms. For flow speeds in our experiments from about 80 to 600 cm/s the time for the total axial mass transfer is between 15 to 2 ms per 1.2 cm reactor length. Hence, concentration gradients are in principal possible only for very high flow speeds.

3.5. Concentration profiles and typical measurements

The experiments were performed by consecutively moving the injector backwards and forwards with a constant speed in the range of about 5 to 20 mm/s. After each movement a certain time has to elapse during which the adsorption equilibrium is re-established. The areas of adsorption and desorption peaks shown on the next figure represent the total number of adsorbed and desorbed molecules for the measurement conditions. The profiles are plotted as a function of the laboratory time.

The complete picture of a typical measurement is presented by sub-dividing the temporal profiles into five different stages, depending on each position of the movable injector. A short description of these stages is given below:
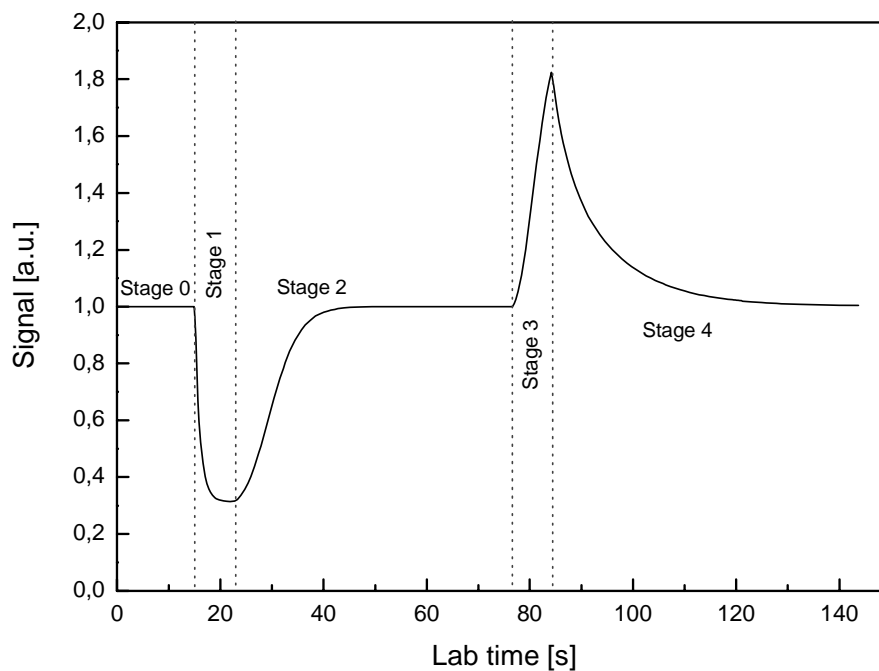
Figure 3.3. Scheme of a concentration profile of a typical measurement.

Stage 0: The movable injector is located just in front of the QMS (i.e. the end of the reactor). The detected signal is constant and the highest value of the MS signal, which corresponds to the initial gas phase concentration. This value is assumed to be 100% signal or 1.0.

Stage 1: This is the beginning of the actual adsorption processes. It starts with continuous movement of the injector with constant speed, which can be varied between 1 to 3 cm/s. During this movement the trace gas will be exposed to a fresh ice film, which causes an initial (highest) drop of the measured signal. The movement is stopped after the end of the programmed distance has been reached.

Stage 2: During this stage the injector is at a fixed outside position. This stage refers to the completion of the uptake process until saturation of the trace gas. The signal increases continuously until the equilibrium between the gas phase and coverage has been established. At this point the adsorption and desorption rates are equal and the total mass balance is zero.

15

As shown in the figure, the signal corresponding to equilibrium conditions is equal to the initial one from the stage 0.

Stage 3: This is the first desorption stage. It represents a continuous movement of the injector backwards in the direction of the MS. It refers to an instant increase of the gas phase concentration due to desorption from the ice surfaces.

Stage 4: The injector is located at the end of the reactor (as in Stage 0). The detected signal from the QMS is a sum of the molecules from the injector flow and the previously adsorbed molecules in the reactor which are desorbing. The desorption process lasts as long as the detected signal is larger than the signal measured in the Stage 0. The remaining amount of adsorbed molecules in the reactor is now low enough to assume the surface as being fresh.

The shape and the time scale of the signal change in each stage strongly depends on the rate coefficients, ice film thickness, concentration range, temperature range, flow speed, injector speed, etc. These dependences will be discussed in the next chapter.

4. Model development and description

The developed kinetic model is based on adsorption/desorption processes in a coated wall flow tube reactor. The model consists of an axial sequence of individual flow tube segments of equal volumes and surface areas in which the gas phase is homogeneously mixed without concentration gradient. The interactions with the reactor wall occur by adsorption and desorption exclusively; reactions on the surface do not occur. Simulations were performed for the temporal behaviour of the gas phase concentration at the end of the reactor tube as a function of laboratory time for the typical operation procedures like instantaneous injection of the gas, instantaneous termination of the gas flow and movements of the injector with constant velocities. The model simulations presented in this chapter were done at parameters typical for our measurements.

4.1. Langmuir adsorption in tubular flow reactors

The developed kinetic model comprises kinetically controlled gas adsorption in individual homogenously mixed volume sections of a tubular flow reactor. Chemical reactions in the gas phase as well as on the surface are not considered. In this case the rate of adsorption of a gas phase component to the surface is given by the Langmuir theory

$$\frac{dc_s}{dt} = k_{ads} c_g \left(c_{s,max} - c_s \right)$$

In here c_g is the gas phase concentration in units of cm^{-3} and $c_{s,max}$ (c_s) is the maximum (temporal) surface concentration in units of cm^{-2}. The rate coefficient for adsorption is considered independent of previous adsorption events and is given by the kinetic theory of gases expression for wall collisions

$$k_{ads} = \frac{1}{4} \bar{c} \gamma \sigma_0$$

17

where $\bar{c} = \sqrt{\dfrac{8kT}{\pi M}}$ is the average speed of thermal gas molecules and γ is the sticking or accommodation probability (uptake coefficient). In the form k_{ads} corresponds to a second order rate coefficient in $cm^3\ s^{-1}$ with σ_0 being the collision cross section of a surface adsorbed molecule. The adsorption rate coefficient k_{ads} has generally a complex temperature dependence originating from the individual factors in the previous equation. To a first approximation, however, and in good agreement with some of our experimental data (Behr et al., 2003) we only consider in the following the T0.5 dependence of the molecular velocity.

Due to mass balance considerations the rate of change of concentration in the gas phase is related to that on the surface by

$$-\frac{dc_s}{dt} = \frac{V}{S}\frac{dc_g}{dt}$$

where V and S are the volume and the surface area of each part of the segmented flow system, respectively. As a consequence gas phase and surface rate changes are proportional and differ by a factor which is given by the reactor's geometry, e.g. 1/2r for a tubular reactor. As opposed to adsorption the inverse process of desorption is considered as a first order process with the rate given by

$$-\frac{dc_s}{dt} = k_{des}c_s$$

where the rate coefficient for desorption k_{des} in units of s^{-1} is again assumed to be independent of other desorption events. However, unlike k_{ads} the rate constant for desorption is assumed to have an Arrhenius temperature dependence with

$$k_{des} = A\exp\left(-\frac{E_{act}}{RT}\right)$$

where E_{act} corresponds roughly to the heat of adsorption for both, physisorption and non-activated chemisorption. Under the conditions of reversible uptake the net change of both gas and surface concentrations in a homogenously mixed volume in contact with a wall is given by

$$-\frac{dc_g}{dt} k_{ads} c_g \left(c_{s,max} - c_s\right) - k_{des} c_s = \frac{S}{V}\frac{dc_s}{dt}$$

This equation may be transformed into a corresponding expression for the fractional surface coverage ($\Theta = c_s/c_{s,max}$) as convenient in Langmuir theory. In this case one obtains

$$\frac{d\Theta}{dt} = k_{ads} c_g \left(1 - \Theta\right) - k_{des}\Theta$$

which upon integration leads to

$$\Theta(t) = \frac{k_{ads} c_g}{k_{ads} c_g + k_{des}} + \left(\Theta_{ini} - \frac{k_{ads} c_g}{k_{ads} c_g + k_{des}}\right) \exp\left(-\left(k_{ads} c_g + k_{des}\right)t\right)$$

This equation describes the temporal evolution of the surface coverage for fixed rate constants of adsorption and desorption starting from an initial surface coverage Θ_{ini}. As can be seen the surface coverage changes exponentially with time where the characteristic time is given by the sum of the time constants of adsorption and desorption. This equation is used in the present kinetic model to calculate concentration changes in the gas phase and on the surface in the flow tube reactor. Apparently it is simplified and derived under assumption for constant gas concentration within the differential time. The complete differential solution and discrepancies between both simplified and compete are presented in the sensitivity tests of the model in this chapter.

4.2. The coated wall flow system model

The equation giving the time dependent change of the surface coverage $\Theta(t)$ can be easily solved explicitly (under the assumption of a constant gas concentration and for infinitively small times) for a given gas phase concentration and fixed values of k_{ads} and k_{des} in a given volume with wall contact. In a flow system, however, the situation becomes more complicated since there are concentration gradients along the reactor distance and the resulting surface change in one volume element is affected by that in the up-stream volume element. Therefore, an iterative procedure must be used to derive the net gas phase concentration at the end of the flow tube which is

19

the quantity normally measured in CWFT studies. To do this we have developed a flow system model in which the total length of the flow reactor is subdivided into a larger number (usually around 200) individual volume elements or segments i of equal length for which each segment is assumed to be homogeneously mixed, i.e. concentration gradient do not exist.
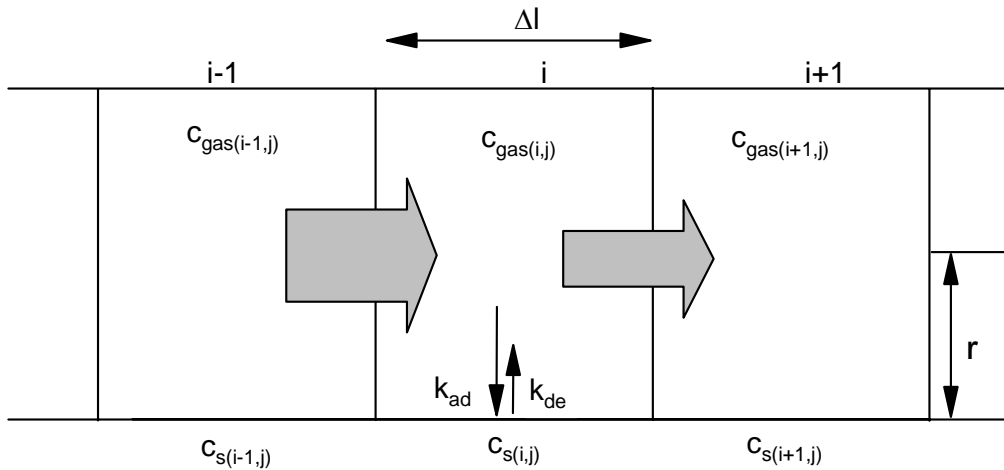

Figure 4.1. Processes connecting gas and surface concentrations in a volume element of the CWFT reactor.

In these segments the gas phase concentration changes with time during the time interval j is as a result of adsorption and desorption. Whether this concentration change leads to increased or decreased surface coverage depends on the initial concentration in this volume element and hence whether the up-stream gas phase concentration is larger or smaller. Therefore the $\Theta(t)$ expression developed above has different starting conditions in each volume element and after each time interval j. Hence, the general expression which accounts for this effect is given by:

$$\Theta(t)_{(i,j)} = \frac{k_{ads}c_{g(i,j)}}{k_{ads}c_{g(i,j)} + k_{des}} + c_{(i,j)}\exp\!\left(-\left(k_{ads}c_{g(i,j)} + k_{des}\right)\Delta t\right)$$

with the integration constant given by

$$c_{(i,j)} = \Theta(t)_{(i,j-1)} - \frac{k_{ads}c_{g(i,j)}}{k_{ads}c_{g(i,j)} + k_{des}}$$

The integration time Δt in this equation corresponds to the average residence time of molecules in the individual segments i, which is determined by the length of each segment divided by the flow velocity. The integration constant $c_{(i,j)}$ for each segment i and time interval j contains the initial surface coverage from the previous time interval j-1.

At this stage of development of the numerical integration scheme it is appropriate to convert from surface coverages and concentrations into absolute numbers of molecules, both in the gas phase and on the surface. The total number of molecules in the gas phase in a segment of length Δl and at time t is

$$N_{gas(i,j)} = c_{g(i,j)}\pi r^2 \Delta l$$

Similarly, the number of adsorbed molecules in one segment i and at time j is related to the surface concentration by

$$N_{ads(i,j)} = \Theta_{(i,j)} C_{s,max} 2\pi r \Delta l$$

The change in total number of gas phase molecules upon entering segment i+1 and during the time interval j is then given by the change of the number of surface adsorbed molecules in segment i+1 during this time interval as a result of adsorption, expressed by the equation

$$N_{gas(i+1,j)} = N_{gas(i,j)} - \left(N_{ads(i,j)} - N_{ads(i,j-1)}\right)$$

A similar equation holds for the change of the surface concentration. In general, however, the sign of this equation (increase or decrease in concentration) depends on the specific situation in the flow reactor and the position of the injector. This will be demonstrated below for different cases of operation of CWFT reactors.

4.3. Mathematical treatment of the data

In this section we present the resulting modelling predictions for different operational procedures of CWFT reactors assuming conditions for Langmuir adsorption and desorption kinetics. Since measurements in such reactors normally focus on the down-stream end of the reactor where the detector is

placed, our studies only consider this situation. The reactor parameters for each simulation are chosen to be typical for our experiments.

4.3.1. Instantaneous gas injection at the upstream end

One of the normal operations of a CWFT reactor is to monitor the concentration response of a gaseous adsorbat following gas injection at the up-stream end of the coated region of the flow tube. This situation is depicted graphically in Fig. 5.2.
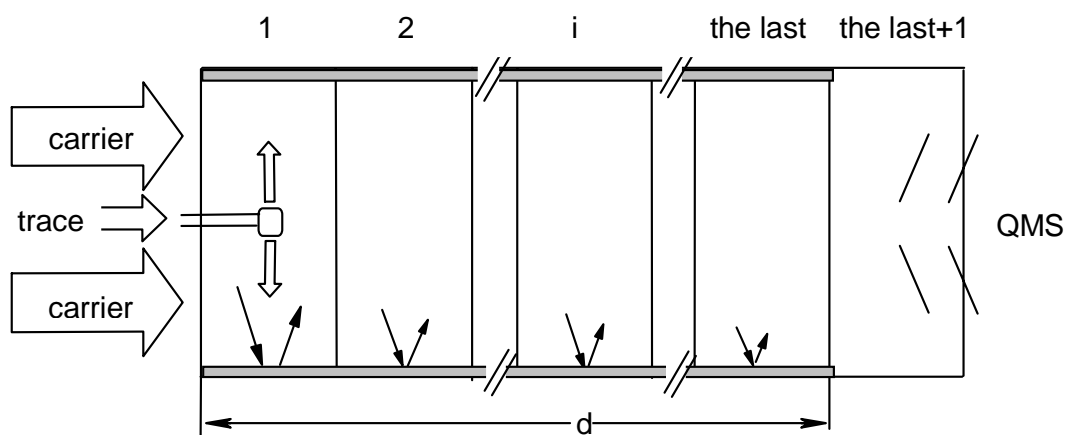

Figure 4.2. Schematic drawing of the processes occurring in different segments of the CWFT reactor when the movable injector is located at the beginning of the reactor tube. The different lengths of the arrows indicate different fluxes.

In this case the injected gas is initially exposed to an entirely fresh surface with the result that there is rapid uptake of gas in volume elements of the flow tube immediately down-stream of the injection point, provided the adsorption kinetics is sufficiently rapid. With time, however, the surface coverages in these segments are saturating and net adsorption occurs only in segments further down-stream. The gas phase concentration at the exit of the reactor therefore evolves only slowly, where the time constant of this evolution depends on both the adsorption and desorption rates. The maximum value of the concentration corresponds to the initial gas phase concentration up-stream of the coated wall and is reached after complete surface equilibration with no net adsorption or desorption. The results from the

22

numerical simulation of gas phase and surface concentration in each of 20 segments of our model reactor together with the resulting net gas phase concentration is shown in the next figure.
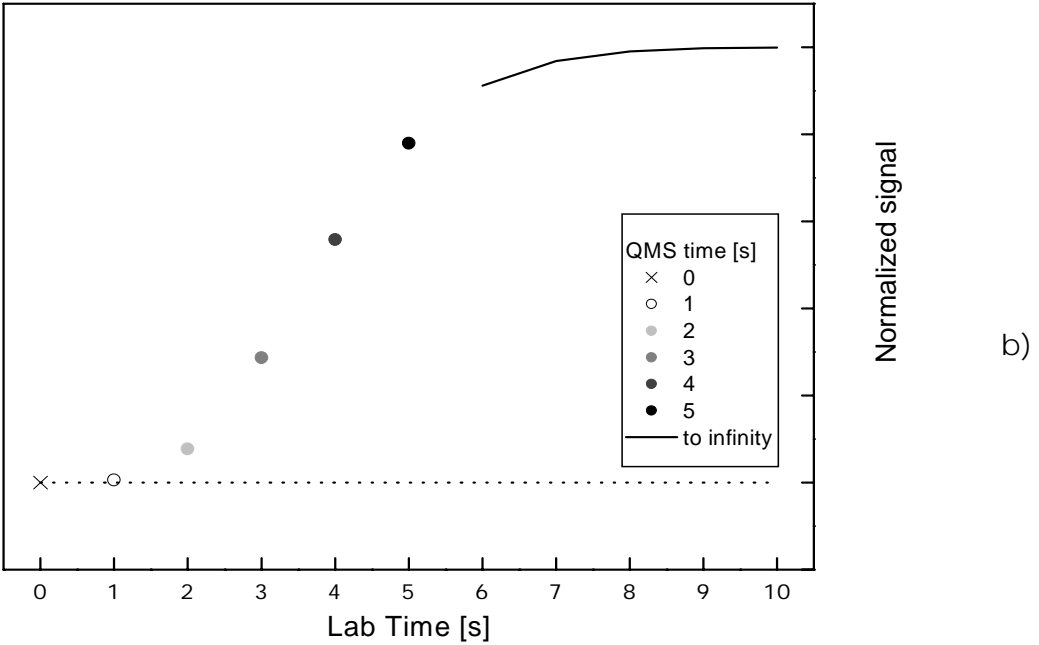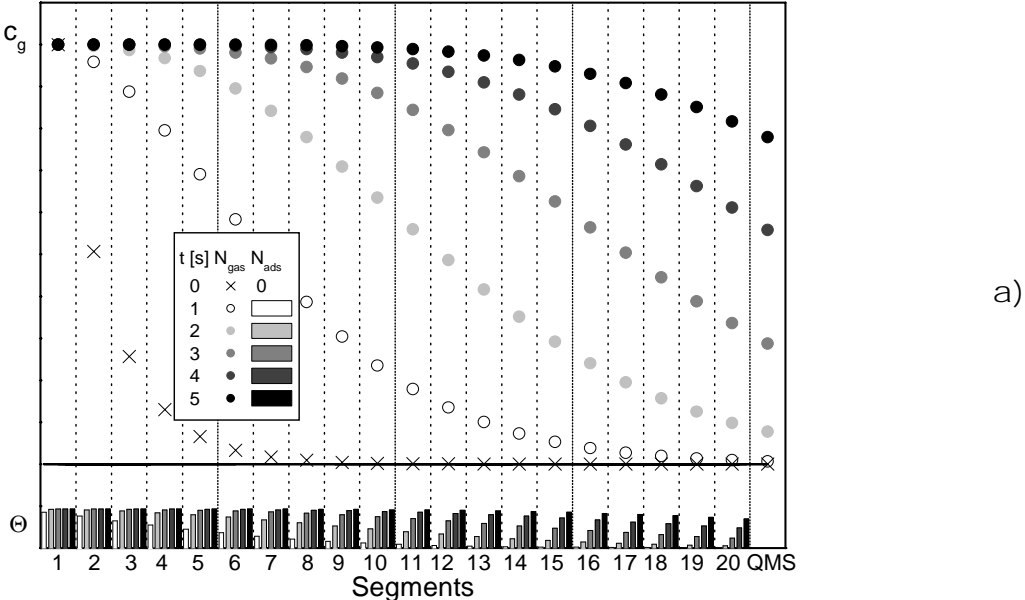

Figure 4.3. Instantaneous gas phase concentrations and surface coverages as well as their temporal evolutions in different volume elements of the coated wall flow tube reactor (a) and corresponding signal intensity at the downstream end of the flow reactor as a function of laboratory time (b).

As can be seen from this figure the gas phase concentration in each segment of the flow reactor is evolving slowly on the time scale of several seconds. As discussed above this is a reflection of the chosen adsorption/desorption kinetics, for which the sum $k_{ads}c_g + k_{des}$ of our model system equals 0.95 s^{-1} at the temperature of the experiment 200 K.

A similar picture applies to the surface coverage. Whereas, however, this coverage is rapidly saturating in the first few segments of the flow tube, there is substantial delay in surface adsorption in the segments further down-stream. In fact more than half of the segments do not attain complete surface coverage during the first 5 s of the experiment.

The effect of temperature on the evolution of the gas phase concentration at the downstream end of the flow reactor has been modelled in independent simulations, the results of which are presented graphically in Fig.4.4. Whereas for the higher temperatures there is rapid penetration of gas through the flow reactor, a considerable delay is observed at lower temperatures. This effect is a reflection of both the adsorption/desorption kinetics as well as the amount of adsorbat on the surface which is increasing with decreasing temperature.
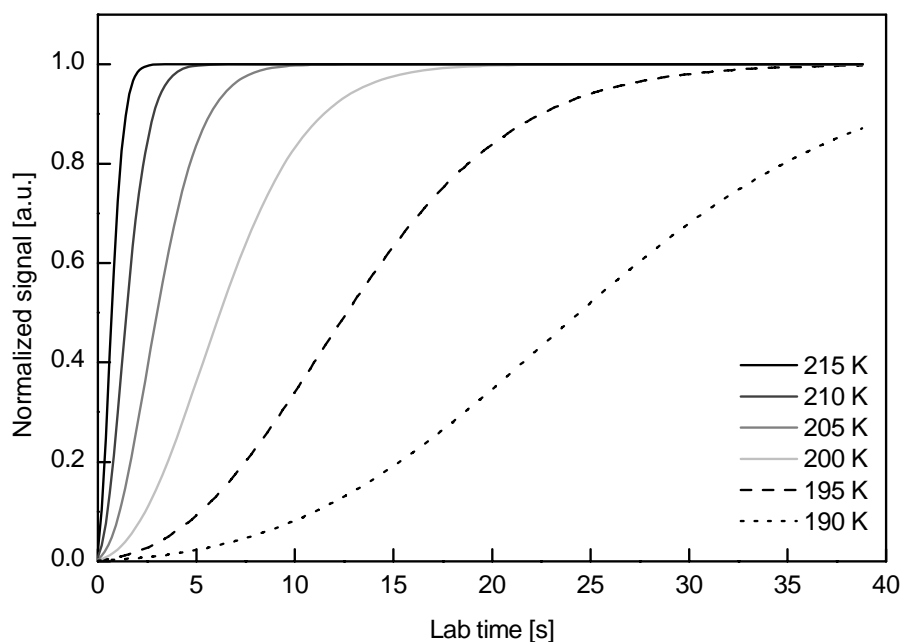

Figure 4.4. Temporal evolution of the normalized QMS signal (proportional to the gas phase concentration) at the downstream end of the flow reactor for different temperatures between 190 and 215K.

24

The total number of adsorbed molecules at each temperature in equilibrium conditions can be derived from the I(t) curves by integrating the area above each curve for time from zero to infinity. As can be shown by this procedure, the number of molecules adsorbed reflects Langmuir behaviour for the particular gas phase concentration considered.

4.3.2. Gas injection through a sliding injector

The standard operational procedure of a flow system is to inject gases whilst the injector is moved in either up-stream or down-stream direction in which case the reaction times between the point of injection and the point of detection are either increased or decreased. In the special case of a wall coated reactor with a loss of gas phase species by surface adsorption these situations correspond to systematic increases or decreases of the available surface areas.

Increasing surface area (stage 1)

In this simulation case the injector is moved with constant velocity (e.g. 1.5 cm/s) in opposite direction of the flow starting from close to the detection point of the QMS system. During the course of this procedure the surface area to which the injected gas is exposed is constantly increasing. This means that new surface area is permanently made available and that high adsorption rates are maintained in the immediate downstream vicinity of the injector tip.

The resulting profiles for the gas phase concentration at the downstream end of the flow reactor are shown in Figure 4.5. In case where desorption is neglected exponential decay curves of the normalized concentration signal as a function of time are observed, at least for gas phase concentrations below $1 \cdot 10^{12}$ cm^{-3} . In this case surface adsorption over the entire time is in the linear region of the adsorption isotherm and adsorption is not saturating.

The same is not the case for higher gas phase concentrations (e.g. $1.4 \cdot 10^{13}$ cm^{-3}). Due to the beginning of saturation of the surface, the temporal evolution of the normalized gas phase concentration is no longer

25

exponential. Rather we predict levelling off of the decaying signal to a steady state value.
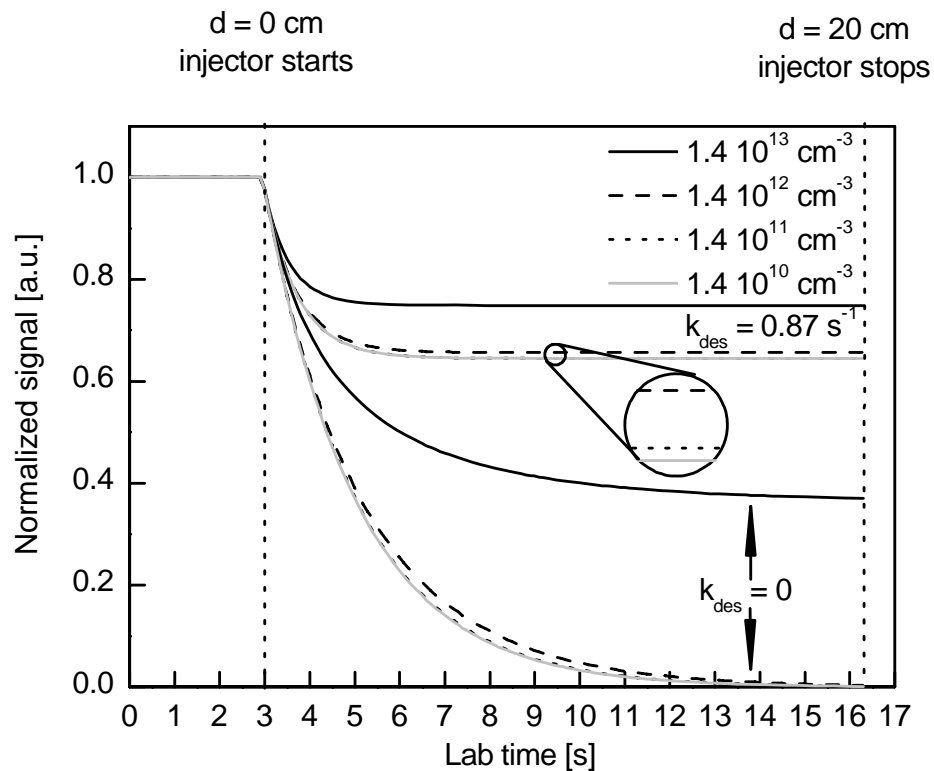

Figure 4.5. Computed evolution of normalized gas phase concentration at the downstream end of the flow reactor as a function of laboratory time for conditions under which the injector is moved with constant speed (e.g.1.5 cm/s) in counterflow direction. The different curves represent different initial gas phase concentrations for both finite desorption (k_{des}=0.87s^{-1}) and negligible desorption (k_{des}=0).

The effect of saturating adsorption becomes even more pronounced if desorption from the surface is also permitted. In this case the temporal profiles level off rapidly with little distinction between the curves for different concentrations at least for the lower concentration ranges. Only for the highest concentration applied a difference is noted. The level of the plateau which is reached depends on the ratio of k_{ads}/k_{des} as well as on the gas flow velocity. Increasing velocities generate higher steady state levels and vice versa (see below).

These findings clearly indicate that adsorption measurements in CWFT reactors have to be conducted with great care if rate coefficients for adsorption are to be determined. Firstly, the gas phase concentration should

be chosen so that surface saturation is avoided. Secondly, if adsorption cannot be separated from desorption and both processes occur simultaneously there is no easy way to extract the surface adsorption rate.
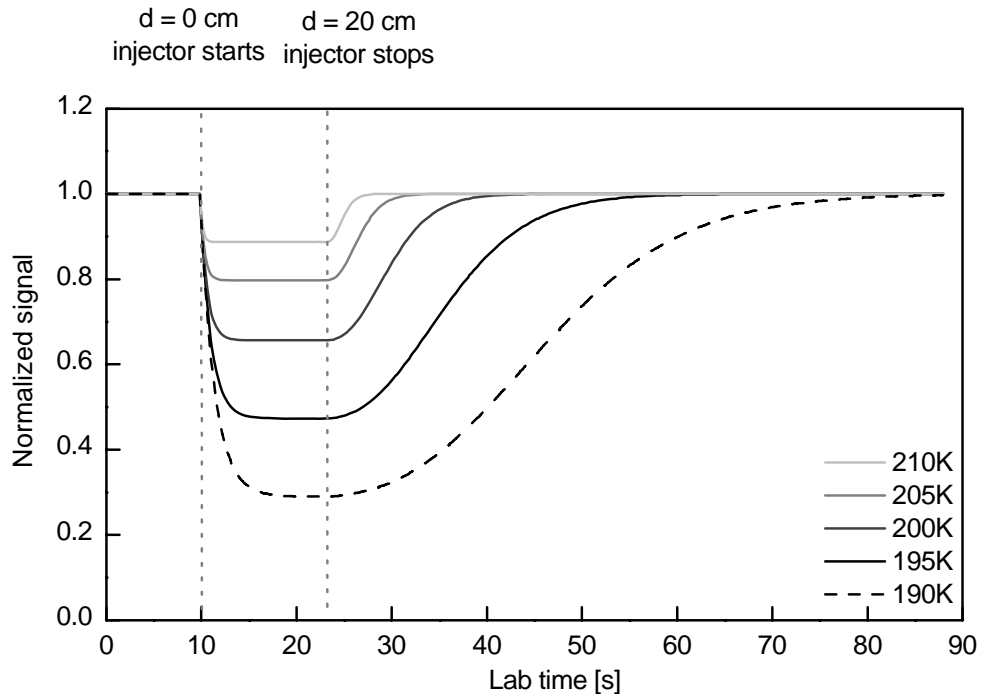

Figure 4.6. Computed profiles of the normalized gas phase concentration at the down-stream end of the CWFT reactor as a function of laboratory time and for different temperatures. The injector has been moved between 10 and 23 s from its down-stream to its up-stream position. The rate coefficients as well as the ratio k_{ads}/k_{des} have been assumed to change as described in subchapter 4.1.

In interesting situation occurs when the injector is stopped at the far end of the coated surface and the evolution in time of the gas phase concentration at the downstream end of the flow reactor is continuously monitored. The result for this model experiment is depicted graphically in fig.4.6. The initial parts of the profiles in this figure are essentially identical to those presented in the previous figure for the case of reversible adsorption. Moreover, it is shown in this figure that the level of the plateau reached during movement of the injector also depends on temperature, with the plateau being lower at lower temperatures. This corresponds to increasingly stronger adsorption because of a decreasing desorption rate. The behaviour in time after the injector is stopped at the up-stream end of the reactor also depends on temperature.

27

Whereas at the highest temperature of 210 K there is rapid recovery of the unattenuated gas phase signal, which corresponds to complete saturation of the entire surface, this recovery is much slower at lower temperatures.

The areas under the profiles of fig. 4.6 correspond to the total number of molecules lost to the surface over the entire time. With the known surface area and the gas phase concentration such areas can be converted into specific surface coverages in molecules/cm^2 and hence can be used to construct adsorption isotherms (Behr et al., 2003).

Decreasing surface area (stage 3)

An interesting situation also evolves when, following complete surface saturation (e.g. after about 90 s of exposure with the injector at the up-stream end of the CWFT), the injector is re-inserted and is moved in flow direction with constant speed. In this case the gas phase concentration behind the injector tip tends to decrease. The rate of decrease, however, is moderated by surface desorption. This in turn increases the gas phase concentration down-stream of the injector tip with the effect that there is additional adsorption. As a net result the temporal profiles of the gas phase concentration at the down-stream end becomes quite complex (see below).

The same complexity applies to the spatial distribution of concentrations along the CWFT axis at a certain point in time. A snapshot of this distribution when the sliding injector tip reaches x=10 cm (e.g. the middle of the length of the coated wall of the reactor) is shown in figure 4.7.
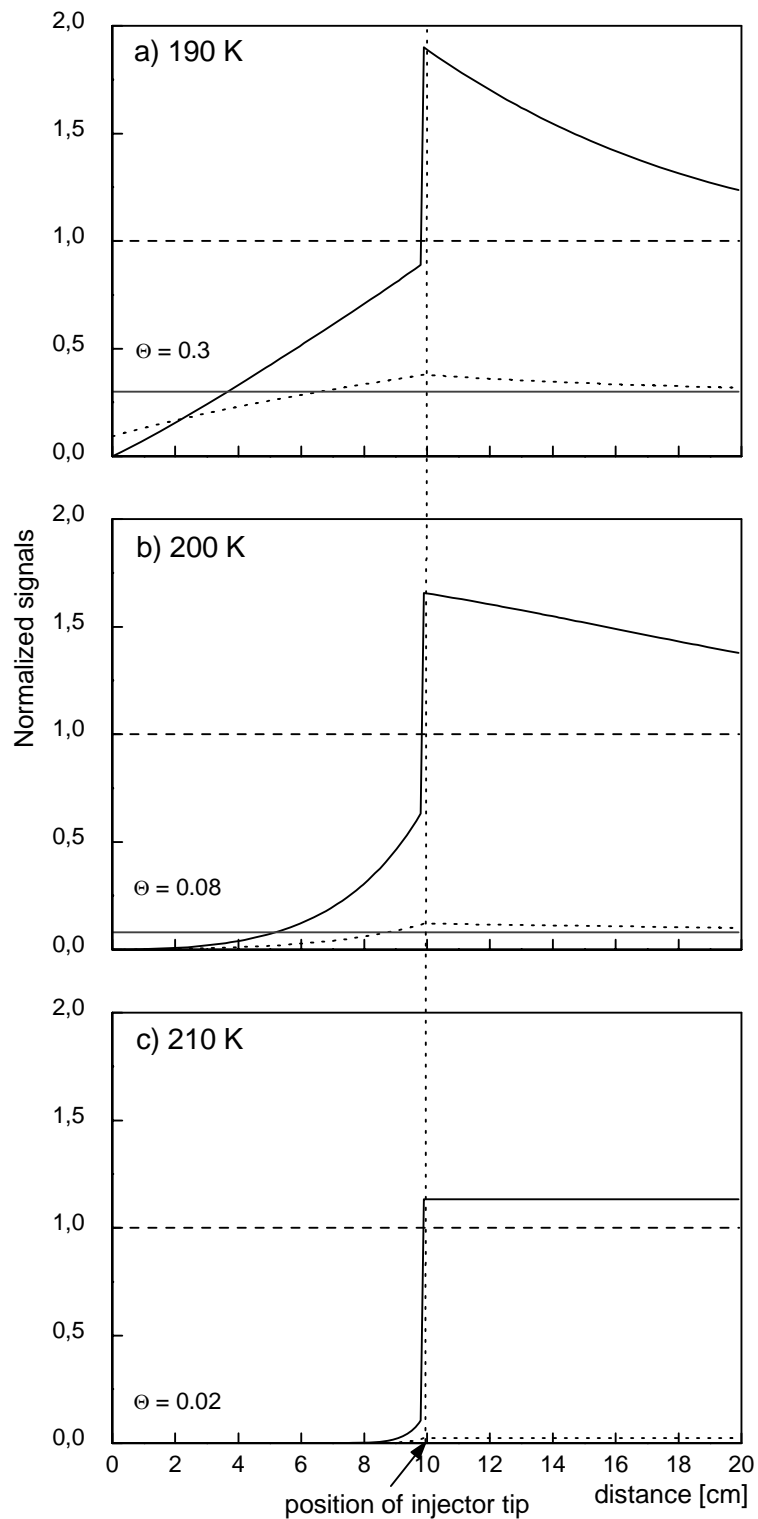
Figure 4.7. Spatial (axial) distribution of gas phase (———) and surface (.......) concentration for a sliding injector at position x=10 cm. The „injected" gas phase concentration (1 10^{12} cm^{-3}) and the equilibrium surface coverages θ are denoted by horizontal dashed lines. Figures a, b and c refer to different temperatures between 190 and 210 K.

29

As can be seen the gross shape of the gas phase concentration is determined by the gas injection at the tip of the sliding injector which generates a step-wise increase in down-stream concentration. The more detailed shapes of the axial distributions, however, vary strongly with temperature. Whereas at the highest temperature there is only a small overshoot and only little tailing downstream and up-stream, respectively, of the injector tip, these effects become more pronounced at lower temperatures. This is mainly caused by the attenuation effect of the surface layer. However, only at lower temperatures the total amount of adsorbent is large enough and its desorption rate sufficiently delayed that the gas phase concentration is significantly affected.

The computational results for a model experiment in which the injector has been moved with constant speed to the far down-stream end of the CWFT and then brought to a halt is shown in figure 4.8. The model runs performed at different temperatures produce desorption signals with entirely different shapes. At the higher temperature we observe a rapid but moderate increase in signal to reach a slight plateau. This is caused by rapid desorption of a small amount of adsorbat once the injector is moved into the down-stream direction. Upon halt of the injector at the down-stream end of the CWFT the desorbing amount is rapidly decaying. At the lower temperature, however, this behaviour is strongly modified. Instead of rapid increase we observe a much more delayed increase with, however, larger amplitude. The peak concentration is only observed once the injector is at its most down-stream position. In each case, however, the peak area under the desorption curves corresponds to the total amount of adsorbat at different temperatures.
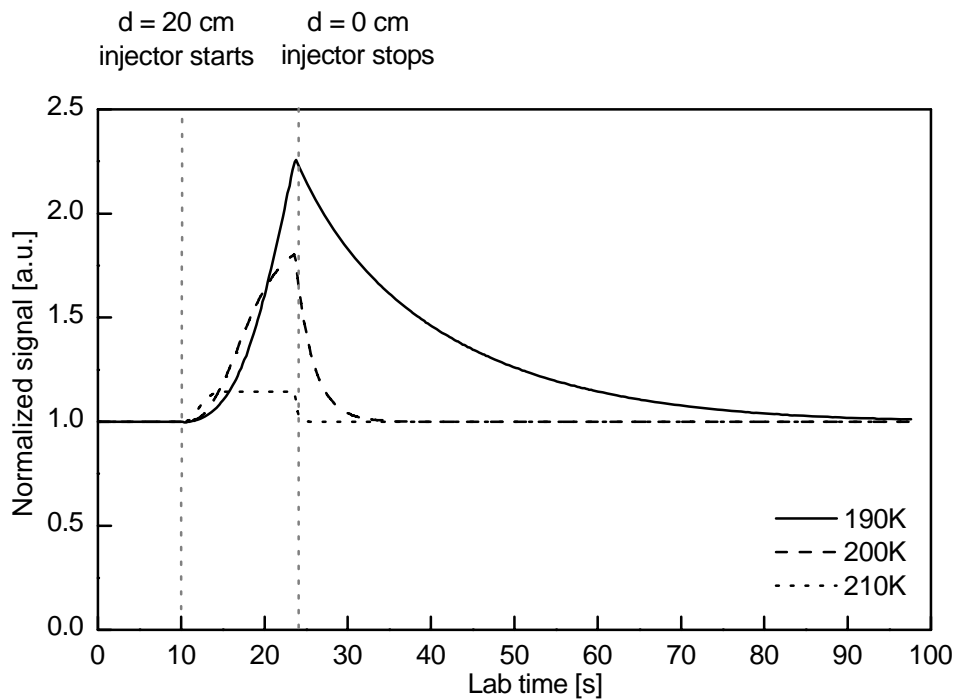
Figure 4.8. Normalized desorption signal of an adsorbat as observed upon and after moving the injector from the up-stream end to the down-stream end of the CWFT. The initial gas phase concentration is around $1.5 \cdot 10^{12}$ cm^{-3}; the different curves are for different temperatures.

The decay part of the desorption peak can be used to extract the rate coefficient for desorption. As shown in Figure 4.9 the decay curves obtained for all three different temperatures are exponential. However, a more quantitative analysis of these decay curves indicates that only at the higher temperature, e.g.210 K, the time constants for decay are almost identical with the time constants for desorption. At lower temperatures on the other hand there is substantial underestimate of the desorption constant caused by successive re-adsorption in the flow reactor.
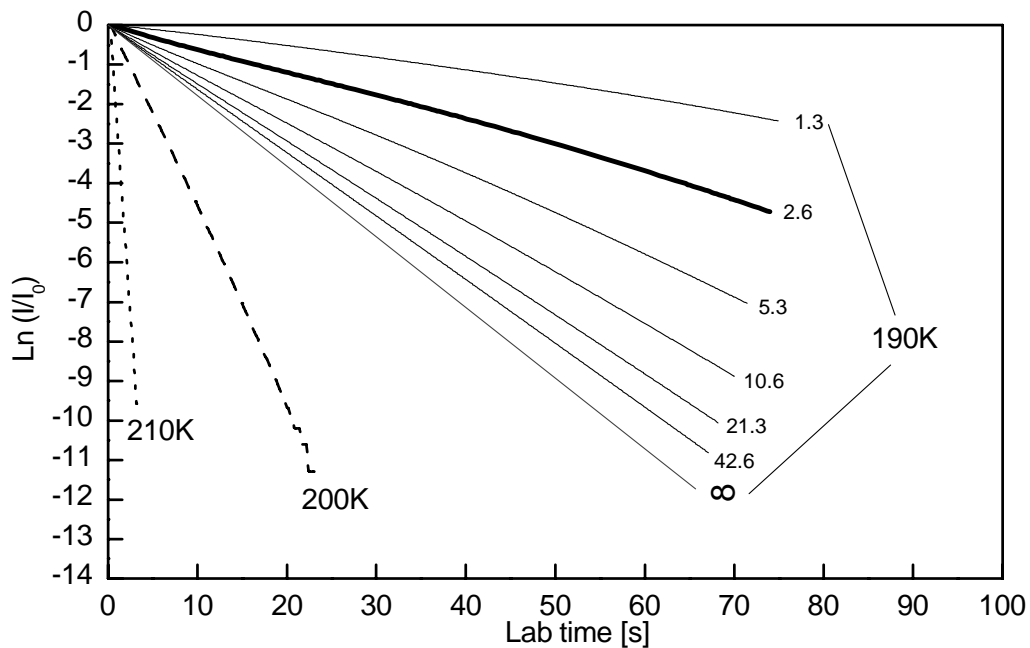
Figure 4.9. Logarithmic representation of the desorption signals of Fig.4.8. The bold lines refer to different temperatures and for a standard flow velocity of 2.6 m/s. The thin lines for T=190 K are for different flow velocities. The slopes of these lines converge to a maximum slope as appropriate for infinite flow velocity.

The extent of this underestimate depends on the flow velocity and hence the residence time in the flow reactor. Only for extremely high flow rates the time constant for the decaying concentration profiles becomes identical with the time constant for desorption.

4.3.3. Injector sliding with different speeds

Another parameter which influences the measured profile is the speed of sliding the injector. For the same conditions this changes the adsorption / desorption processes and also the gas phase and surface concentrations. In order to present the injector speed influence we have performed simulations in which the injector speed varied stepwise as 2.3, 7.5 and 22.6 mm/s. The simulations were made at temperature 200 K, initial gas phase concentration of $2 \ 10^{11} cm^{-3}$ and maximal surface concentration $c_{s,max} = 1 \ 10^{14} \ cm^{-2}$. A snapshot of this simulation when the injector tip reached the middle of the reactor tube (10 cm) is shown on the next figure.
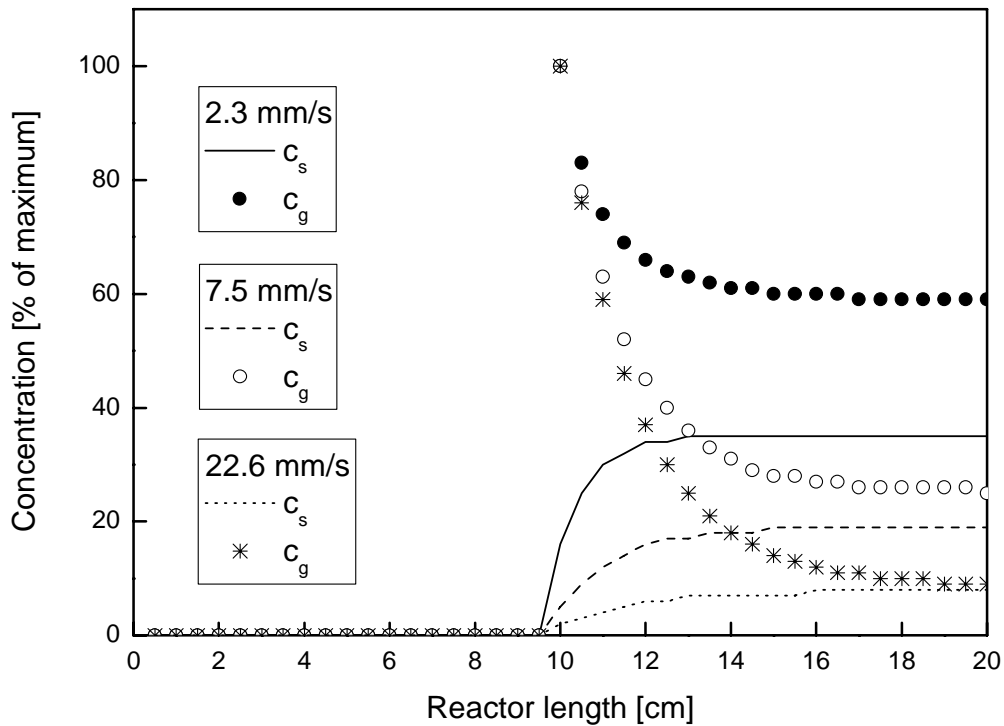
32

Figure 4.10. Axial distribution of gas phase and surface concentration for a sliding injector in stage 1. The simulations were performed at different speeds of the sliding injector. c_s and c_g are the concentrations on the surface and in the gas phase.

For simplicity the surface concentration is expressed by lines and the gas phase concentration by points. It is seen that at higher speeds the initial drop of the gas phase concentration is higher and the increase of the surface coverage along the reactor is slower compared to lower injector speeds. The explanation of this observation is in the different time scales for the three simulations. The time the injector needs to reach the middle of the coated tube at three different injector speeds of 2.3, 7.5 and 22.6 mm/s are, respectively, 44.2, 13.3 and 4.4 s. In other words, the fastest injector speed (shortest time) leads to more instantaneous exposure of the measured gas to the fresh surface and causes a higher change of the gas phase and surface concentration. The same mathematical treatment was applied to desorption experiments (stage 3). The result is shown on the following figure.
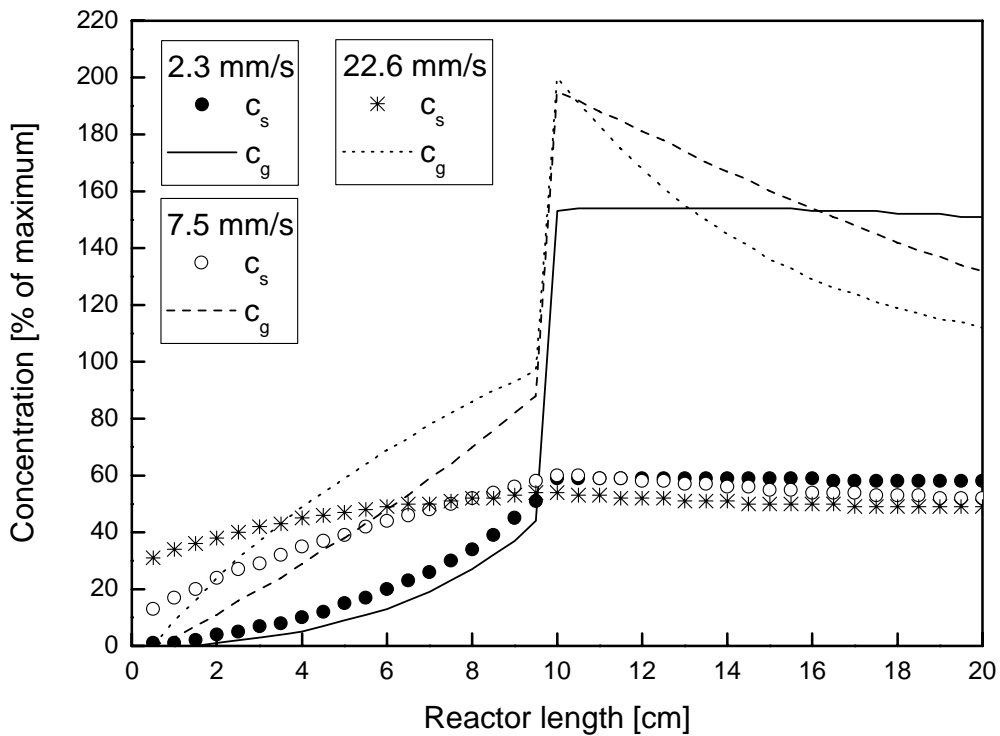
Figure 4.11. Axial distribution of gas phase and surface concentration for a sliding injector in stage 3. The simulations are for different sliding speeds of the injector.

The figure clearly shows that for the fastest speed the gas phase and surface concentrations have the highest values. The relaxation time of the axial surface and gas phase concentration to equilibrium is the most important point of the explanation. In other words, simulations for the slowest speed reflect the latest (in time) snapshot of reaching the equilibrium between gas phase and surface concentration under the experimental conditions.

The gas phase concentration at the end of the tube is the observed measured signal (see the next figure). As has been explained the measured signal for the fastest injector speed has the steepest drop and the steepest increase at stages 1 and 3.
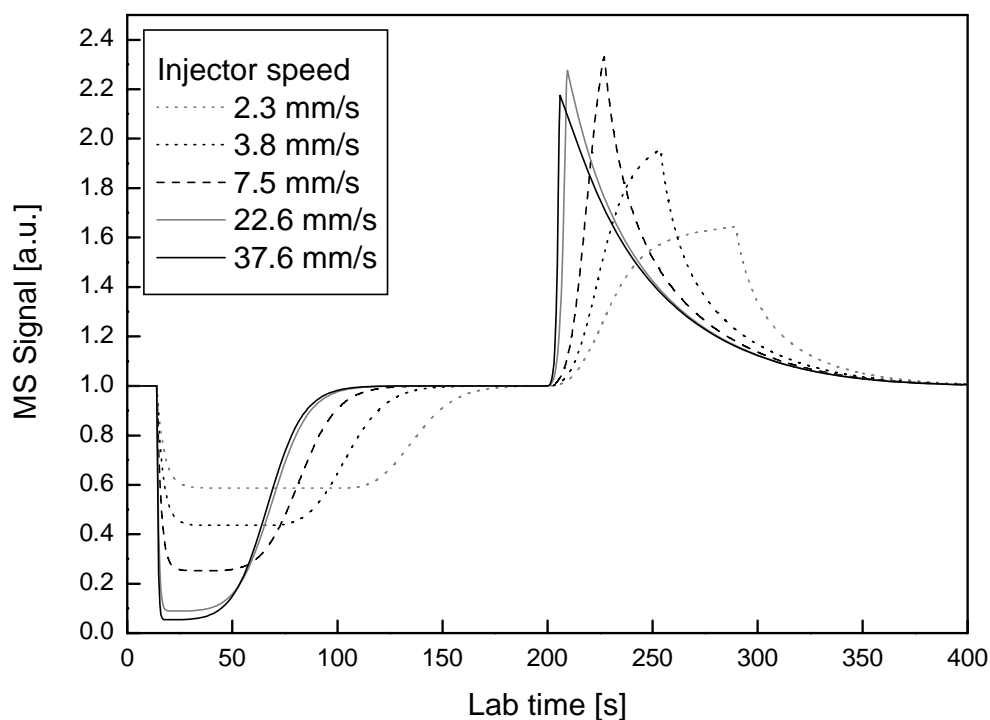
Figure 4.12. Computed profiles of the normalized gas phase concentration at the down-stream end of the CWFT reactor as a function of laboratory time and for different sliding speeds of the injector.

The total adsorption and desorption peaks reflect the same number of adsorbed (and desorbed) molecules which corresponds to the equilibrium (Langmuir) constant and the maximum surface coverage. Both are fixed for the simulations.

4.4. Adsorption at two different surface sites

The present kinetic model based on Langmuir adsorption / desorption equilibrium was found to be applicable only for cases such as on fresh or aged ice surfaces. Thus further development of the model was needed in order to explain the effect of ageing. We decided to use a two-site dynamic adsorption model. According to Langmuir theory, in this model the total adsorption of acetone on the ice film is supposed to be governed by two different adsorption sites: cubic (I_c) and hexagonal (I_h) ice, respectively. Each of these crystallographic forms has their own individual Langmuir parameters K_L and $c_{s,max}$ as well as their own adsorption and desorption kinetics (Figure

35

4.13). The effect of ageing and hence the change of adsorption capacity is then attributed to a change of l_c into the more stable l_h form.
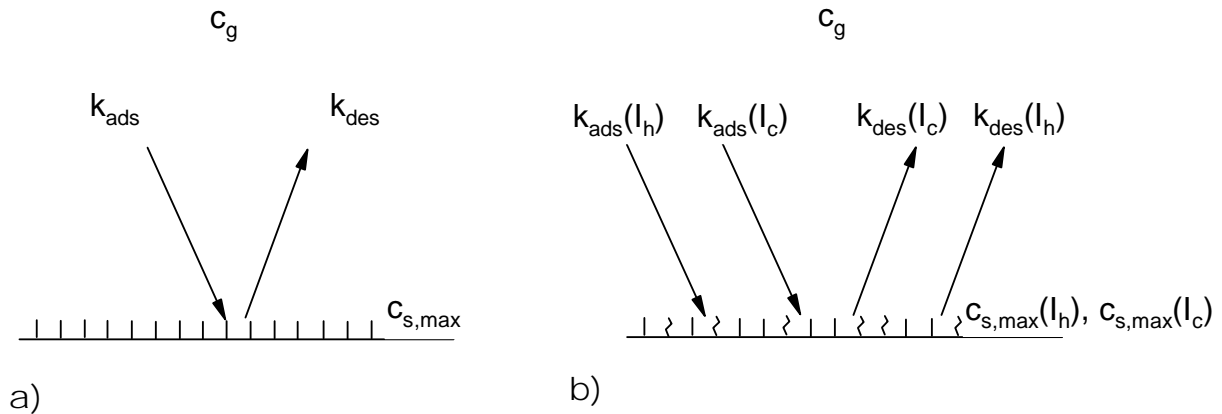

Figure 4.13. Schematic representation of the kinetic model. Adsorption on one a) and adsorption on two different sites b).

The figure 4.13 (b) presents schematically the adsorption of two different surface sites. The hexagonal and cubic sites are shown by straight and zigzag arrows with maximum site numbers $c_{s,max}(l_h)$ and $c_{s,max}(l_c)$. The adsorption rate coefficients for the two sites are $k_{ads}(l_h)$ and $k_{ads}(l_c)$ and the desorption rate coefficients are $k_{des}(l_h)$ and $k_{des}(l_c)$.

The rates of surface coverage under conditions of reversible adsorption to each of the two different adsorption sites are given by the following equations:

$$\frac{dc_{s(lc)}}{dt} = k_{ads(lc)}c_g\left(c_{s,max(lc)} - c_{s(lc)}\right) - k_{des(lc)}c_{s(lc)}$$

and

$$\frac{dc_{s(lh)}}{dt} = k_{ads(lh)}c_g\left(c_{s,max(lh)} - c_{s(lh)}\right) - k_{des(lh)}c_{s(lh)}$$

where $c_{s(lh)}$, $c_{s(lc)}$, $c_{s,max(lh)}$ and $c_{s,max(lc)}$ are the surface concentrations and their maximum values, respectively, for hexagonal and cubic adsorption sites in molecules/cm^2 and c_g is the gas phase concentration of acetone.

The total rate of adsorption as expressed by the overall rate of surface coverage is given by the sum of the two terms, i.e.

$$\frac{dc_s}{dt} = \frac{dc_{s(lc)}}{dt} + \frac{dc_{s(lh)}}{dt}$$

The corresponding change of the gas phase concentration c_g of acetone is related to this surface change by the relation

$$\frac{dc_g}{dt} = -\frac{2}{r}\frac{dc_s}{dt}$$

which is valid for tubular reactors. Since in our experiment only c_g (or its proportional MS signal) has been monitored in the above equations and their integrals have been used to extract the desired parameter, namely k_{ads}, k_{des} and $c_{s,max}$ for each of the two adsorption sites. This is done by fitting of the calculated gas phase concentration as a function of laboratory time to the measured adsorption and desorption profiles. As will be shown below, only the above parameter $c_{s,max(lc)}$ is concluded to change with time as a result of ageing and hence of the conversion of l_c to l_h adsorption sites.

4.5. Model reliability and a mathematical approach

The reliability of the kinetic model was tested using a one site adsorption model. However the results are also applicable to the two surface sites adsorption case. As described in 4.2 we assume the gas phase concentration in each segment to be constant in the differential time period. The complete relation between gas phase molecules and adsorbed molecules in time can be given by the following system of ordinary differential equations (ODE)

$$\left| \begin{aligned} \frac{dc_s}{dt} &= k_{ads}c_g\left(c_{s,max} - c_s\right) - k_{des}c_s \\ \frac{dc_g}{dt} &= -\frac{2}{r}\left(k_{ads}c_g\left(c_{s,max} - c_s\right) - k_{des}c_s\right) \end{aligned} \right.$$

The differential time for our experimental conditions is $1.25 \ 10^{-2}$ and $1.67 \ 10^{-3}$ s, respectively, when the flow velocity is between 80 and 600 cm/s and the segment length is 1 cm. The outputs for the two cases are presented in the next figure 4.14. The ODE system was solved by the Runge-Kutta method (Enright et al., 1986; Fehlberg, 1970; Forsythe et al., 1977; Shampine, 2000) and Maple program.
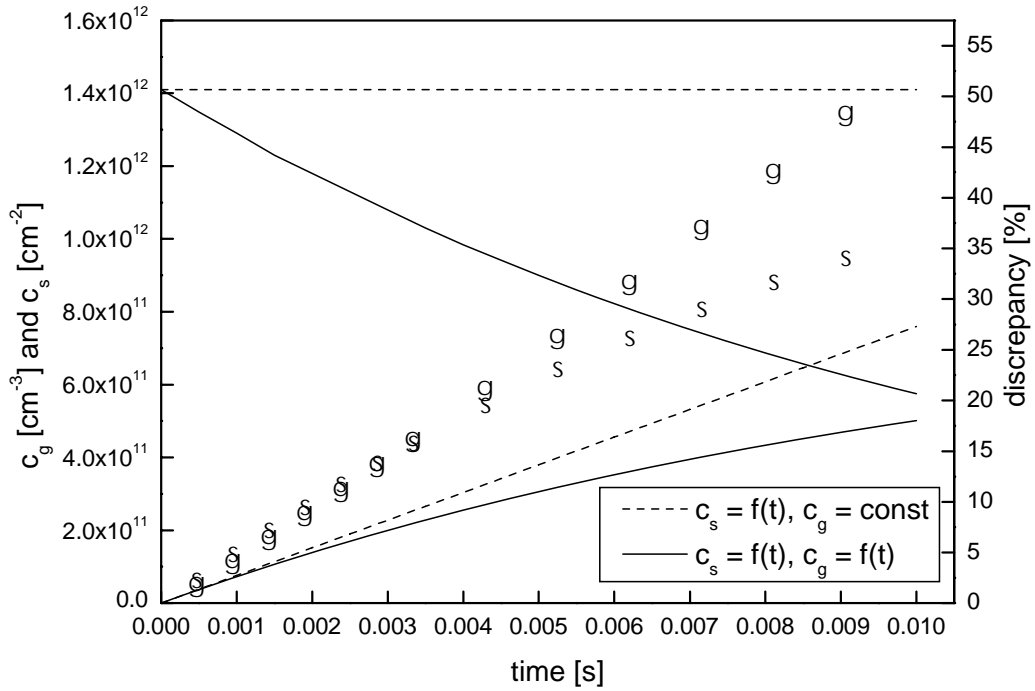
Figure 4.14. Calculation of the surface coverage as a function of time in a reactor segment with radius 1.2 and length 1 cm. Calculations were performed for an initial gas phase concentration of 1.4 10¹³ cm⁻³.

The simulation output shown with dashed line corresponds to the assumption for constant gas phase concentration of $1.4 \ 10^{12}$ cm^{-3} (the upper dashed line). In this case the time dependent surface coverage is calculated by the analytical solution of the following ODE

$$\frac{dc_s}{dt} = k_{ads} c_g \left(c_{s,max} - c_s \right) - k_{des} c_s$$

where the differential time was changed in stepwise from 0 to 0.01 s.

The bold lines express the simultaneous time change of both surface and gas phase concentrations. The calculations in this case were done by numerically solving the system of ODEs mentioned above. As can be clearly seen the increase of the surface coverage is lower compared to the simulation with the constant gas concentration. The discrepancies in the gas phase and surface concentrations for the two calculations are presented in percents with "g" and "s" symbols on figure 4.14. It is seen that the precision increases

38

by decreasing the differential time. Experimentally this time is fixed by the ratio between the segment length and flow velocity, i.e. precision can be increased by decreasing the segment length. The usual segment length for this experiment is 10 times smaller (0.1 cm) than the one used for calculating figure 4.14 i.e. the time was 0.0001 s, which makes insignificant difference in gas phase concentration for this time.

In the next figure a comparison between the output of the model run under conditions of ODE and a system of ODEs with a segment length of 0.5 cm is shown.

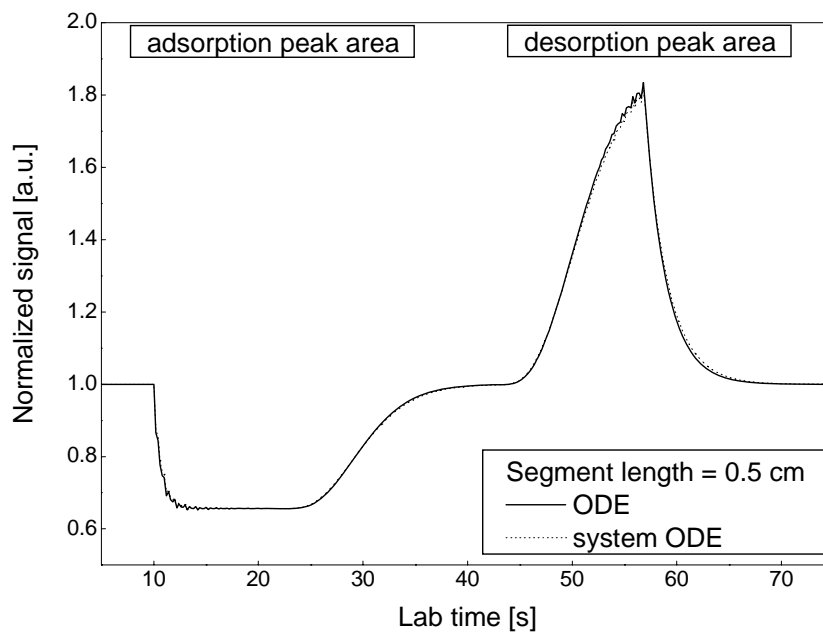*Figure 4.15. Simulations calculated by ODE and a system of ODEs for 200K and a gas phase concentration of 1.4 10^{12} cm^{-3}.*

In order to estimate how much these differences influence the final result we subtracted from the final simulation plot as calculated for a system of ODEs three simulations performed at segment lengths 1, 0.5 and 0.1 cm, respectively.
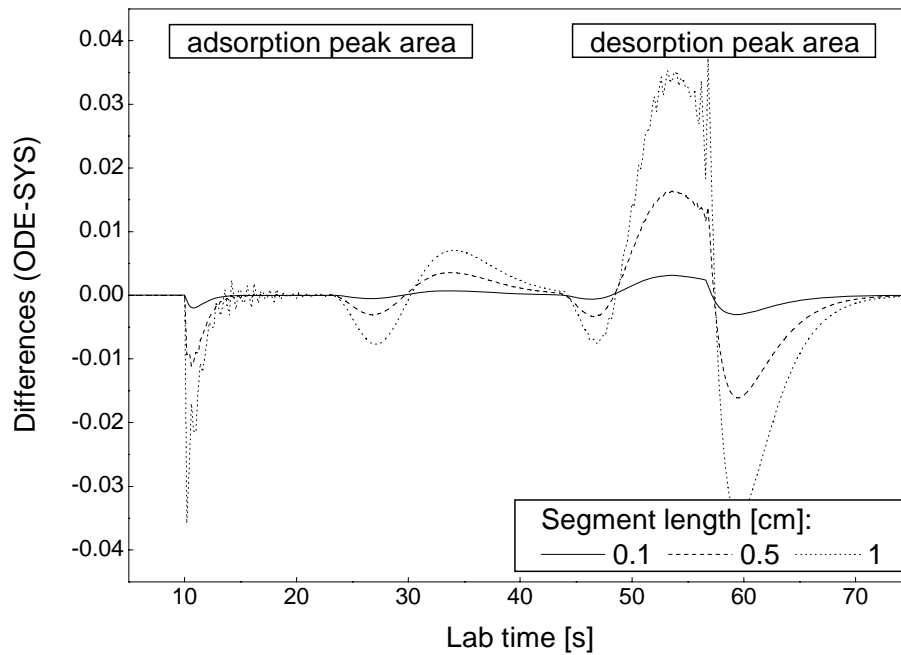
Figure 4.16. Result of subtracting the default simulation from figure 4.15 and three simulations performed at segment length 1, 0.5, and 0.1 cm.

It is obvious that the calculation error from the analytical approximation of the system with differential equations is insignificant.

4.6. Additional models

It was found that the two kinetic models (adsorption on one and on two different surface sites) are the most applicable to explain acetone adsorption on ice at our conditions. Evidences in the literature like ice diffusion, solution and also formation of gas clusters have lead us to create and test a few additional models. These additional processes can be presented as an extended model which influences the main adsorption / desorption equilibrium. For simplicity the developed models will be presented together with the simple Langmuir adsorption model. The simulations in the next chapters (4.6 and 4.7) were done for 200K, $c_g = 2 \ 10^{11}$ cm^{-3} and injector speed of 1.5 cm/s with the following parameters according to the simple Langmuir model as $k_{ads} = 6.1 \ 10^{-13}$ cm^{3}s^{-1}, $k_{des} = 0.2$ s^{-1} and $c_{s,max} = 10^{14}$ cm^{-2}.

4.6.1. Penetration into bulk ice

An extensive theoretical research (Batista and Jonsson, 2001; Girardet and Toubin, 2001; Ikeda-Fukazawa et al., 2002; Livingston and George, 2001; Livingston et al., 2002; Livingston et al., 1998) about bulk penetration processes has been published recently. The processes like bulk and pore diffusion and solution have been treated with different mathematical approaches in order to explain the physical processes. This chapter will present the application of these processes to our adsorption/desorption kinetic model and show how the bulk loss of molecules could influence the equilibrium of gas phase concentration and the measured signal.

Batista and Jonsson in their work (Batista and Jonsson, 2001) explain an additional bulk loss of water molecules as sequent bulk diffusion on the base plane surface of an ice Ih crystal. Their calculations are based on interaction potential and diffusion barriers simulated with Monte Carlo calculations at 140 K. Girardet and Toubin (Girardet and Toubin, 2001) performed a dynamic analysis of the diffusion processes. The molecular dynamic simulations show different transfer times to the ice sub-layers in times of picoseconds.
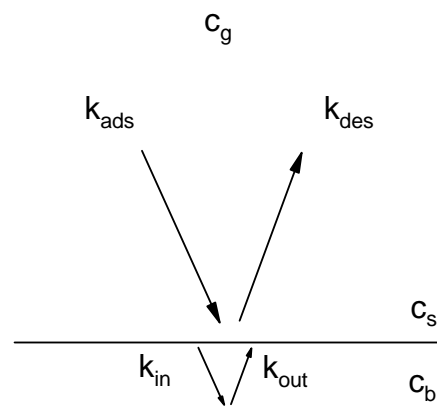
Figure 4.17. Schematic representation of the kinetic model which accounts for an additional loss of adsorbed molecules into the ice bulk.

Based on these theoretical assumptions for stepwise bulk diffusion, a kinetic model has been developed which accounts for an additional loss of adsorbed molecules by penetration into the bulk as presented in the figure 4.17. The adsorbed molecules on the ice surfaces can penetrate into the ice bulk with rate coefficient k_{in} and will return to the surface with k_{out}. The

dimensions of k_{in} and k_{out} correspond to first order process with rate coefficient in units of s^{-1}. The bulk is defined by a fixed number of free sites (c_b) proportional to the depth of the ice layer. The adsorption and desorption processes together with bulk penetration can be expressed completely with the following system of differential equations.

$$\left| \begin{array}{l} \dfrac{dc_g}{dt} = -\dfrac{2}{r}\left(k_{ads}c_g\left(c_{s,max} - c_s\right) - k_{des}c_s\right) \\[3mm] \dfrac{dc_s}{dt} = k_{ads}c_g\left(c_{s,max} - c_s\right) - k_{des}c_s - k_{in}c_s\left(c_{b,max} - c_b\right) + k_{out}c_b \\[3mm] \dfrac{dc_b}{dt} = k_{in}c_s\left(c_{b,max} - c_b\right) - k_{out}c_b \end{array} \right.$$

where the first two ODEs are for gas and surface concentration-time change, and the third is for the bulk penetration process. The model can also be applied freely to pore diffusion, as explained by Keyser et al. 1993.

The effect of this model in comparison with the simple Langmuir model is presented on the next figure (4.18). The calculations were done using the following parameters: $k_{in} = 10^{-15}$ s^{-1}, $k_{out} = 0.01$ s^{-1} and the maximal adsorption capacity of the bulk layer of 7×10^{13} cm^{-2}. As can be seen from the figure, the simulated profile, which includes bulk penetration processes from figure 4.17 (dashed line), has larger adsorption / desorption area compared to the one calculated only for the simple Langmuir model. The higher number of adsorbed (respectively desorbed) molecules corresponds to the maximal bulk concentration c_b and the ratio between k_{in} and k_{out}. In stage 2, the difference between the slopes is caused by the increment of the gas concentration which represents different adsorption kinetics (see chapter 4.8.2). The desorption drop in stage 4 clearly shows two different desorption kinetics. The first one, which is faster, corresponds to the initial desorption from the surface (A to B form figure 4.18) and the second one is slower due to segregation from the bulk phase to the gas phase as accounted for by the k_{out} rate coefficient.
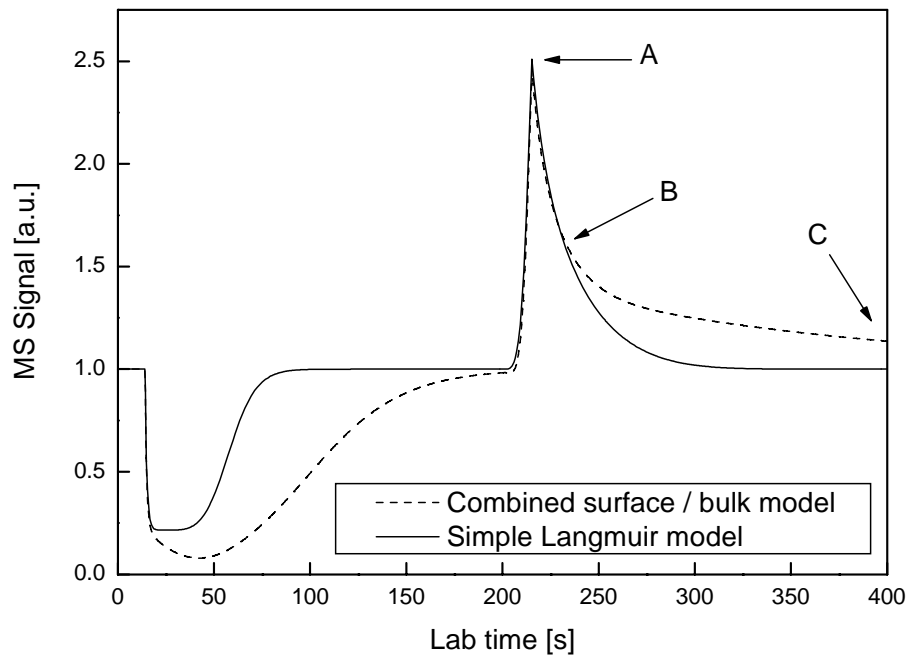
Figure 4.18. A comparison between combined surface/bulk model and the simple Langmuir model.

Based on the same theoretical assumption the model has been further improved by creating a model which accounts for bulk processes separated into two layers, so that the stepwise bulk penetration (Girardet and Toubin, 2001) can be allowed for.

Figure 4.19. A scheme of a multilayer bulk penetration.

The processes shown are fully described mathematically with the equations:

43

$$\left|\frac{dc_g}{dt} = -\frac{2}{r}\left(k_{ads}c_g\left(c_{s,max}-c_s\right)-k_{des}c_s\right)\right.$$

$$\left|\frac{dc_s}{dt} = k_{ads}c_g\left(c_{s,max}-c_s\right)-k_{des}c_s-k_{in1}c_s\left(c_{s,max}-c_s\right)+k_{out1}c_{b1}\right.$$
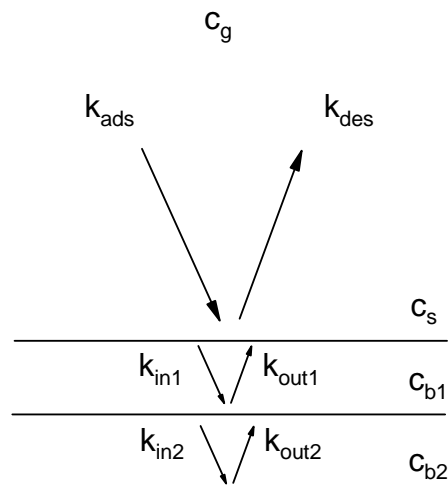
$$\left|\frac{dc_{b1}}{dt} = k_{in1}c_s\left(c_{s,max}-c_s\right)-k_{out1}c_{b1}-k_{in2}c_{b1}\left(c_{b1,max}-c_{b1}\right)+k_{out2}c_{b2}\right.$$

$$\left|\frac{dc_{b2}}{dt} = k_{in2}c_{b1}\left(c_{b1,max}-c_{b1}\right)-k_{out2}c_{b2}\right.$$

where the unit of the coefficients related to the layer bulk penetration k_{in1}, k_{out1}, k_{in2}, and k_{out2} is s^{-1}. It is very hard to extract valuable experimental results from the bulk parameters, which is the main reason not to develop the model.

The next kinetic model is based on sequential Henry solution of the adsorbed molecules in a quasi-liquid surface layer of the ice.
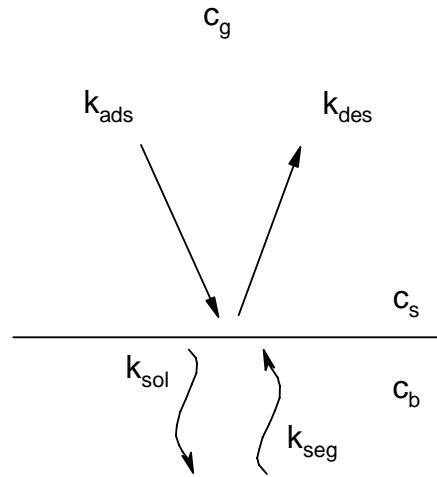
Figure 4.20. A scheme of a Henry solution model

The solution and segregation coefficients together with the bulk concentration represent the bulk processes. The complete mathematical expression of the processes is given by the system

$$\left|\frac{dc_g}{dt} = -\frac{2}{r}\left(k_{ads}c_g\left(c_{s,max}-c_s\right)-k_{des}c_s\right)\right.$$

$$\left|\frac{dc_s}{dt} = k_{ads}c_g\left(c_{s,max}-c_s\right)-k_{des}c_s-k_{sol}c_s+k_{seg}c_b\right.$$

$$\left|\frac{dc_b}{dt} = k_{sol}c_s-k_{seg}c_b\right.$$

The bulk concentration c_b is given by the dissolved molecules in the ice bulk volume which is proportional to the ice depth and the geometry of the reactor. The dissolved molecules correlate with the ratio between solution and segregation rate coefficients.
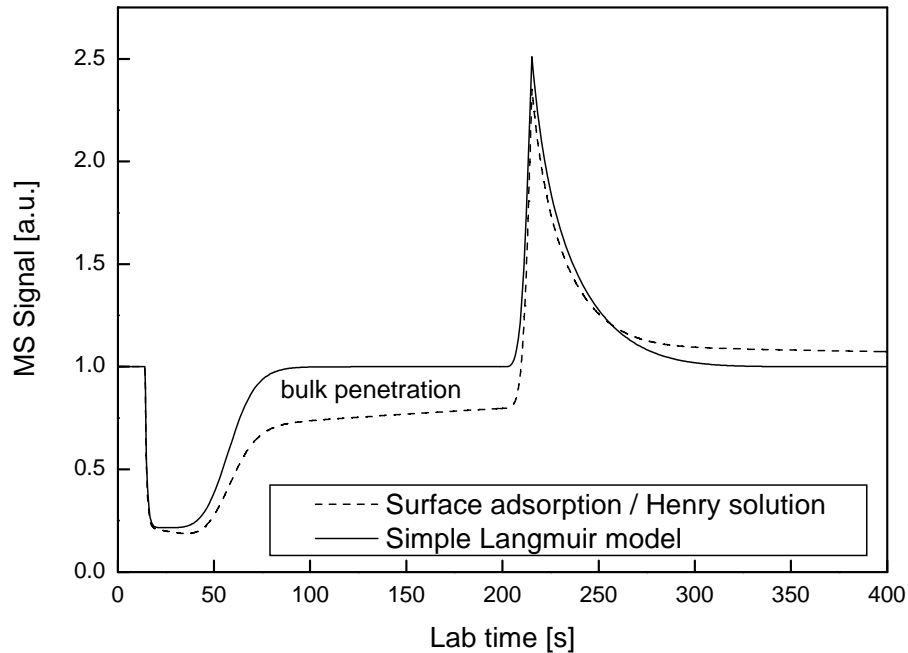
Figure 4.21. A comparison between surface adsorption / Henry solution model (dashed line) and the simple Langmuir model (bold line).

The simulation shown in the figure was calculated with the following parameters: $k_{sol} = 10^3$ cm^{-1}s^{-1}, $k_{seg} = 3 \cdot 10^{-3}$ s^{-1} and an ice depth of 10^{-4} cm. The area between the bold and dashed line in stage 2 corresponds to the additional number of penetrated molecules from the surface to the ice bulk. As can be seen the time of about 200 s is not enough to establish equilibrium between the totally removed molecules from the gas phase and those that have been injected through the movable inlet. Thus longer simulation has also been performed (figure 4.22).

45
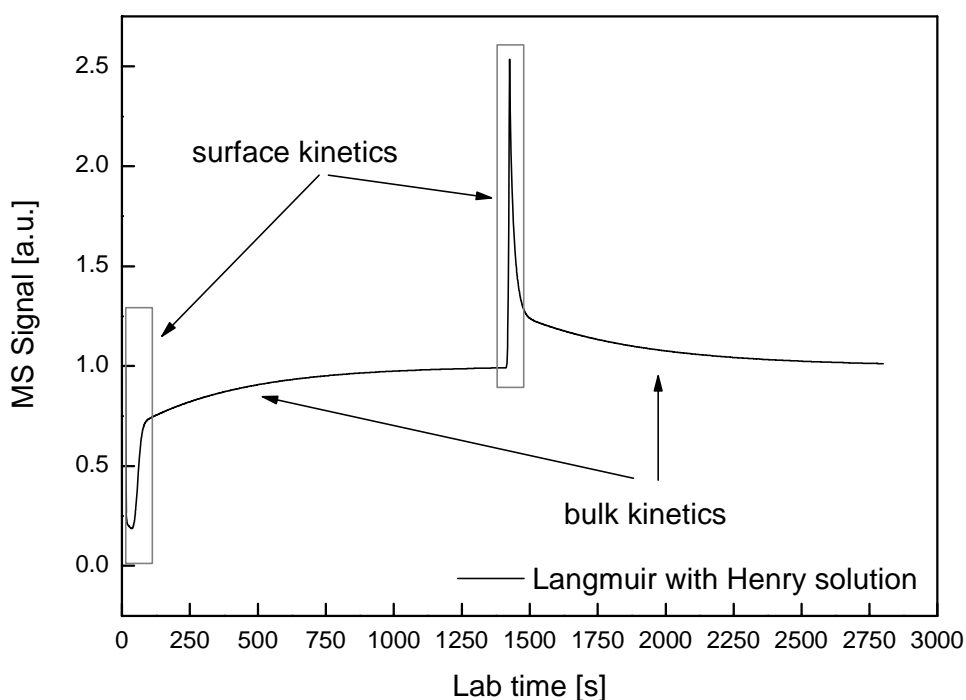
Figure 4.22. The same as Figure 4.21 with enlarged time scale.

The marked zones in the figure 4.22 represent the surface processes. As can be seen they are about 2 orders of magnitude faster than the bulk solution.

George's group (Livingston et al., 2002) measured bulk and surface diffusion in ice of NH_3, CH_3COOH, CH_3OH, HCl and HCOOH and found a diffusion coefficient for these substances between 10^{-16} to 10^{-9} cm^2/s in the temperature range of 140 to 200 K. Abbatt et al. (Cox et al., 2005) have developed a kinetic model (using Facsimile program) including ice diffusion. Relying on this literature observation a kinetic model which accounts for ice bulk diffusion has also been created based on the following scheme

Figure 4.23. Schematic representation of adsorption on ice with subsequent bulk diffusion as expressed by the diffusion coefficient

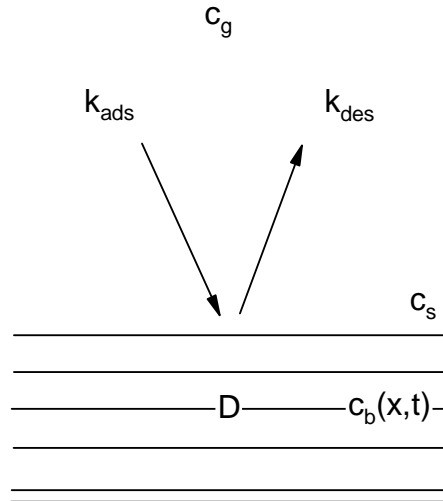The diffusion theory indicates that we have a bulk concentration gradient i.e. the bulk concentration is a function of the ice depth. Relying on this the processes can be described mathematically with the following system of ODEs.

$$\left|\frac{dc_s}{dt} = k_{ads}c_g\left(c_{s,max} - c_s\right) - k_{des}c_s\right.$$

$$\left|\frac{dc_g}{dt} = -\frac{2}{r}\left(k_{ads}c_g\left(c_{s,max} - c_s\right) - k_{des}c_s\right)\right.$$

$$\left|\frac{c_b(x,t)}{c_{b,0}(x,0)} = \frac{1}{2}\left[erf\left(\frac{h-x}{2\sqrt{Dt}}\right) + erf\left(\frac{h+x}{2\sqrt{Dt}}\right)\right]\right.$$

where the c_b is the depth dependent bulk concentration, D is the diffusion coefficient, and x is the ice depth.

The total gas uptake is probably a complicated bulk process which depends on several factors like pore diffusion, solvation and ice diffusion, taken with a different weight.

4.6.2. Cluster model

The background of this model is based on the desorption energies of acetone and water molecules from ice surfaces which are, respectively, about 29 and 48 kJ/mol. The desorption of initially adsorbed acetone molecules on the ice surfaces could occur accordingly by two processes 1) acetone desorption

from ice with a rate coefficient k_{des1} and 2) desorption of clusters of acetone and water with rate coefficient k_{des2}. In the second case acetone molecules leave the surface together with one water molecule. The bond energy between water and acetone molecules in the cluster is about 29 kJ/mol. The concentration of desorbed clusters and single acetone molecules in the gas phase is c_{g2} and c_{g1}, respectively, and their further adsorption is with adsorption rate constants k_{ads2} and k_{ads1}, respectively.
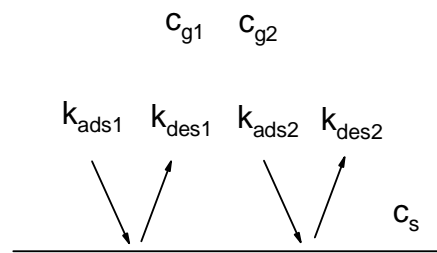
Figure 4.24. A scheme of the cluster model

Once adsorbed on the surface, the clusters or acetone molecules are no longer distinguishable, so the surface concentration c_s is given by the number of adsorbed species per area. These processes are fully described by the following system of ordinary differential equations

$$\left|\begin{array}{l} \dfrac{dc_{g1}}{dt} = -\dfrac{2}{r}\left(k_{ads1}c_{g1}\left(c_{s,max} - c_s\right) - k_{des1}c_s\right) \\[3mm] \dfrac{dc_{g2}}{dt} = -\dfrac{2}{r}\left(k_{ads2}c_{g2}\left(c_{s,max} - c_s\right) - k_{des2}c_s\right) \\[3mm] \dfrac{dc_s}{dt} = \left(k_{ads1}c_{g1} + k_{ads2}c_{g2}\right)\left(c_{s,max} - c_s\right) - \left(k_{des1} + k_{des2}\right)c_s \end{array}\right.$$

The gas phase concentration of acetone (c_{g1}) and their clusters (c_{g2}) are not detectable separately, i.e. the observed signal is a sum of species. However, their contributions can be simulated during the calculation.
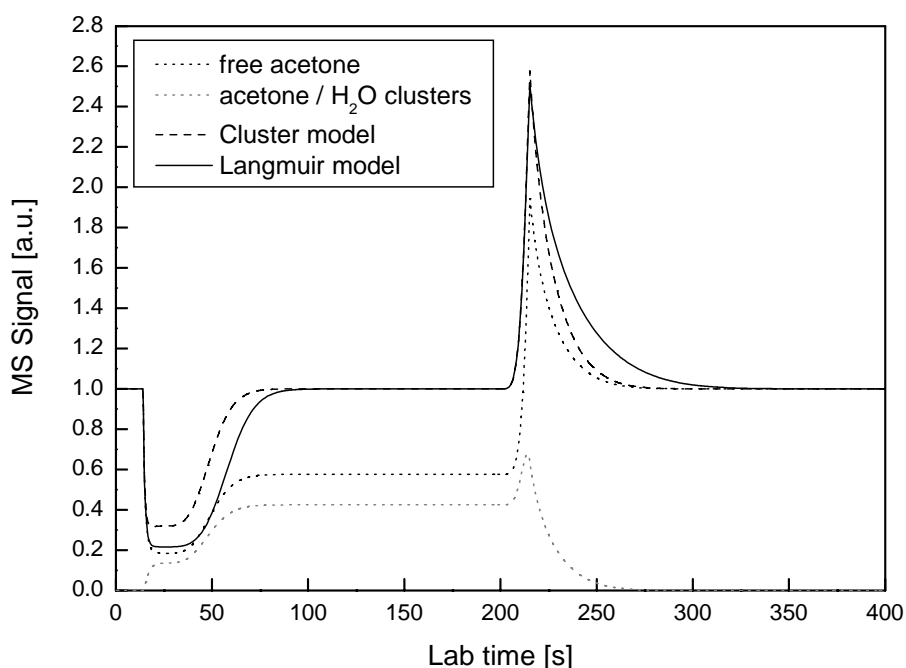
Figure 4.25. Simulated profiles of temporal evolution of adsorption/desorption processes with a cluster model in a CWFT reactor. The dotted lines represent the gas phase concentration of acetone molecules and clusters, and the dashed line the observed signal.

The profile shape of the sum line strongly depends on the kinetic parameters chosen for the simulation. The model has not been completely tested yet, however, it explains some particular measurements which cannot be explained by the models reported above.

4.7. Data fits and sensitivity tests of the model

The measured signal, i.e. gas phase concentration at the end of the reactor tube, can be considered as a function of parameters for the respective measurement. There are two types of parameters: experimental parameters and kinetic parameters. Experimental measurable parameters include temperature, pressure, flow rates etc. Kinetic parameters include adsorption and desorption rate constants as well as maximum surface coverages. Whereas experimental parameters can be easily measured within narrow error limits, this is not the case for the kinetic parameters.

The developed kinetic model can be considered as a mathematical function f_{math}(exp, kinetic), analogous to the experimental one f_{exp}(exp, kinetic). We assume that the values of the kinetic parameters k_{ads}, k_{des} and $c_{s,max}$ describing the adsorption desorption processes are accurate, when the two functions f_{exp} and f_{math} have equal output. By *data fit* we understand a consecutive change of the kinetic parameters so that the calculated output f_{math} has as shape identical to the measured one f_{exp}. This procedure has been performed manually for the present study. In this chapter more detailed information and the most important steps of the fitting procedure are presented.

4.7.1. Initialization of fits

The typical measured data (f_{exp}) are contained in a table where the change of the mass spectrometer signal in laboratory time has been stored. Typically, the time step for lab time, where the averaged count pulses is about 0.2 sec; 2 minutes of typical measurement time will result in about 600 measured points. As has been described, the actual timing (moments) of when and how the movable injector should move have been defined manually. Thus these parameters including temperature, reactor pressure, initial gas phase concentration, gas flows, molecular weight of the substance, count pulses step and the geometry of the reactor must be entered in the model.

A typical measurement is presented on the next figure. The times t_1 and t_2 are the starting times for moving the injector forward and backward, respectively. These timings were given manually when the measurement has been performed. The pointed slopes on the figure 4.26 reflect the kinetic processes. Together with this, these parts of the spectrum (stage 2 and 4) are the most sensible; therefore by varying the rate coefficients we influence the simulated output f_{math} in order to fit the data.
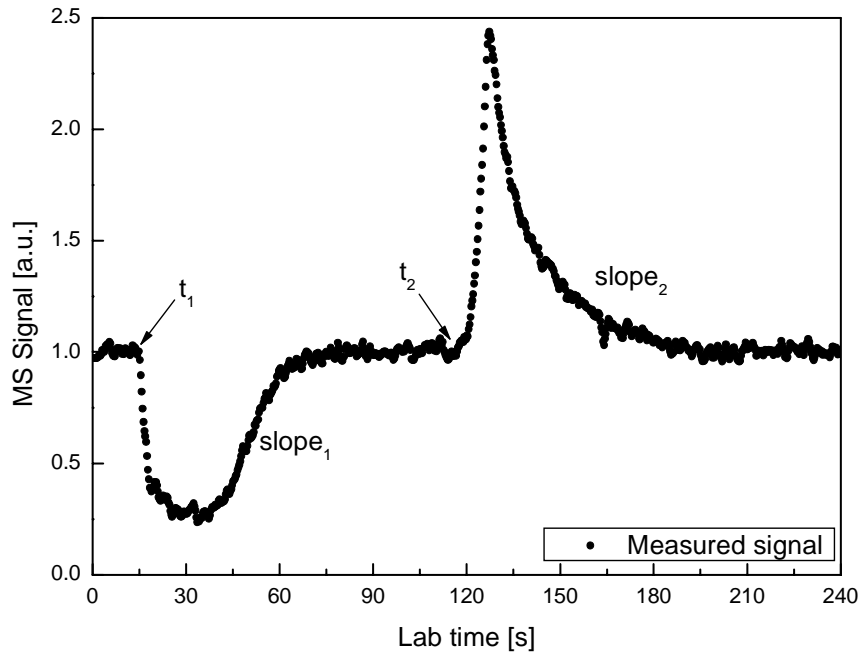
Figure 4.26. A profile of a typical measurement.

4.7.2. Variation of the adsorption rate coefficient

As was presented, the adsorption coefficient is proportional to the uptake coefficient, the average speed of gas molecules and the area of one molecule. Whereas the last two terms are theoretically calculated, the uptake coefficient is assumed to be a variable for the fitting procedure. Therefore varying k_{ads} must be considered as the same as varying the uptake coefficient.

The next figure represents the kinetic simulations performed by varying the adsorption rate coefficient while keeping the desorption rate coefficient and the surface coverage constant.

51

Figure 4.27. Model simulations performed by varying only the adsorption rate coefficient by factors 2 and 10.

The simulated spectra were calculated by multiplying the k_{ads} parameter by factors of 0.1, 0.5, 1, 2 and 10. The desorption rate coefficient and the maximal surface coverage were kept constant for the simulations and were assumed to have values of 0.05 s^{-1}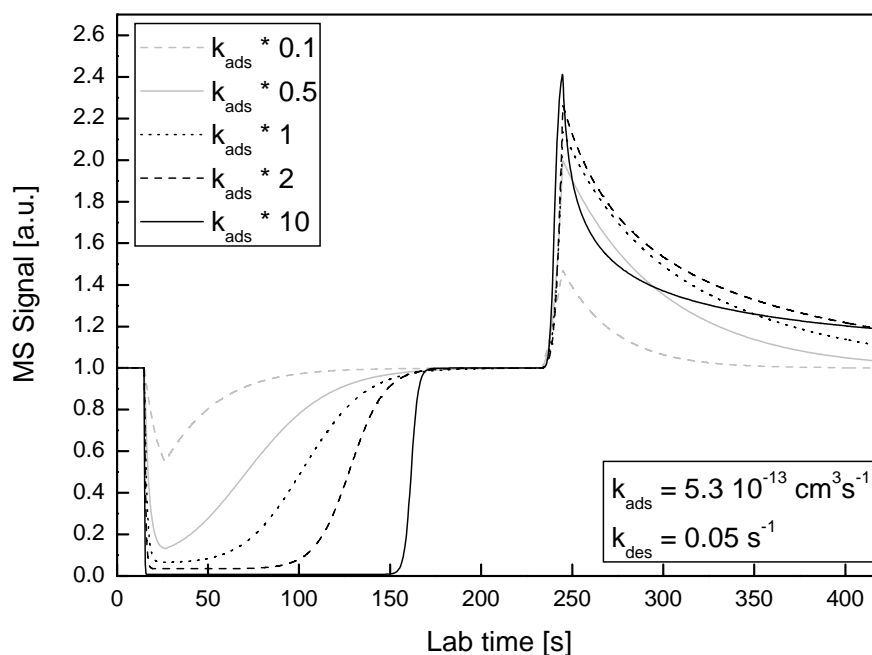 and 9 10^{13} cm^{-2}, respectively. The adsorption areas, and hence the total number of the adsorbed molecules are proportional by the same factor, because the adsorption capacity K_L is proportional to k_{ads} and k_{des}, and K_L is the ratio between the two.

Increasing the signal due to the adsorption in stage 2 or the adsorption when the injector tip is located at the beginning of the tube (or slope$_1$) is also proportional to the adsorption coefficient, i.e. higher k_{ads} leads to faster completion of the equilibrium conditions in the tube and vice versa. In other words, the slope$_1$ is the most sensitive to the k_{ads} value.

An analysis of the desorption drop (or slope$_2$) in dependence on k_{ads} change is represented on the next figure.
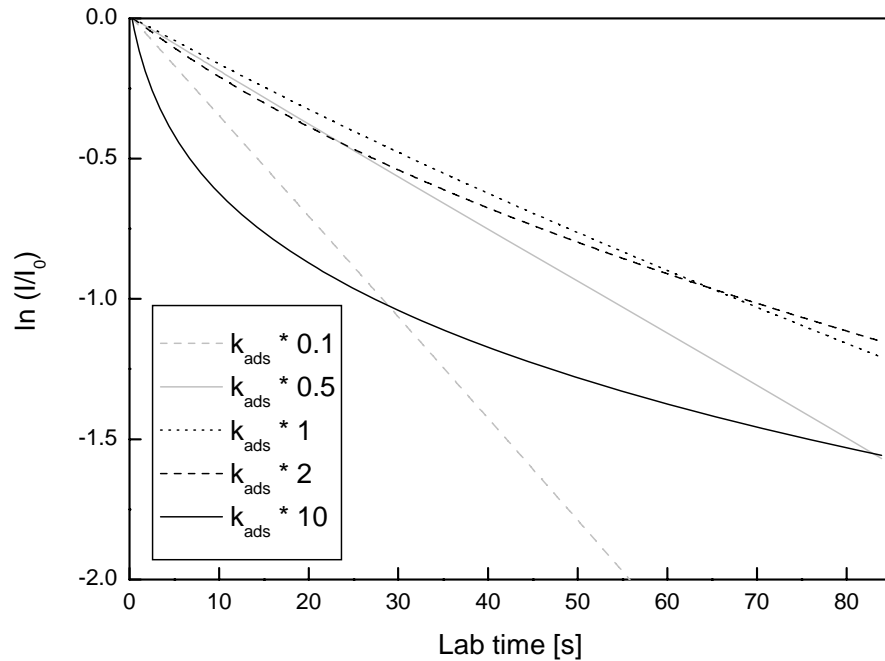
Fig 4.28. Logarithmic representation of the desorption signals performed for different adsorption rate constants.

The figure clearly shows that the measured drop of the signal during desorption is first order only for low values of the adsorption rate coefficient. Although the desorption drop is mostly dependent on k_{des}, some conclusions on k_{ads} can hence be made as well.

4.7.3. Variation of the desorption rate coefficient

The desorption rate coefficient is linearly proportional to the frequency factor and exponentially proportional to $-E_{act}/RT$. The activation energy E_{act} can be calculated from the Arrhenius plot of k_{des} versus $1/T$. Therefore the value of k_{ads} which is being varied is the frequency factor.
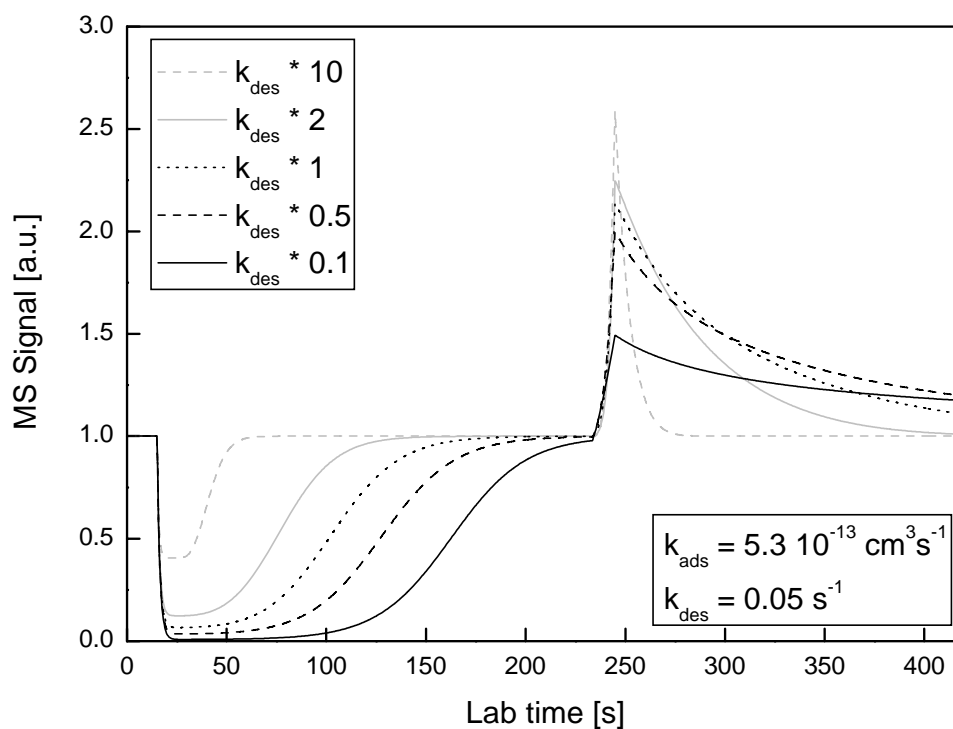
Figure 4.29. Model simulations performed by varying the desorption rate coefficient by different factors between 0.1 and 10.0.

The plots were calculated by varying the desorption coefficient by factors 0.1, 0.5, 1, 2 and 10. The k_{ads} value and the maximum surface coverage were kept constant. The number of adsorbed molecules is inversely proportional to the value of k_{des} . As can be seen from the figure, the slope of the signal (slope$_1$) is only slightly dependent of desorption coefficient. The desorption rate influences mostly the measured signal in stage 4 (static desorption). This is shown on the next figure.
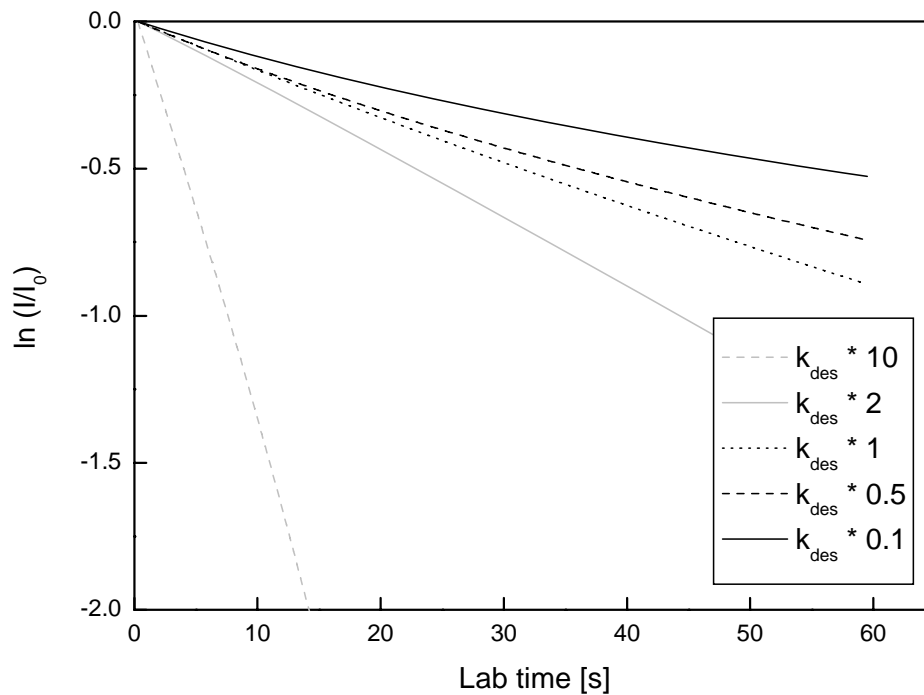
Fig 4.30. Logarithmic representation of the desorption signals performed for different desorption rate coefficients.

The plots are similar to lines with slopes proportional to the desorption coefficients for each. This part of the measured profiles (stage 4) is the most relative to varying k_{des}.

4.7.4. Variation of the maximum surface coverage

Even when both, $slope_1$ (mostly for extracting k_{ads}) and $slope_2$ (for k_{des}), are well fitted, one more parameter, usually the maximum surface coverage ($c_{s,max}$), is still needed. Since the areas correlate to the number of adsorbed (respectively desorbed) molecules it is this parameter which is supposed to be varied.

The next figure represents the simulations performed for varying the maximum surface coverage while the adsorption / desorption rates are kept constant.

55
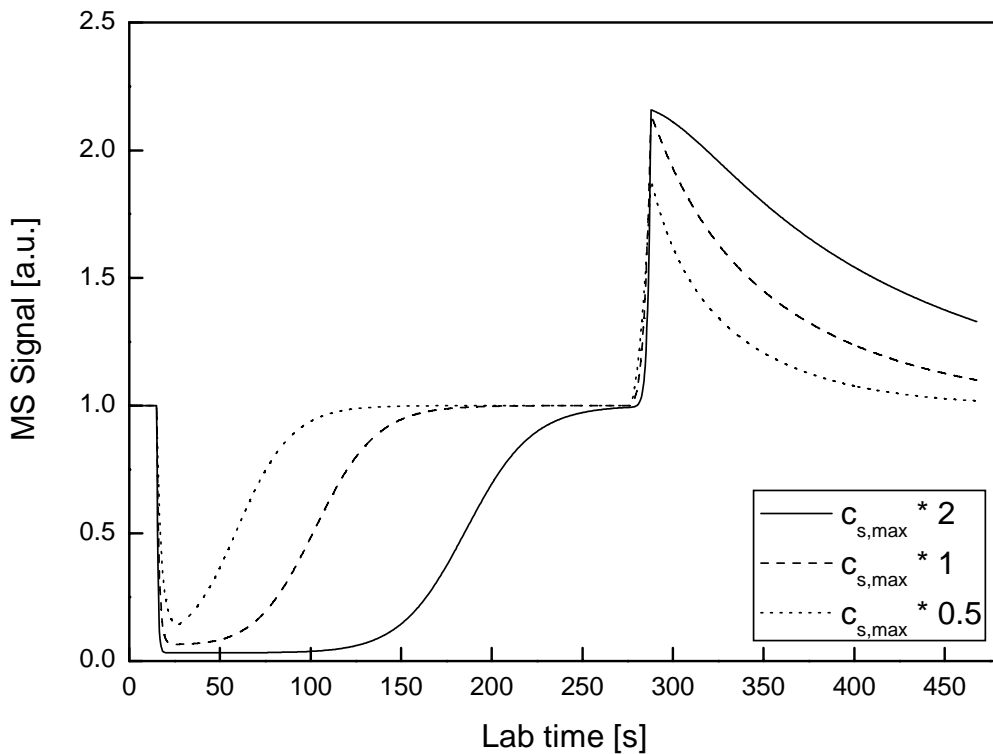
Figure 4.31. Model simulations performed by varying the maximum surface concentration by different factors.

The simulations show that adsorption and desorption slopes are not influenced by changing the maximum surface coverage. The maximum surface coverage should be changed however, in order to adjust the kinetic fit when the adsorption and desorption coefficients are fixed.

4.7.5. Sensitivity analysis of the kinetic model

The demonstrated change of the three kinetic parameters clearly shows their influence to the calculated signal. However, the adsorption capacity and the absolute number of adsorbed molecules strongly depend on the Langmuir equilibrium constant K_L which is the ratio between the adsorption and desorption coefficients ($K_L=k_{ads}/k_{des}$). The next figure shows the default fit (the bold line) and how the adsorption/desorption rates varied by keeping K_L unchanged.

56
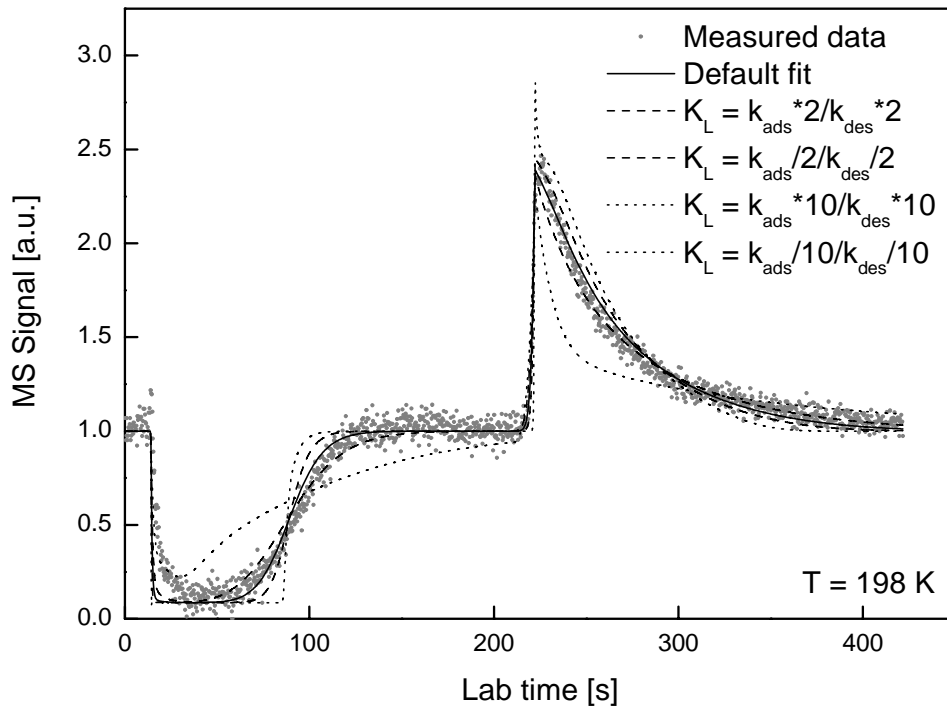
Figure 4.32. Sensitivity of adsorption/desorption peak profiles of acetone on ice surfaces on the rate coefficients k_{ads} and k_{des} at T = 198 K. The areas under the peaks have been fixed at $7.3x10^{13}$ molecules/cm² as given by the Langmuir constant and a gas phase concentration of acetone of c_{gas} = $2x10^{11}$ molecules/cm³.

The performed simulations are clearly distinguishable from the measured data, although their ratios have been kept constant. The different kinetic profiles refer to the same number of adsorbed molecules, which correlates only with K_L and $c_{s,max}$. Another sensitivity test is by simultaneous variation of the adsorption rate coefficient and the maximal surface coverage in order to keep the adsorbed molecules constant. The simulation (of next figure) clearly shows different slopes in the time dependent saturation of the tube when the injector tip is located at the beginning of the tube reactor (slope$_1$). The reason for this, as was discussed above, is that the adsorption rate coefficient k_{ads} mostly modifies the shape of the adsorption peak rather than that of the desorption peak. The slope$_1$ is clearly distinguishable from the three simulations within the error interval of less than 50%.

57

Figure 4.33. Model simulations performed by varying the maximum surface concentration and adsorption rate coefficient by different factors and keeping the number of adsorbed molecules constant.

The last sensitivity test can be made by keeping the equilibrium adsorption / desorption rates constant while varying k_{des} and $c_{s,max}$. The next figure shows the influence of the desorption coefficient to the simulated profile as calculated for three different conditions. The bold line is the default fit and the next two, are for maximum surface coverages of $0.65 \cdot 10^{13}$ and $1.35 \cdot 10^{13}$ cm^{-2} with the desorption coefficients divided and multiplied by factor 2, respectively. The graph presented in the next figure clearly shows the distinction between the spectra in the desorption area and slope$_2$ on the diagram. The change of k_{des} influences mostly the desorption signal while, the adsorption peak shape is more independent of this kinetic parameter.
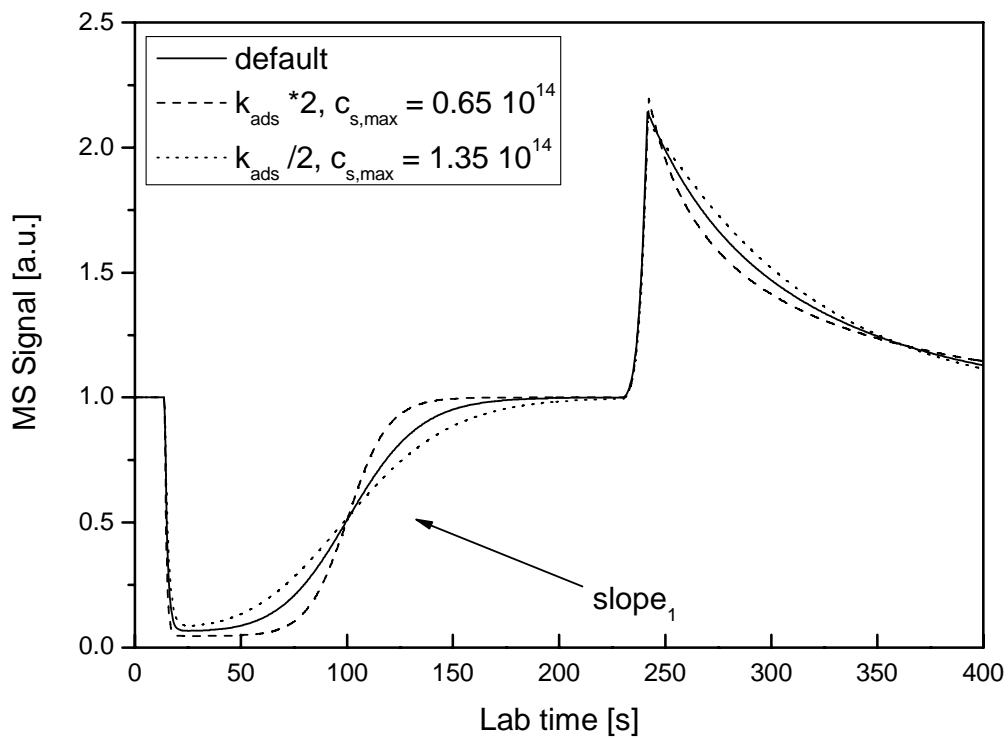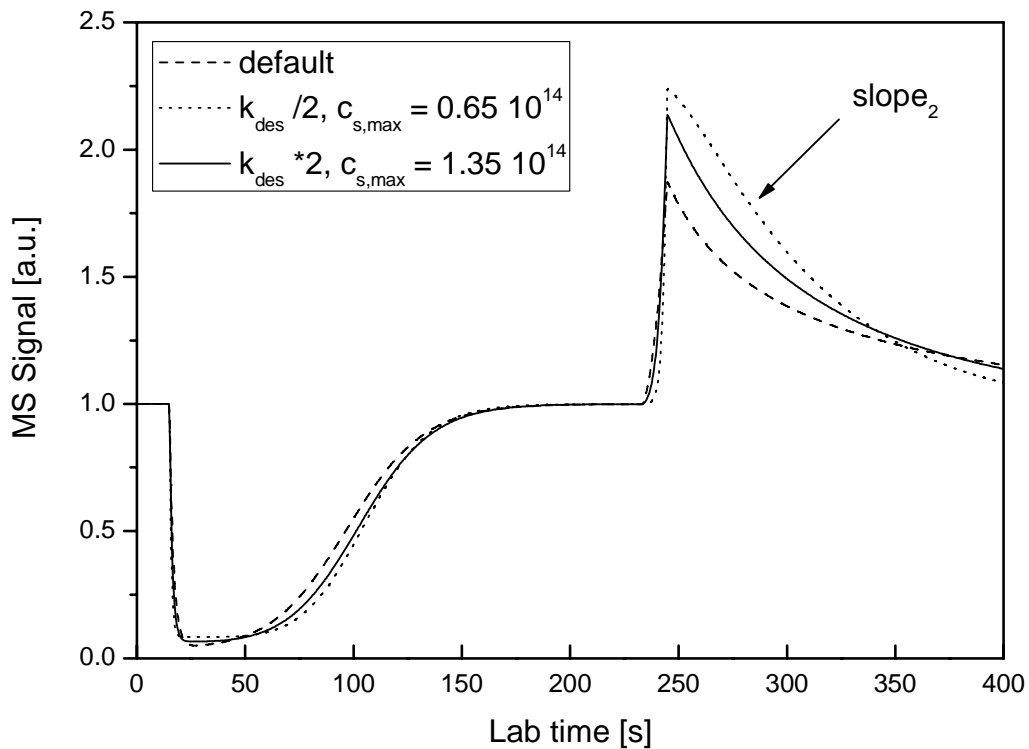
Figure 4.34. Model simulations performed by varying the maximum surface concentration and desorption rate coefficient by different factors while keeping the number of adsorbed molecules constant.

4.7.6. The two adsorption sites model

In this case the number of variables is twice as large with k_{ads}, k_{des} and $c_{s,max}$ for each of the two surface sites and the fitting procedure is also much more complicated.

Measurement conditions			Approximations
Gas phase Concentration	Temperature	Age of the ice surface	
Low	Low	Fresh	Adsorption only on ice cubic sites (I_c)
Low	High	Aged	Adsorption only on hexagonal ice sites (I_h)
High	High	Aged	Adsorption mostly on I_h

Table 4.1. Connections between measured conditions and acceptable assumptions.

The simulated profile is a function of all six parameters as well as their influences and interactions which lead to a more unclear and complicated

59

output. However the measurements under the conditions of only three parameters have been selected and this therefore simplified the task. As it is comprehensively described in the next chapter, the following general conditions are assumed as described in table 4.1.

Initially reliable kinetic parameters based on these extreme cases have been extracted. The second iteration of the fitting was to apply the extracted parameters to the other cases.

5. Adsorption measurements of acetone on ice surfaces

One of the purposes of the present work was to measure adsorption isotherms for acetone on ice in order to extract the enthalpy of interaction and to predict the amount of acetone adsorbed on ice surfaces under different temperature conditions. The temperature range has been varied between 190 – 223 K, and the gas phase concentration of acetone was between $5 \cdot 10^{10}$ to $5 \cdot 10^{13}$ cm^{-3}. Moreover, additional influences to the adsorption capacity of acetone on ice such as ageing and ice thickness effects have also been studied. The kinetic model described above was used to extract the kinetic parameters such as adsorption and desorption rate coefficients and the surface coverage, respectively.

5.1. Langmuir adsorption isotherms

In phase partitioning the gas phase (c_g) and surface concentration (c_s) are in dynamic equilibrium. The connection between c_s and c_g is given by the Langmuir theory and can be expressed by the following relation:

$$c_s = \frac{K_L c_g}{1 + K_L c_g} c_{s,max}$$

where K_L is the temperature dependent equilibrium constant for the adsorption / desorption processes ($K_L = k_{ads}/k_{des}$) and $c_{s,max}$ is the maximal possible concentration of surface sites. A graphical plot of this equation as calculated for two different maximum surface coverages of $1 \cdot 10^{14}$ and $0.5 \cdot 10^{14}$ cm^{-2} and for two different values of K_L ($3 \cdot 10^{-11}$ and $1 \cdot 10^{-11}$ cm^3) is shown on the next figure.
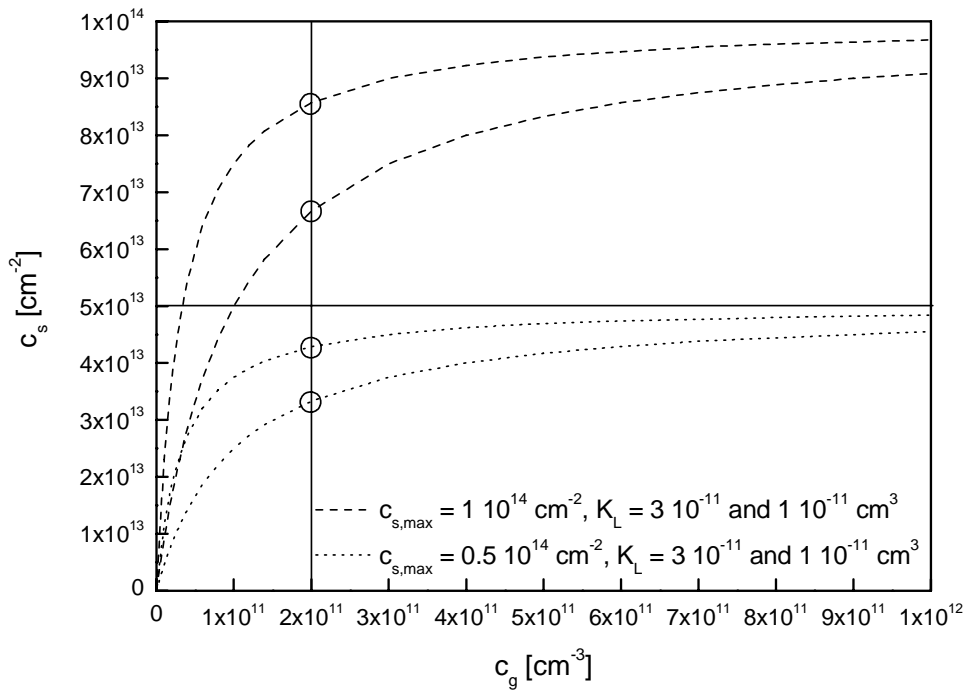
Figure 5.1. A theoretical plot of Langmuir isotherms for different values of the parameters $c_{s,max}$ and K_L.

The diagram shows a faster increase of the number of adsorbed molecules (c_s) for higher Langmuir constants. Keeping the gas phase concentration constant (for example at $2 \cdot 10^{11}$ cm^{-3}), the surface concentration is proportional only to the Langmuir constant, and the absolute number of adsorbed molecules is higher for the higher maximum surface coverage. By increasing the gas phase concentration to infinity in a theoretical case, the number of molecules that can be adsorbed on the surface i.e. $c_{s,max}$, has been reached. It is important to note that the equilibrium between c_s and c_g depends only on the ratio between the two kinetic parameters k_{ads}/k_{des} and not on their absolute values.

A large number (between 1500 and 2000) of measurements were performed in order to extract reproducible data of thermodynamic parameters which describe acetone adsorption for different gas concentrations and temperatures. The absolute number of adsorbed molecules was initially found

by evaluating the adsorption peak (stage 1 and 2) of each measurement. The area under this peak represents the total number of adsorbed molecules corresponding to the equilibrium condition at fixed gas phase and maximum surface concentration and temperature. These areas were calculated by integrating each point as shown on the next figure.
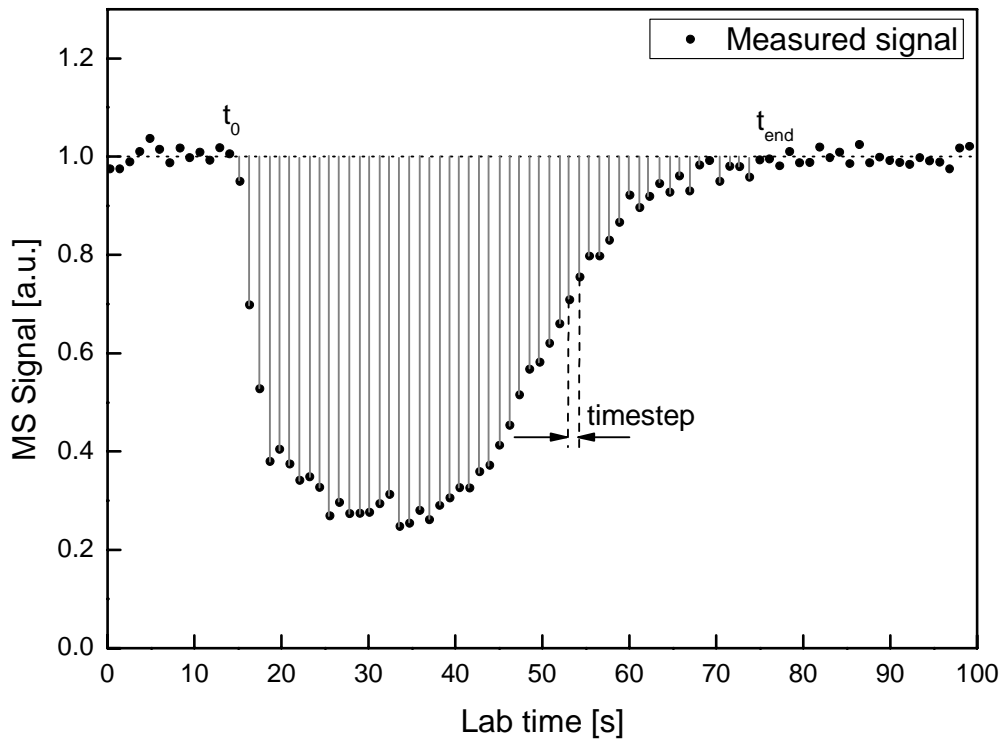
Figure 5.2. Schematic representation of the procedure of calculating the total area the adsorption peak.

The sum of the gray color lines, multiplied by the total number of acetone molecules which have entered the reactor (F_{max}) will give the total number of adsorbed molecules (N_{ads}) in the reactor tube during the Stages 1 and 2. This can be presented by the equation

$$N_{ads} = F_{max} \frac{1}{\text{timestep}} \sum_{t_0}^{t_{end}} (1 - \text{Signal})$$

where "Signal" is the measured and normalized (from 0 to 1) signal, t_0 and t_{end} are the integration times, respectively, and F_{max} is the maximum number of

63

molecules which have entered the reactor tube in the time interval (t_{end}-t_0), calculated with the equation

$$F_{max} = \pi \, r^2 \, v_{flow} \, c_{gas} \, (t_{end} - t_0)$$

The time step is the step of discrete increase of the laboratory time. For this experimental setup and the typical measurements performed it is about 0.2 s, i.e. about 5 measured points per second. The absolute numbers of adsorbed molecules (N_{ads}) divided to reactor area gives the surface concentration

$$c_s = \frac{N_{ads}}{2 \, \pi \, r \, l_r}$$

where l_r is the reactor length. The surface concentrations derived for constant temperature have been plotted against the gas phase concentration. Further fit of the data was made in order to extract the Langmuir constant and the maximum surface coverage.

Desorption peaks were analyzed in the same way as applied to the adsorption peaks. The areas corresponding to the total number of adsorbed and desorbed molecules are identical within the experimental error interval. Hence the conclusion can be made that the thermodynamical processes which occur in the reactor are fully reversible. No evidence for a permanent loss of acetone molecules have been found under these experimental conditions.

5.2. Adsorption / desorption processes and ageing effects

An important conclusion based on Langmuir theory is that the surface coverage and maximum number of adsorbed molecules are proportional only to the temperature Langmuir constant, the gas phase concentration and the maximum number of free active sites on the surface. In other words, if the gas concentration and the temperature are constant, the number of adsorbed molecules correlating with the surface coverage on the same ice surface shall be constant as well. Usually the daily measurements were performed with the same ice film.

Large discrepancies have been found in the adsorption capacity of acetone on fresh ice surfaces compared to aged ice at the end of the day.

Depending on the temperature and the gas phase concentration, the adsorption ability has been found to decrease by a factor of 8 for aged ice, compared to fresh ice. In this chapter a more detailed experimental proof for different conditions will be given. The two typical measurements performed on fresh and aged ice surfaces are presented on figure 5.3.
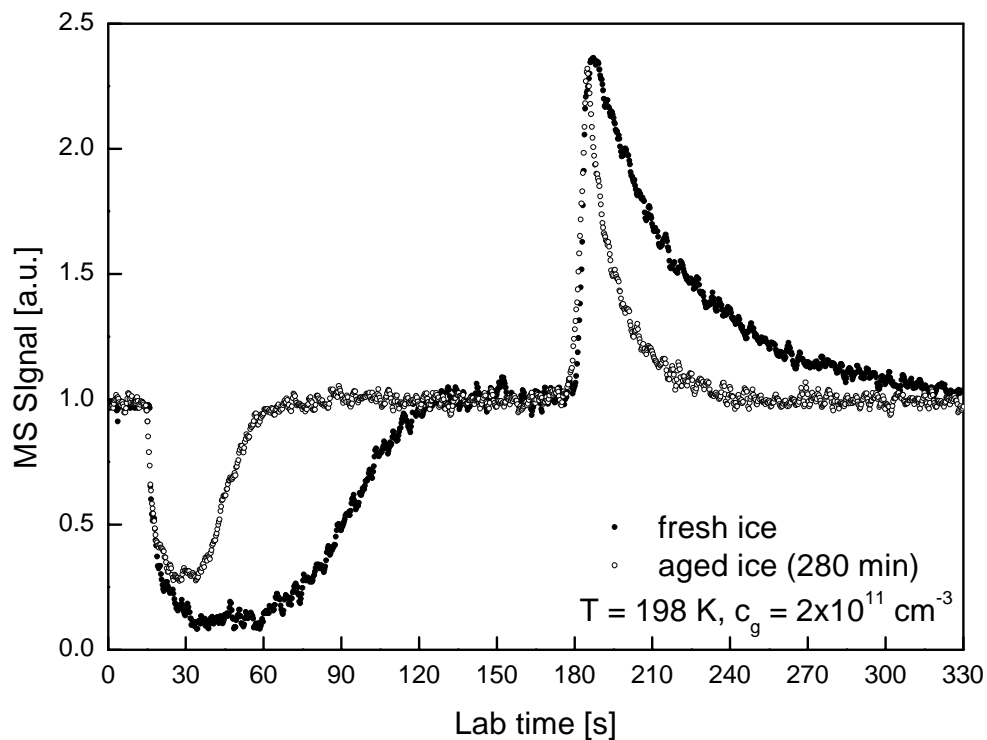
Figure 5.3. Adsorption and desorption profiles for acetone on ice at T = 198 K and c_g = 2x10^{11} cm^{-3} as obtained by moving the injector sequentially in up-stream and down-stream direction. The two profiles are for different ages of the ice surface and correspond to a total number of adsorbed molecules of 7.3 10^{13} cm^{-2} and 2.4 10^{13} cm^{-2}, respectively.

The figure compares two measurements taken under the same conditions with the time difference of 280 minutes. The profile taken on fresh ice is the first one registered on a surface immediately after it has been generated. The adsorption capacity drops by a factor of 3 after 280 min of ageing. The estimated surface coverages for both measurements on fresh and aged ice surface are calculated to be about a few percent. The analysis of the logarithmic drops of the two desorption profiles is presented on the next

figure. It clearly shows the existence of two different first order desorption processes.
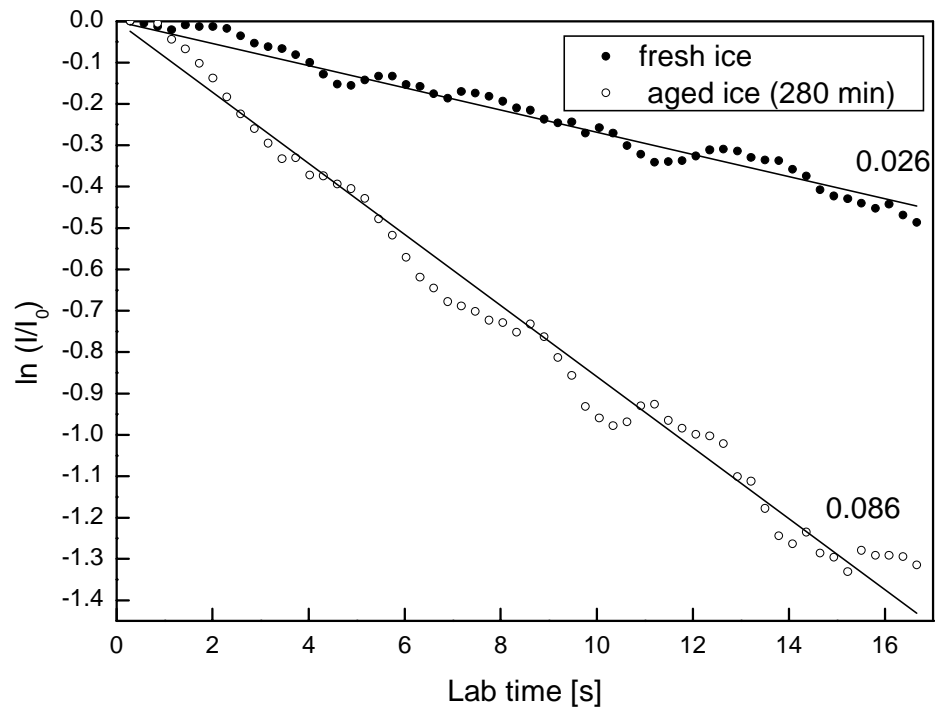
Figure 5.4. Logarithmic plot of the decay of the desorption signal for fresh and aged ice.

The same experiment was repeated for a one order of magnitude higher gas phase concentration (Figure 5.5.). The area corresponding to the absolute number of adsorbed molecules for aged ice is about 25% less compared to the fresh ice case. This number is nearly identical to the one observed in the experiment for lower acetone concentrations, although in that case the ageing effects affected the total number of adsorbed molecules by about 33%.

The observed ageing effect in the experiments at lower temperatures occurs on the time scale of hours. In order to study ageing processes of the ice surfaces, the ageing time or the relative laboratory time (RLT) between the

measurements have been systematically varied by keeping other parameters constant.
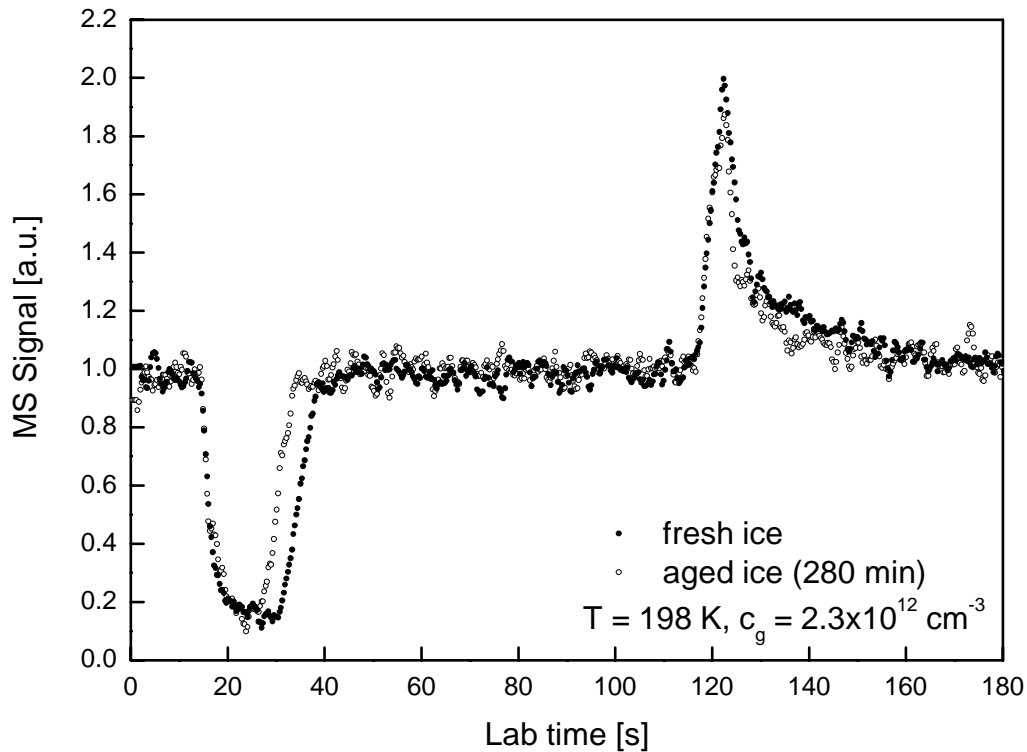
Figure 5.5. Same as for Figure 5.4 but for an acetone concentration of 1.6 10^{13} cm^{-3}. The change of the adsorption capacity due to ageing amounts to approximately 5 10^{13} cm^{-2}.

The resulting adsorption capacity has been measured in each single measurement, i.e. the number of acetone molecules adsorbed. The resulting variation of this capacity as a function of relative laboratory time is shown in Figure 5.6.

As can be seen from these experiments, this capacity decreases with a time constant of ~50 min, and hence an ageing rate constant of ~0.02 min^{-1}, at T = 198 K. About 60% of the initial capacity has been lost after ageing. The figure also shows the result of a simulation study for the temporal change of the maximum number of cubic adsorption sites ($c_{s,max}(I_c)$) using a dynamic two-site model as described in chapter 4. The parameters used to describe this change are $k_{ads}(I_c)$ = 5.4 10^{-13} cm^{3}s^{-1}, $k_{ads}(I_h)$ = 3.0 10^{-14} cm^{3}s^{-1}, $k_{des}(I_c)$ = 0.31 s^{-1},

$k_{des}(I_h) = 0.1$ s^{-1}, $c_{s,max}(I_c)$ up to 1.0 10^{14} cm^{-2} (depending on RLT) and $c_{s,max}(I_h) = 6.0$ 10^{14} cm^{-2}.
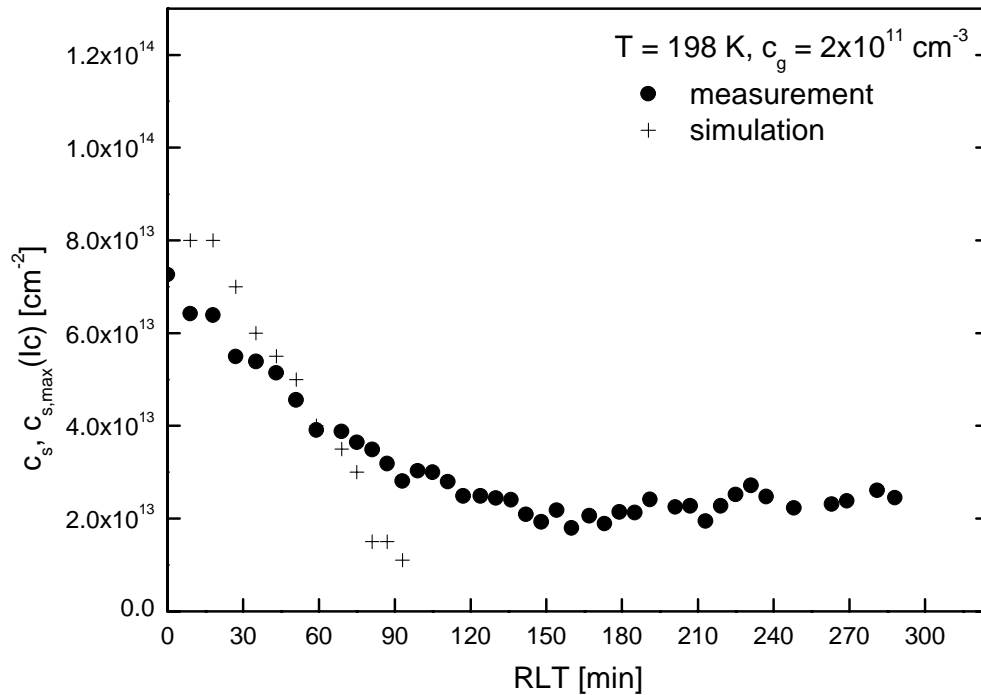
Figure 5.6. Temporal variation of the adsorption capacity (no. of molecules of acetone adsorbed per cm²) of ice as a function of the age of the ice surface as expressed by the relative laboratory time (RLT). T = 198 K, c_g = 2.0 10¹¹ cm⁻³. Comparison of measured (•) and simulated data (+) using a two-adsorption site model.

As can be seen from the figure, the adsorption capacity is influenced by the ageing only up to 150 minutes of RLT and stays constant at about 2 10^{13} cm^{-2} of equilibrium surface concentration afterwards. The time of reaching constant ice surface conditions is shorter at higher temperatures.

5.3. Adsorption isotherms for differently aged ice surfaces

Measuring the adsorption isotherms for differently aged surfaces at different concentration and temperature ranges became one of the major objectives of the present work. The next figure presents the isothermal change for 193K on fresh ice surface for a concentration range of up to 3.5 10^{13} cm^{-3} of acetone molecules.
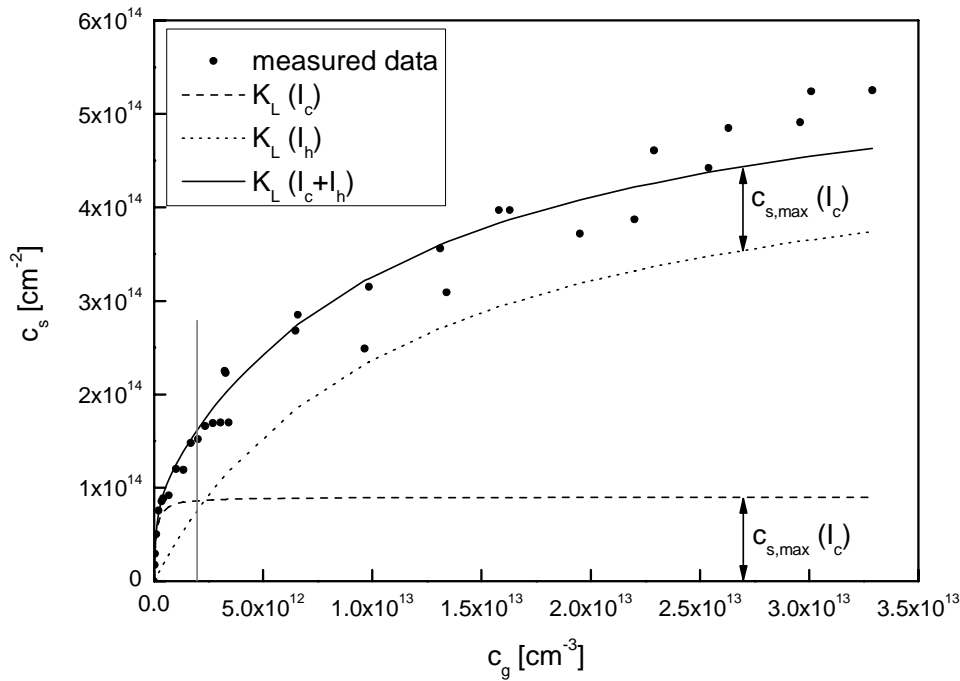
Figure 5.7. Adsorption isotherm of acetone on fresh ice surfaces at 193 K (black dots) and thermodynamical fit of the data.

The dashed line represents the adsorption of acetone on cubic ice surface sites, calculated for K_L = 11.6 10^{-12} cm^3 and $c_{s,max}$ = 9 10^{13} cm^{-2} and the dotted line accounts for the adsorption of acetone on hexagonal ice with the parameters K_L = 8 10^{-14} cm^3 and $c_{s,max}$ = 5.3 10^{14} cm^{-2}. The bold line is a sum of both adsorption on cubic and hexagonal sites, hence the total thermodynamic equation is

$$C_s = \frac{K_{L(I_c)}C_g}{1+K_{L(I_c)}C_g}C_{s,max(I_c)} + \frac{K_{L(I_h)}C_g}{1+K_{L(I_h)}C_g}C_{s,max(I_h)}$$

As can be seen, for lower gas phase concentrations adsorption is mainly on cubic sites, because the adsorption rate is higher for these sites. By increasing the concentration the adsorption occurs more and more on hexagonal sites, because the cubic surface sites are lower in total number ($c_{s,max}$ for I_c is one order of magnitude smaller than $c_{s,max}$ for I_h). In the higher concentration range the resulting isotherm is shifted parallel with the maximum number of

69

cubic sites. The next figure is a magnification of the previous one in the concentration range up to $2 \cdot 10^{12}$ cm^{-3}.
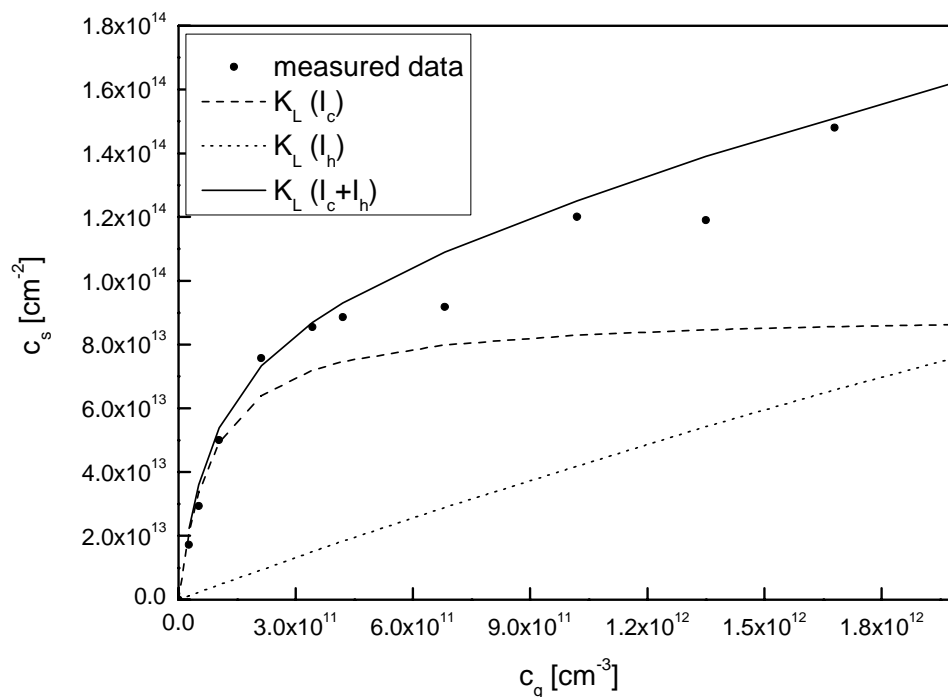
Figure 5.8. The Same as fig 5.7 zoomed in the concentration interval up to 2 10^{12} cm^{-3}.

The adsorption of hexagonal sites does not occur in the low gas phase concentration range.

The next figure shows the measured adsorption isotherm at T = 193 K for a range of acetone concentrations of less than $2.3 \cdot 10^{12}$ cm^{-3} and for a number of different ages of the ice surface. The measured data are enormously scattered if taken as measured and if the age of the ice surface is left unconsidered. After sorting by relative lab time, single isotherms become clear from which Langmuir constants (K_L) and maximum coverages ($c_{s,max}$) can be extracted.
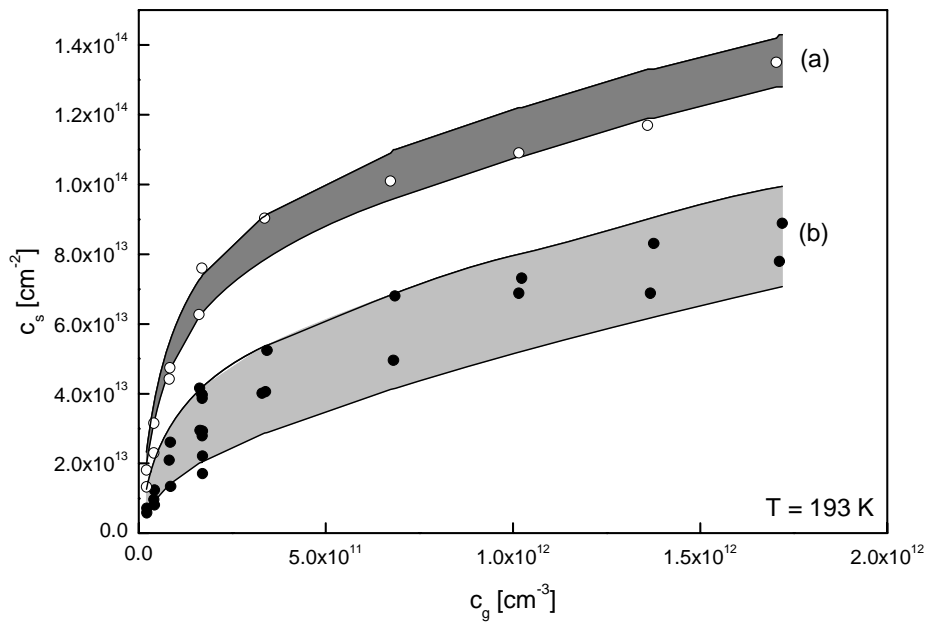
Figure 5.9. Langmuir plot for acetone adsorption on ice surfaces at T = 193 K and gas phase concentration below $2 \cdot 10^{12}$ cm^{-3}. The data encompassed by the different curves are (a) for a fresh ice surface (~ 30 min) and (b) an aged ice surface (~220 min). Within each of the shaded areas $c_{s,max}(I_c)$ changes from $9.5 \cdot 10^{13}$ to $8 \cdot 10^{13}$ cm^{-2} in case (a) and from $5 \cdot 10^{13}$ to $2 \cdot 10^{13}$ cm^{-2} in case (b).
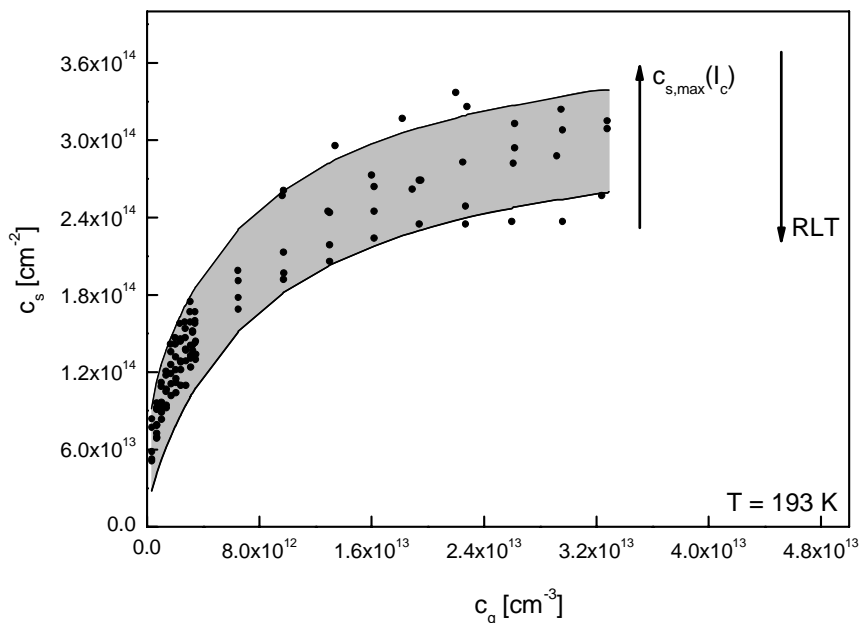
Figure 5.10. Same as Fig. 5.9 but for an extended scale of the concentrations. The data shown are obtained for ages of the ice surface between 5-300 min. The upper and lower boundary of the shaded area correspond to $c_{s,max}(I_c)=10 \cdot 10^{13}$ cm^{-2} and $2 \cdot 10^{13}$ cm^{-2}, respectively. In each case $c_{s,max}(I_h)=3 \cdot 10^{14}$ cm^{-2}.

71

This figure presents an extension of the data from the previous figure (5.9) up to $3.2 \cdot 10^{13}$ cm^{-3} of acetone gas phase concentration. An important point here is that for the aged isotherm the maximum surface concentration is almost reached (more than 80% surface coverage). The curves represent the upper and lower boundaries of the isotherms, which correlate with the ageing effect. They have been calculated from a two-site dynamic model in which the maximum number of adsorption sites for cubic ice changes from $10 \cdot 10^{13}$ cm^{-2} to $2 \cdot 10^{13} cm^{-2}$ over the time interval 5 to 300 min, whereas the corresponding number for hexagonal sites is left time invariant at $3 \cdot 10^{14}$ cm^{-2}.
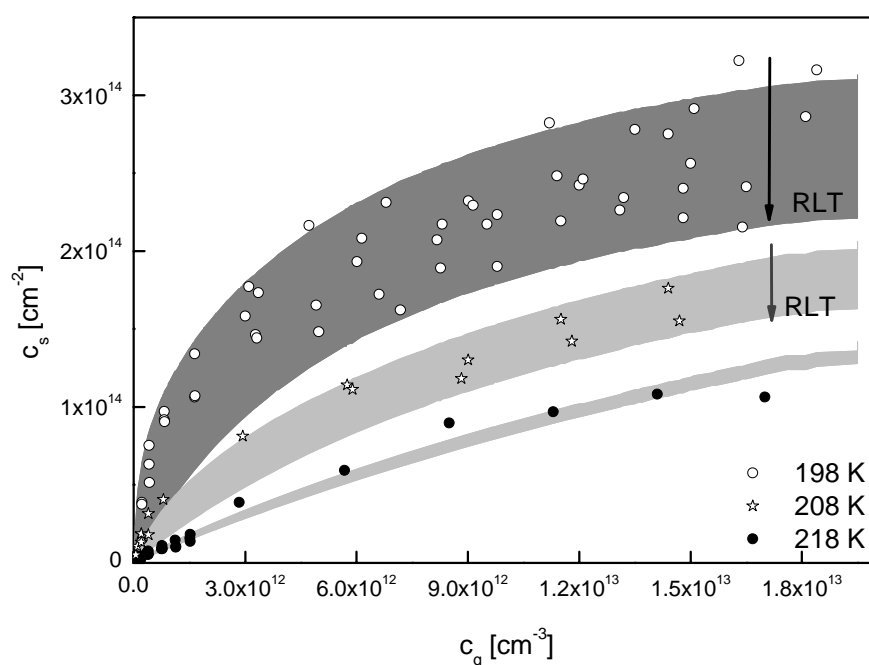
Figure 5.11. Adsorption isotherms for acetone on ice surfaces for temperatures of 198, 208 and 218 K. The upper and lower boundaries of the isotherms at 198 and 208 K reflect fresh (0-5 min) and aged (300 min) ice surfaces, respectively.

As opposed to the adsorption isotherms measured at low temperatures, those measured at higher temperatures showed a much weaker ageing effects. This is shown in 5.11 where the adsorption isotherms for 198, 208 and 218 K has been presented. All the data presented have been taken at ages of the ice surface between 10 and 250 min. As opposed to the data at 198 K for which

there is still substantial ageing, the effect is becoming smaller at 208 K and no longer noticeable for 218 K. The upper boundaries for the isotherms at 198 and 208 K corresponding to initial maximum numbers of adsorption sites of cubic structure at 9 10^{13} cm^{-2} and 4 10^{13} cm^{-2}, respectively. For the lower boundaries this number has been set to zero in each case, corresponding to complete conversion of cubic into hexagonal sites after ageing.

The rate coefficients for desorption from the two different sites are presented graphically in Arrhenius form in the next figure.
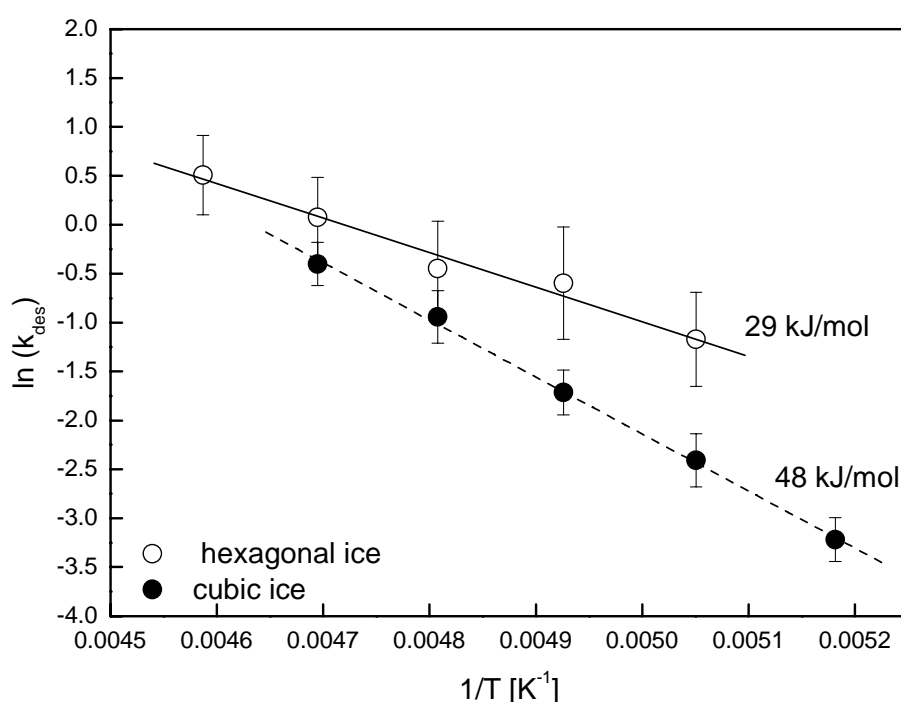
Figure 5.12. Arrhenius representation of desorption rate coefficients of acetone from cubic and hexagonal surface sites of ice

The most interesting information of this plot is the difference in activation energies. Whilst the value for cubic sites is in the order of 49 kJ/mol, the corresponding value for hexagonal ice is only around 30 kJ/mol. If the reverse process of adsorption is assumed to occur without any barrier, as is indicated from our measurements of the temperature dependence of k_{ads}, then this difference is clearly a reflection of the enthalpies of adsorption which is larger

in the case of cubic ice. This is shown in the next figure where we present the van t`Hoff plot of the Langmuir constants for each of the crystalline phases.
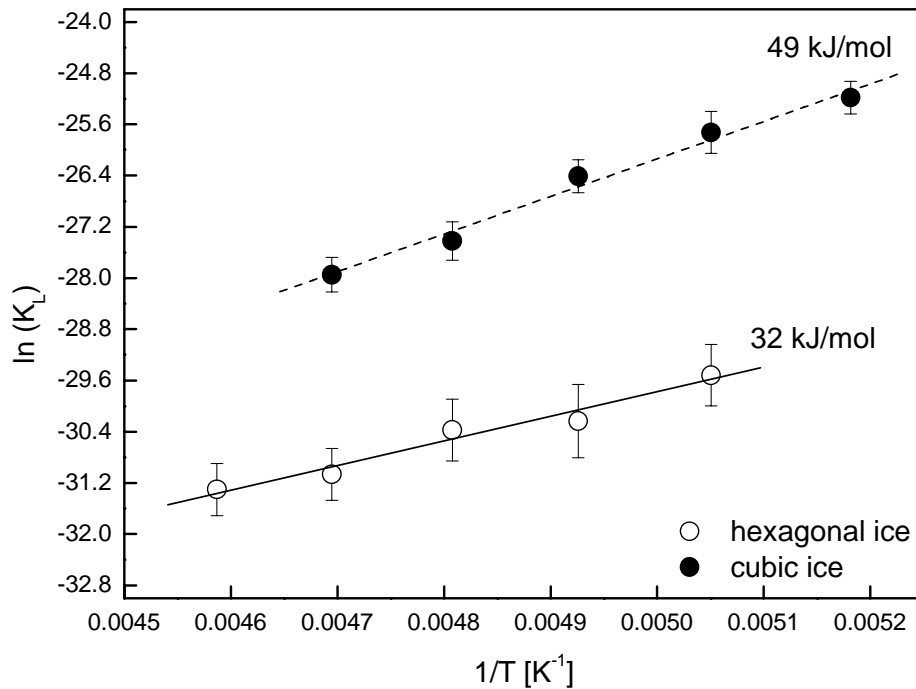
Figure 5.13. Van t'Hoff representation of the Langmuir constants of acetone on cubic and hexagonal surface sites of ice.

5.4. Ice thickness influence on adsorption / desorption processes

Ice thickness is a parameter which is proportional to the coating time of our flow reactor (chapter 3.2). Here we will refer to a coating time instead of mass of ice per reactor area for simplicity. However, it was found that one hour of coating time (for temperature 203K, pressure in the reactor of 3.5 mbar and flow of water vapour of 150 sccm) corresponds to 1 gram of ice in the reactor. In order to study the ice thickness influence on the adsorption capacity we have performed an additional set of measurements for different coating times (from 6 to 180 min of coating), temperature and concentration ranges. The results, together with a theoretical treatment, will be presented for hexagonal and cubic sites, respectively.

5.4.1. Ice thickness influence on hexagonal ice sites

The ice thickness dependence on the maximum number of hexagonal sites ($c_{s,max}$ (I_h)) has been studied for experimental conditions at which we assume only adsorption on hexagonal sites (mainly aged ice surfaces). The next figure presents two measurements of acetone on aged ice (210 min) at 213 K and a gas phase concentration of about $2 \cdot 10^{11}$ cm^{-3}.

Figure 5.14. Measurements and simulations of acetone adsorption on ice surfaces with different thicknesses for 213 K

The open circles present adsorption of acetone on a thinner ice film (30 min of coating) whereas bold circles refer to a thicker film (90 min of coating). The two simulated lines were calculated at constant kinetic parameters (k_{ads} and k_{des}) and different maximum number of hexagonal sites (assuming $c_{s,max}(I_c)=0$). The figure clearly shows that the adsorption / desorption kinetics is independent of the ice thickness, the adsorption capacity, however, is not. Hence we cannot explain the increased adsorption capacity by bulk penetration (chapter 4.6.1). Therefore for the simulations in figure 5.14 the values of $3 \cdot 10^{14}$ and $9 \cdot 10^{14}$ cm^{-2} were assumed for the maximum number of

hexagonal sites $c_{s,max}(I_h)$, respectively for 30 and 90 minutes of coating. The next figure summarizes the relation between the maximum number of hexagonal sites and coating time at different temperatures. The $c_{s,max}(I_h)$ values were extracted by data fitting using the developed kinetic model (chapter 4) applied to adsorption measurements of acetone on aged ice. As can be clearly seen, the maximum number of hexagonal surface sites is proportional to the ice depth (coating time). For still thicker ice films, however, the adsorption capacity, respectively, the maximum number of hexagonal sites tend to become constant.
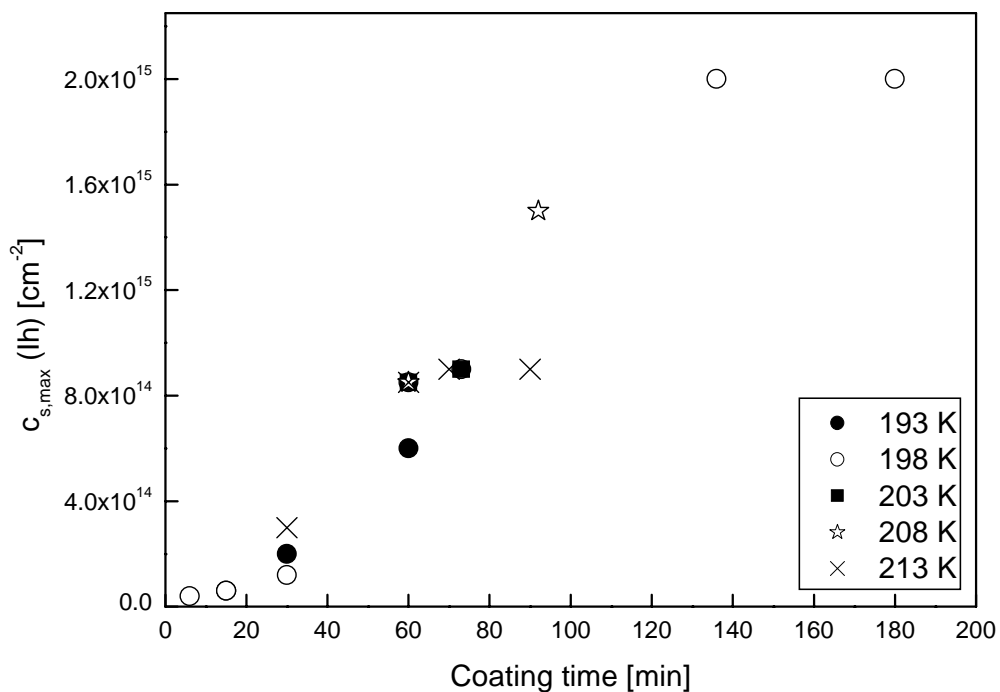
Figure 5.15. Maximum number of hexagonal sites as a function of the ice thickness. Results obtained from kinetic fits of adsorption / desorption profiles.

Keyser and Leu (Keyser and Leu, 1993) consider an increase of the adsorption surface capacity of thicker ice surfaces to be proportional to the increased surface porosity. The calculated pore diffusion coefficient is significantly higher than the adsorption rate coefficient; hence the surface porosity can be included in the kinetic model for which increased adsorbed surface sites

has been assumed. In other words, the adsorption / desorption kinetics is not influenced by the much faster pore diffusion.

5.4.2. Ice thickness influence on cubic ice sites

The same thickness dependence has also been found for the cubic sites. A similar data treatment has been done for adsorption of acetone with low gas phase concentration on fresh ice surfaces. For these conditions we assume preferable adsorption on cubic sites. The next figure presents two measurements of acetone on fresh ice surfaces performed at the same gas phase concentration of $2 \ 10^{11}$ cm^{-3} and temperature of 198 K. The open circles profile corresponds to adsorption on thinner (15 minutes of coating) and bold circles on thicker (60 minutes of coating) ice film.
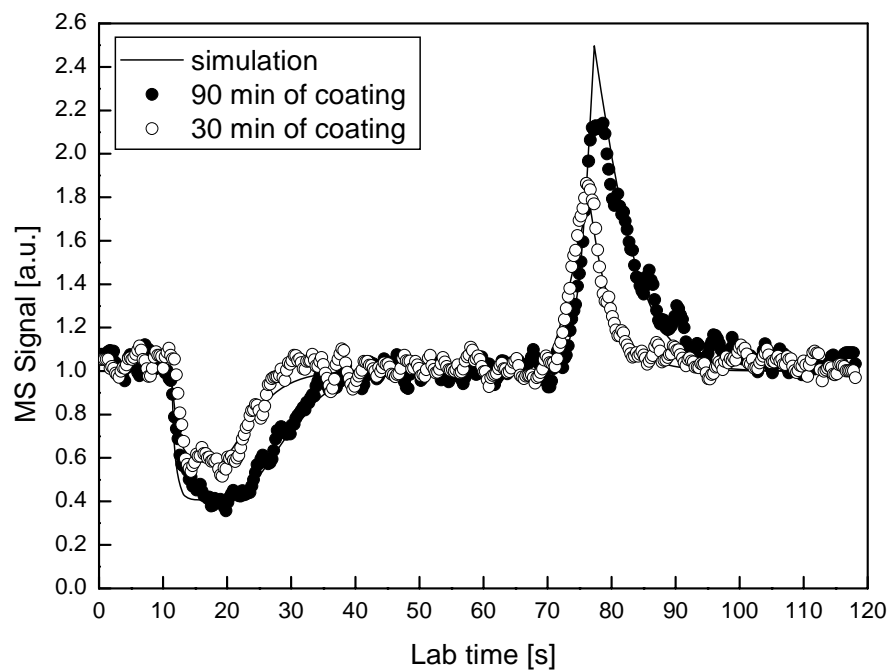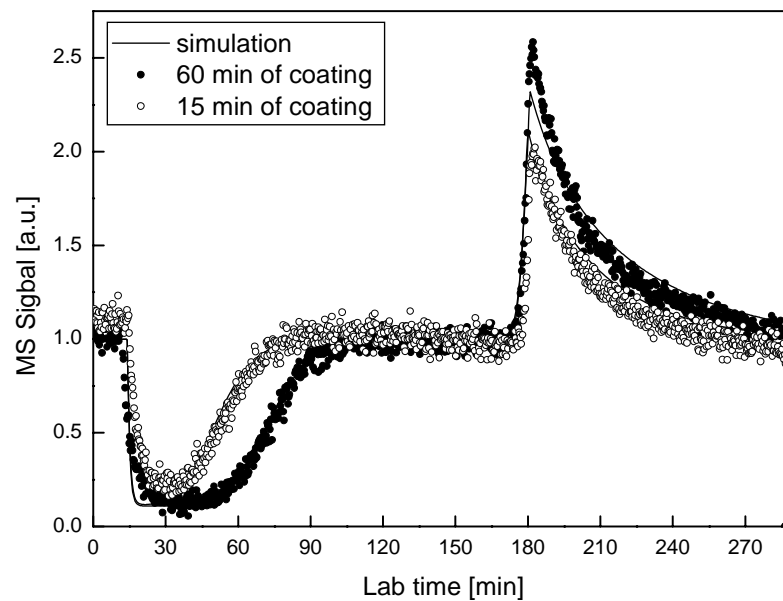

Figure 5.16. Measurements and simulations of acetone adsorption on ice surfaces with different thicknesses for 198 K

The kinetic model has been applied to the two measurements shown on figure 5.16 (the bold lines). For both fits the kinetic parameters for acetone adsorption on cubic sites are as follows: $k_{ads} = 5.4 \ 10^{-13}$ cm^{3}s^{-1} and $k_{des} = 0.1$ s^{-1}. The maximum surface coverage $c_{s,max}(I_c)$ was calculated to be $7.5 \ 10^{13}$ and $12 \ 10^{13}$ cm^{-2} for both thinner and thicker ice film, respectively. Therefore it can

be concluded that the ice thickness influences both the numbers of hexagonal and cubic surface sites. Whereas the number of hexagonal sites depends only on ice thickness, the number of cubic sites is also time dependent. The ageing effect under the experimental conditions was also found to be influenced of the ice film thickness. A theoretical explanation of this experimental observations can be given by the parcel model (Murphy, 2003) in which the formation of both cubic and hexagonal ice forms as a function of relative humidity have been suggested. The following three processes (the next figure) will schematically explain the formation of I_c ice and its conversion into I_h.
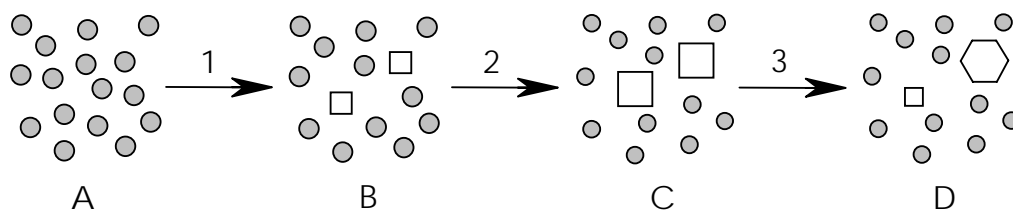
Figure 5.17. A scheme of I_c and I_h formation as suggested by the parcel model.

State "A" from the figure corresponds to relative humidities between 100 to 160%. Such condition of supersaturated water vapour exists in the reactor during the ice film generation where the water vapour (at room temperature) has been injected into the cooled tube reactor. For this condition of low temperature, entered water vapour in the reactor can be considered as super saturated vapour, and to cause instant freezing on the surface. The processes 1 and 2 from figure 5.17 correspond to ice film generation. The deposition of gaseous water forms ice cubic crystals, and their size increases during the coating procedure. The crystal growing process is proportional to the water vapour pressure and the sticking coefficient of water on ice which has been assumed to be averaged value of 0.15 (Murphy, 2003). In other words higher relative humidity contributes to fast crystal growing as well as thicker ice film. The crystal size or edge under the experimental coating conditions varies between 7 and 15 μm for coating times from 6 to 60 minutes (figure 5.18) as shown later. It is important to notice that hexagonal crystals

form also at higher relative humidity, so more or less our fresh ice consists of a mixture of cubic and hexagonal ice crystals.

State "C" corresponds to the surface condition right after generating the ice film. At this stage cubic ice crystals have the biggest size (edge) and this is so called fresh ice surface. The ageing (process 3) starts as soon as the relative humidity is being decreased. Cubic ice crystals have a higher vapour pressure (Murphy, 2003) i.e. they evaporate by a rate corresponding to their volume to surface ratio. Under these conditions the water vapour concentration in the gas phase is not enough to form cubic crystals any more and this is the reason why I_c transfers to I_h.
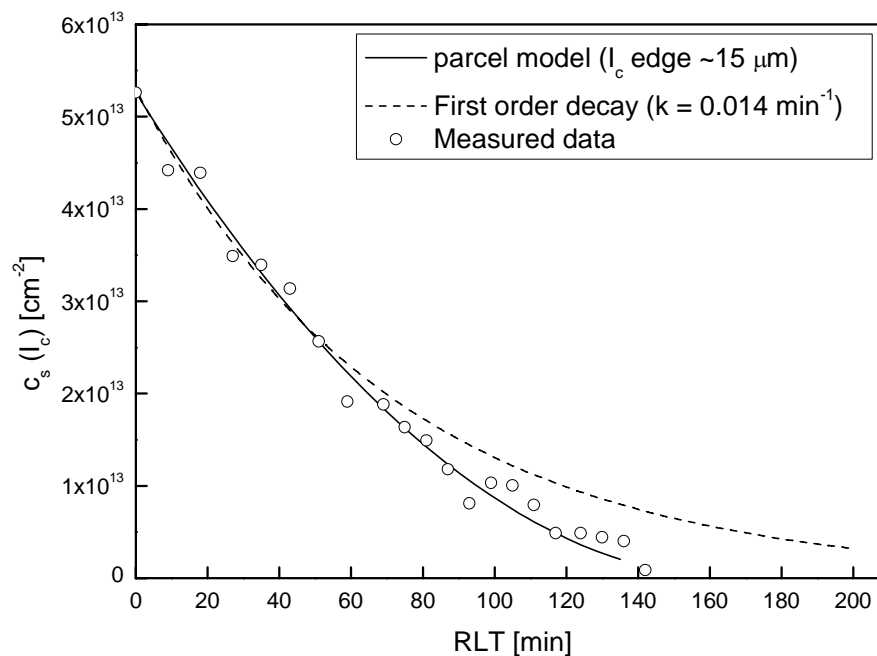
Figure 5.18. Applying the parcel model to ageing measurements performed at T=198 K, c_g=2 10^{11} cm^{-3} and ice film generated for one hour of coating.

Figure 5.18 presents an application of the parcel model to an ageing measurement at 198 K, and for an initial gas phase concentration of 2 10^{11} cm^{-3} and 60 minutes of generating the ice film. The open circles represent the measured adsorbed molecules on cubic surface sites in units of cm^{-2} which correspond to $c_{s,max}(I_c)$. The dashed line is a logarithmic plot for a rate constant of 0.014 min^{-1} which represents first order transformation of cubic to

hexagonal sites. The bold line is the best fit calculated using the parcel model and with the edge of cubic ice crystals as a variable parameter of 15 μm. As can be concluded from the figure, the I_c to I_h transition can not be explained with first order transformation.
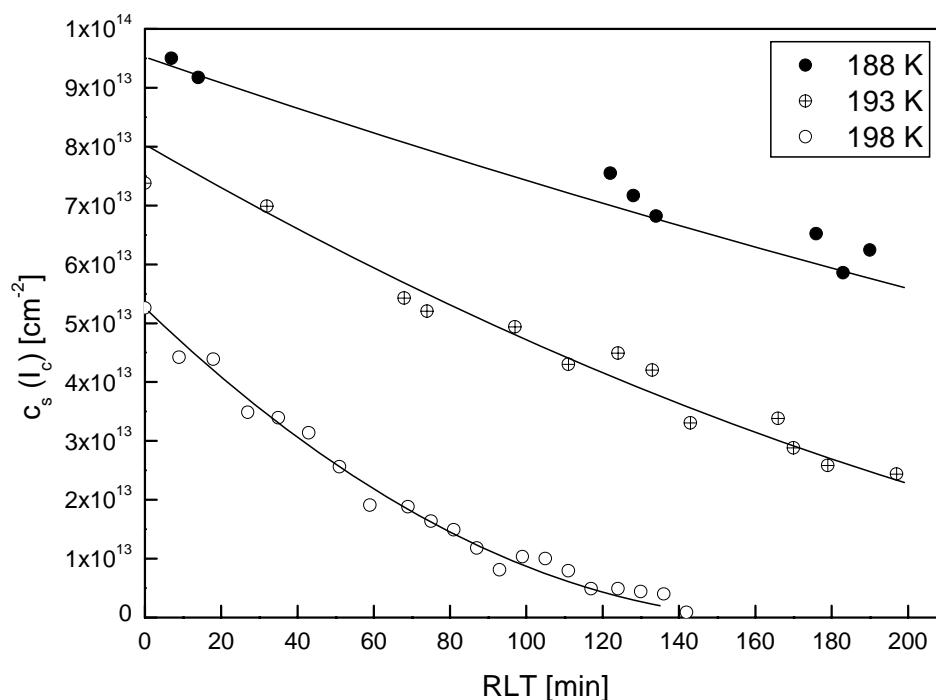
Figure 5.19. Ageing measurements at constant ice depth and different temperatures.

The ageing effect at different temperatures is presented in fig 5.19. As can clearly be seen the cubic sites drop is inversely proportional to temperature. As was explained above the I_c to I_h change is proportional to the evaporation rate of cubic sites which is proportional to temperature. The measured surface concentrations $c_s(I_c)$ and theoretical fits for RLT=0 for the three temperatures are shifted according to the Langmuir constant. In other words when the maximum surface coverage is constant the adsorbed molecules are proportional to the Langmuir constant and inversely proportional to the temperature. According to the parcel model the relative humidity (RH) is the reason for I_c to I_h transformation. On the other hand the RH is proportional to the water vapour pressure and respectively, the k_{ads}/k_{des} ratio of water. The

80

k_{ads} coefficient is also slightly temperature dependent and we can assume it to be a constant at a sticking coefficient fixed to 0.15.
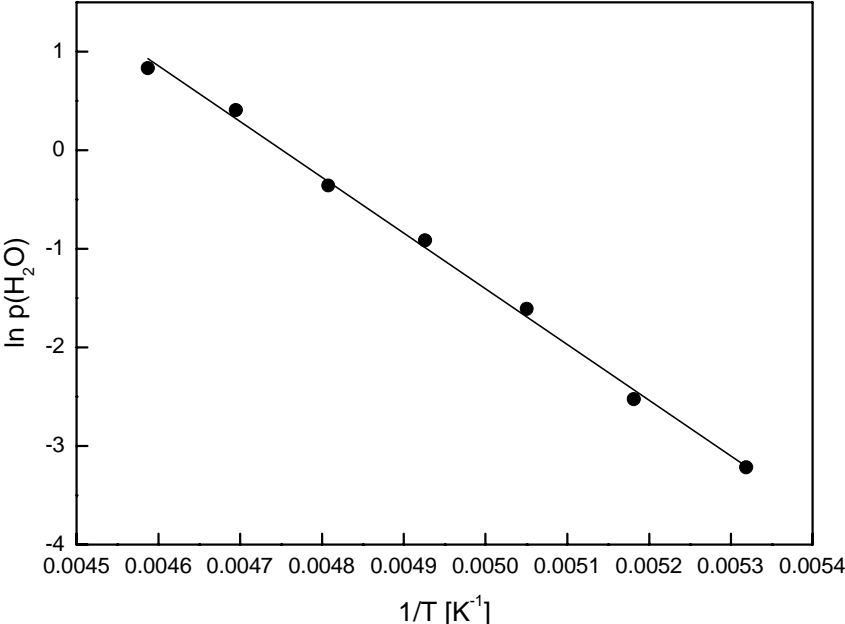
Figure. 5.20. Arrhenius representation of the conversion energy of cubic to hexagonal ice. The slope corresponds to 47 kJ/mol
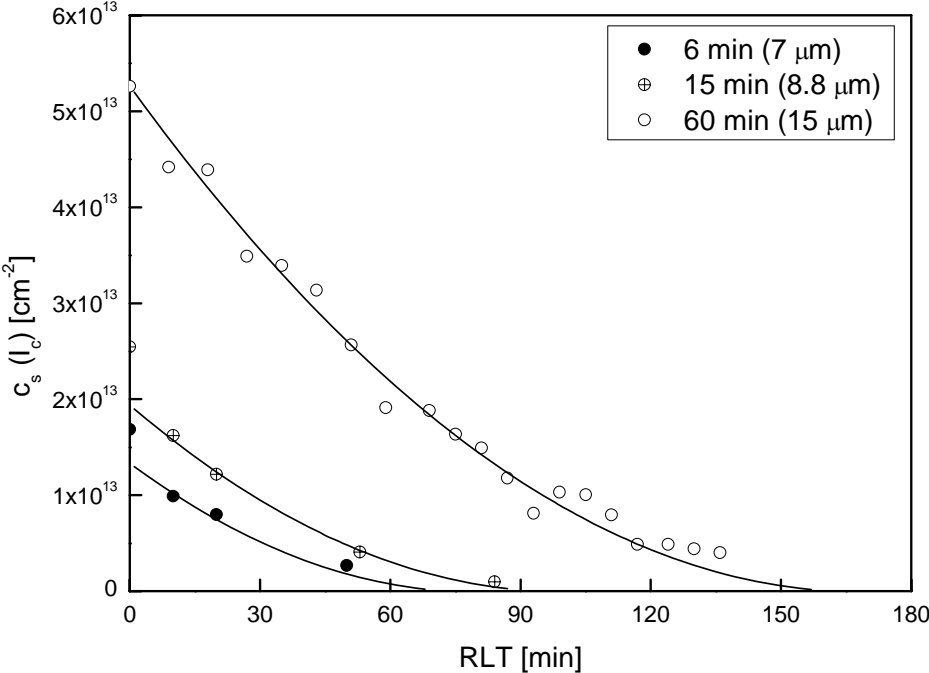
Figure 5.21. Ice thickness (coating time) influence on the ageing at 198 K

Hence we can conclude that the Arrhenius plot will produce the conversion energy from cubic to hexagonal ice (figure 5.20). The slope of the fitted line through the data points corresponds to a conversion energy of about 47 kJ/mol. The ageing effects for different ice thicknesses but constant temperature of 198 K are presented in figure 5.21. The measured data have been fitted using the parcel model. Water vapour for 198 K has been taken 0.2 Pa (NIST Webbook, 2005). As variable we used crystals edge for cubic crystals. The result values of the fit shown in fig 5.20 are 7, 8.8 and 15 μm for ice coating time of 6, 15 and 60 minutes, respectively.

The measured surface concentrations $c_s(l_c)$ and theoretical fits for RLT=0 for the three different coating times (ice thicknesses) are shifted according to the size (edge) of cubic ice crystals.

5.5. Sensitivity of the thermodynamic fits

The thermodynamic fits are made by plotting a regression line through the data points corresponding to equilibrium conditions. The adsorption isotherms in this chapter were fitted by applying the Langmuir adsorption / desorption theory, respectively, for adsorption on one and two different adsorption sites. The fit was done by varying the equilibrium Langmuir constant and the maximal number of active surface sites. The result is c_s versus c_g. In this chapter we show the reliability of the fits by testing the sensitivity of the parameters that have been varied. For simplicity, the Langmuir model which accounts for adsorption on one type surface sites has been chosen.
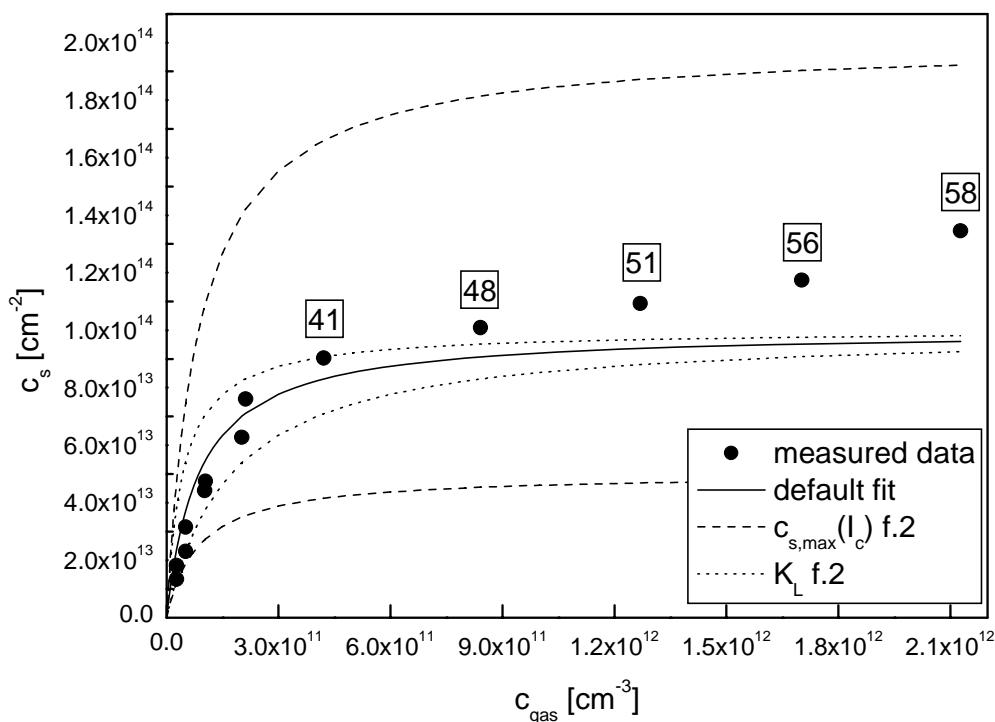
Figure 5.22. Sensitivity tests and measurements at 193 K.

The figure shows the sensitivity of the parameters Langmuir constant (K_L) and maximum surface coverage ($c_{s,max}(I_C)$) for cubic ice. The default fit (the bold line) is the best fit through the data points (the black dots). Four additional simulations have been performed by varying K_L by a factor a 2 (the dotted lines) and $c_{s,max}(I_C)$ by a factor of 2 (the dashed lines). The numbers in the squares show the RLT for each of the measurements taken. As can be seen the discrepancies between the default (the best) fit and measured data increase with increasing gas phase concentration. Varying the parameters by a factor of 2 shows that they are clearly distinguishable. Hence the thermodynamic fits and extracted parameters like K_L and $c_{s,max}$ are reliable within the experimental error.

6. Error analysis

To estimate the errors and the reliability of the final results and the conclusions the scheme presented in the next figure was used. In this chapter the errors and inaccuracy will be shown and discussed for each step of the present study.
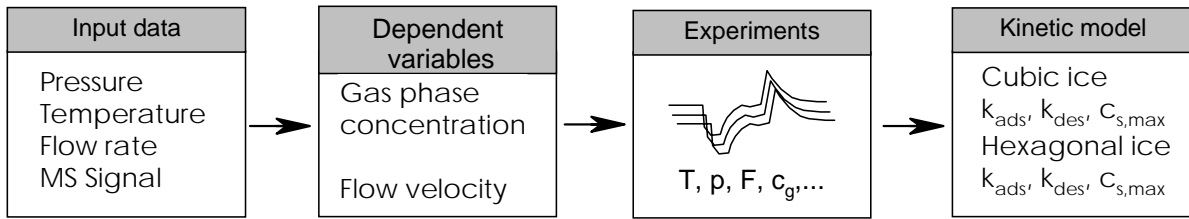
Figure 6.1. A typical block scheme of the experiments

The input parameters (Input data) include the measurable quantities. Each of them has a statistical error of about 1% reported from the manufacturer. The measured values were respectively the pressure of the reactor (p [mbar]), the pressure of the substance in the flask (p_b [mbar]), the total pressure of the bottle (p_t [mbar]), injector flow (F_i [sccm]), carrier gas flow (F_c [sccm]) and the temperature of the reactor (T [K]). The complete set of measured equipment was calibrated and further systematical errors will not be taken into account nor discussed in this chapter.

The inaccuracy of the calculated gas phase concentration and flow velocity can be given by the following two equations for the gas phase concentration:

$$\Delta c_g = \left(\frac{dc_g}{dp}\right)\Delta p + \left(\frac{dc_g}{dp_b}\right)\Delta p_b + \left(\frac{dc_g}{dp_t}\right)\Delta p_t + \left(\frac{dc_g}{dF_i}\right)\Delta F_i + \left(\frac{dc_g}{dF_c}\right)\Delta F_c + \left(\frac{dc_g}{dT}\right)\Delta T$$

and the flow velocity:

$$\Delta v_{flow} = \left(\frac{dv_{flow}}{dp}\right)\Delta p + \left(\frac{dv_{flow}}{dT}\right)\Delta T + \left(\frac{dv_{flow}}{dF_i}\right)\Delta F_i + \left(\frac{dv_{flow}}{dF_c}\right)\Delta F_c$$

where the single statistical errors Δ are multiplied by the first derivation of the equation for c_g, and respectively v_{flow} discussed in chapter 3. Calculated

intervals of indefiniteness are for Δc_g = 10% and for v_{flow} less than 2%. In order to estimate how much the c_g error influence the observed signal a simulation at 200K has been performed, and gas phase concentration 2 ($\pm$10%) 10^{11} cm^{-3} (figure 6.2).
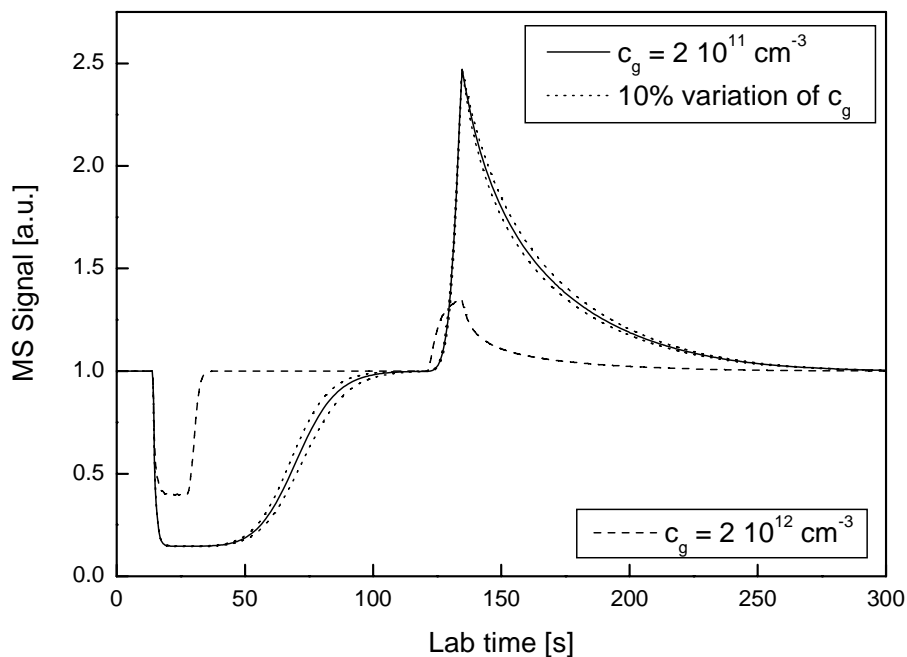
Figure 6.2. A simulation at T=200K, and c_g=2 10^{11} cm^{-3} (the bold line). The dotted accounts the change of the observed signal when the gas concentration is varied with 10%. The dashed line is simulation for on order higher gas concentration.

As can be seen the 10% errorbar in the gas phase concentration leads to insignificant change of the resulting signal. The change of the surface concentration concerning the c_g change of 10% is about 5% according to figure 6.2.

The third stage is the one where experiments were carried out. For the present work nearly 2000 single measurements were taken and more than 1000 were analyzed and fitted with the kinetic model. However it must be noted that the adsorption/desorption areas for experiments at high gas phase concentration or high temperature were relatively smaller (figure 6.2 – dashed line). Such are most of the conditions for describing the processes affecting adsorption on hexagonal sites.

Fitting the adsorption and desorption slopes (slope 1 and slope 2) is more inexact compared to the cubic sites, therefore reported values (such as $k_{ads}(I_h)$, $k_{des}(I_h)$ and $c_{s,max}(I_h)$) are comparatively more inaccurate than those for I_c. Considering these values and error intervals, at last desorption energies are derivable kinetically from Arrhenius by the equation:

$$\Delta H_{ads} = -T \ln(k_{des})$$

and thermodynamically from Van t'Hoffs plot:

$$\Delta H_{ads} = -T \ln(K_L)$$

where the energetic barrier ΔH_{ads} is described in chapter 5.3.

7. Discussions and comparison with literature data

Acetone adsorption on ice has been investigated in two directions: experimentally and theoretically. The results of the different experimental techniques such as coated wall flow tubes (CWFT) (Behr et al., 2003; Behr et al., 2004; Peybernes et al., 2004; Winkler et al., 2002), chromatography (Bartels-Rausch et al., 2004; Bartels-Rausch et al., 2005; Guimbaud et al., 2003), Knudsen cells (Hudson et al., 2002) and volumetric methods (Domine and Rey-Hanot, 2002) together with some theoretical studies using quantum chemical and molecular dynamical approaches (Girardet and Toubin, 2001; Marinelli and Allouche, 2001; Picaud and Hoang, 2000; Picaud et al., 2000) are summarized in table 7.1 with respect to adsorption enthalpies (ΔH_{ads}) and the maximum numbers of adsorption sites ($c_{s,max}$). The most important fact to note from this table is the inconsistency/variability of the enthalpy of adsorption which differs by almost a factor of two between the different studies. Since this quantity reflects the energy change upon interaction of gas phase acetone with an ice surface it will depend on a number of parameters (surface coverage, surface morphology and porosity, surface crystallographic phases and imperfections), none of which can be considered as genuinely invariant between these studies. Moreover, since there is no easy method or technique available by which such variations could be quantified or controlled the comparison between these results can at best be qualitative. Nevertheless, one of the experimental parameters which can be reasonably well controlled is surface coverage. As seen from table 7.1 most of the experiments performed at low surface coverages (0.01 % < θ < 7%) yield "high" values of adsorption enthalpies in the order of -50 ± 6 kJ/mol. This is consistent with the value obtained in the present work for a fresh ice surface and a low gas phase concentration (< 10^{11} cm^{-3}) and which is attributed to adsorption on cubic ice. Similarly high values of ΔH_{ads} were also obtained in a series of chromatographic studies using different ice

(polycrystalline, single crystal) and snow samples (Bartels-Rausch et al., 2004). Although the experiments were performed on ice samples of different origin and thermal history, preferred adsorption on dislocations and imperfections on the ice surfaces cannot be excluded.

T / K	ΔH_{ads} / kJ mol^{-1}	$c_{s,max}$ / 10^{14} cm^{-2}	Technique
0	-31,2[d]		Ab initio
	-53,4[e]		
0	-49	2,45	MD
50	-46,3	2,45	MD
150	-41,8	2,45	
175	-38,9	1,27	
Average	-43,8[c]		Semi
193-213	-55 ± 7	-	Volumetric
198-223	-46 ± 7	2,7 ± 0,7	CWFT
190-223	-43,7 ± 7,9	14g	CWFT
193-223	-48,1 ± 3,1	1,37 ± 0,13	CWFT/Langmuir
193-223	-50,3 ± 2,5	1,30 ± 0,18	CWFT/BET
203-223	-46 ± 3	< 5%[f]	CWFT
205-243	-54,4 ± 7,6[i] -56,0 ± 2,8[j]	< 5%[f]	Chromatography
198-223	-52[c]	0,1-6%[f]	Chromatography
130-180 K	-35 ± 2[a]	100%[f]	TD
	-40 ± 2[b]	100%[f,h]	
190-220 K	-49±3	≤ 1[g,h]	CWFT
	-32±6	6g	

Table 7.1. Summary of literature studies for the adsorption enthalpies (H_{ads}) and maximum umber of surface sites ($c_{s,max}$) for the adsorption of acetone on ice surfaces.

α State. β State. Average value (4 diff. types of ice). Adsorption on a non defective surface. Adsorption on a defective surface. Value obtained at this % of the full surface coverage (2.5 10^{14} [cm^{-2}]) Adsorption capacity depends on ice mass. Annealing reduces adsorption capacity. Ice spheres. Aged snow. CWFT: Coated Wall Flow Tube. TD: Thermal Desorption. MD: Molecular Dynamic

Ageing effects, however, have not been reported. From more systematic investigations of the dependence of ΔH_{ads} on the extent of surface coverage Crowley's group (Winkler et al., 2002) suggest a systematic trend to decreasing values of ΔH_{ads} for increasing coverages even below total surface coverages of 0.07%. This trend could easily be reconciled if coverages were approaching or even exceeding a monolayer. They are difficult to understand though if surface coverages are extremely low and in a range where consecutive adsorption events do not influence each other energetically. In contrast to all other experimental techniques Knudsen cell experiments by Tolbert's group (Hudson et al., 2002) produce a much lower value for the enthalpy of adsorption (ΔH°_{ads} = - 28 ± 7 kJ). This is difficult to explain solely on the basis of surface coverages since Knudsen cells operate by definition at very low concentrations and coverages.

In the present investigation a "low" value for the adsorption enthalpy was obtained for an aged ice surface which accounts the adsorption of acetone on ice with hexagonal structure. This finding is in agreement with a theoretically predicted result for the adsorption of acetone on a proton ordered ice surface (Marinelli and Allouche, 2001). Moreover, direct observations of the molecular surface structure under experimental conditions similar to those described by Hudson et al. support the assumption, that the value of ΔH°_{ads} = - 28 ± 7 kJ was measured on a ordered hexagonal ice surface. This structure has a "full-bilayer termination", meaning that molecules in the outer layer are bound to the three molecules in the layer below and have just one dangling bond pointing outward, the typical termination of the

upper surface of the hexagonal ice structure (Braun, 1998; Materer et al., 1997).

Further evidence for the energetic and structural details of gas phase acetone interacting with an ice surface has been obtained from MD calculations. From investigations of this interaction on proton-ordered ice at 0 K Girardet's group (Picaud et al., 2000) found that under these conditions acetone forms an ordered layer on the ice surface with 2 molecules of acetone per surface unit cell of ice. Hence a monolayer of acetone on ice was found to consist of $2.45 \cdot 10^{14}$ cm^{-2}, adsorbed with an energy ΔU_{ads} = - 49 kJ/mol. Using the same approach, Picaud and Hoang (Picaud and Hoang, 2000) performed calculations at temperatures between 50 and 150 K, whereupon ΔU_{ads} was found to decrease to -46.3 kJ/mol and -41.8 kJ/mol at 50 and 150 K, respectively. The temperature dependence of the adsorption enthalpy was assigned to the increasing flexibility of the surface molecules with increasing temperature. As opposed to MD calculations ab initio calculations as performed by Marinelli and Allouche (Marinelli and Allouche, 2001), indicate quite different adsorption enthalpies with -53,4 kJ/mol for the adsorption on molecular defects on the ice surface in comparison to -31.2 kJ/mol on proton ordered hexagonal ice.

In summary, whilst the majority of experiments performed at low coverages, including our own, produce a high value of the adsorption enthalpy, there is also experimental evidence for lower values. The theoretical results indicate high values only in the presence of surface imperfections whilst lower values correspond to adsorption on perfectly ordered hexagonal structures. Except for our own work ageing effects have as yet not been reported.

A further inconsistency in the literature data of table 7.1 is the maximum surface coverage $c_{s,max}$ for which values between $1.3 \cdot 10^{14}$ to $1.4 \cdot 10^{15}$ cm^{-2} have been found. From gas phase vapour deposition under our experimental conditions and for a coating time in the order of one hour a total number of active surfaces sites in the order of about $1 \cdot 10^{15}$ cm-2 is found in our present experiments. This is in agreement with the ESEM and BET studies of Keyser and Leu (Keyser and Leu, 1993) and Leu et al. (Leu et al., 1997a) and a previous

value from our group (Behr et al., 2003). As opposed to these results all experiments performed on frozen liquid water films produced much lower maximum numbers of active surface sites. This difference is most likely due to surface morphology for which vapour deposition produces a larger roughness and hence larger specific surface areas.

A major finding of the present work is the effect of ageing of the adsorption capacity. When generating ice films from the condensation of water vapour at low temperatures ($\leq$ 200 K) cubic ice seems to be the preferentially formed ice modification (Hobbs, 1974; Keyser and Leu, 1993). Moreover, there is evidence from a number of other observations that I_c forms easily at lower temperatures. For instance, supercooled water preferentially freezes to cubic ice at sufficiently cold temperatures (Huang and Bartell, 1995). Clusters of 4000–6000 water molecules have been shown to nucleate exclusively to Ic when cooled by evaporation to 200 K (Huang and Bartell, 1995). Rapid quenching of 3 μm droplets on a cryoplate led to Ic at 190 K but to Ih at 200 K (Mayer, 1987). However, cubic ice is a metastable phase which tends to transform into the thermodynamically stable hexagonal phase on a time scale of several 10 minutes at temperatures around 200 K (Chaix et al., 1998; Davy and Somorjai, 1971; Keyser and Leu, 1993; Dowell and Rinfret, 1960; Kumai, 1968).

Different adsorption behaviour of acetone on ice surfaces depending on the thermal history of the ice has previously been observed in thermal desorption (TPD) experiments under ultrahigh vacuum (UHV) conditions (Schaff and Roberts, 1994; Schaff and Roberts, 1996; Schaff and Roberts, 1998). From the preparation of thin ice films (10-100 monolayers) by condensation of water vapour onto the cold (90-130 K) metal substrate two desorption peaks of acetone at 140 and 157 K, designated α- and β-acetone, respectively, were observed during TPD. Assuming first-order desorption kinetics and frequency factors of 10^{13} s^{-1} (Yates, 1985) the corresponding activation energies were approximately 35 and 40 kJ mol^{-1}, respectively. Annealing of the ice surface leads to irreversible change of the desorption behaviour for which only the lower temperature state (α-acetone) was observed, very much in agreement

with the present findings on the kinetics of acetone adsorption under surface ageing conditions. These authors, however, differ from us in assigning the higher temperature desorbing ß-acetone to correspond to an adsorption on amorphous ice rather than cubic ice. Whilst the existence of a thermally metastable cubic ice phase has i.e. been suggested from electron microscopy and electron diffraction studies (Kumai, 1968) other observations favour the existence of amorphous ice at temperatures below 140 K (Burton, 1935). IR-spectroscopic studies performed by Schaff and Roberts (Schaff and Roberts, 1994; Schaff and Roberts, 1996; Schaff and Roberts, 1998) also indicated differences in the surface chemical structure of the two ice phases. Experiments reported by Chaix et al. (Chaix et al., 1998) for the adsorption of D_2O on ice suggest that both the method of preparation and the thermal history of the ice sample influence the morphology and the microstructure of the sample and hence its adsorption kinetics. For instance, it was found that the annealing of cubic ice, prepared by condensing water vapour at 140 K, reduces the γ value for adsorption of D_2O irreversibly by a factor of two.

As discussed in the above sections of this work we suggest that the observed ageing behaviour of our ice films, as noted at lower temperatures, is caused by a change of the crystallographic phase of available surface sites, namely from cubic to hexagonal. Any other explanation for the observed ageing effect, i.e. a change of surface topography or morphology, is left unconsidered, albeit not unlikely. Moreover, since we have no direct evidence for the assumed crystallographic change we have attempted to relate our observations to other evidence reported in the literature (Dowell and Rinfret, 1960; Murphy, 2003).

One of the more significant and characteristic observations of cubic to hexagonal ice conversions that have been reported is the rate of change and its temperature dependence (Bertie et al., 1963; Dowell and Rinfret, 1960). Measurements in the temperature range 160 – 220 K indicate activation energies in the order of 34 kJ/mol and characteristic times between 104 and 10 min (Dowell and Rinfret, 1960). This is very much consistent with the findings of the present work and therefore lends

independent support for our conclusions. Formation of metastable cubic ice and its subsequent thermal conversion into stable hexagonal ice is supposed to occur because the rate of surface reconstruction to a structure of lower potential energy is slow in comparison to the rate of condensation. In addition, cubic ice may have a more energetic and reactive surface with highly irregular surface structure and a substantial fraction of incompletely coordinated surface water molecules. Indeed computer simulation suggest significant modification of the ice surface structure with respect to the cubic crystalline interior, toward loss of lateral order at 200 K (Devlin and Buch, 1995). During annealing a transition of the ice structure from cubic to hexagonal is expected (Dowell and Rinfret, 1960; Murphy, 2003).

The next figure represents a literature comparison for the temperature dependent transformation of cubic to hexagonal ice. The dashed line is calculated by first order assumption of I_c to I_h change.
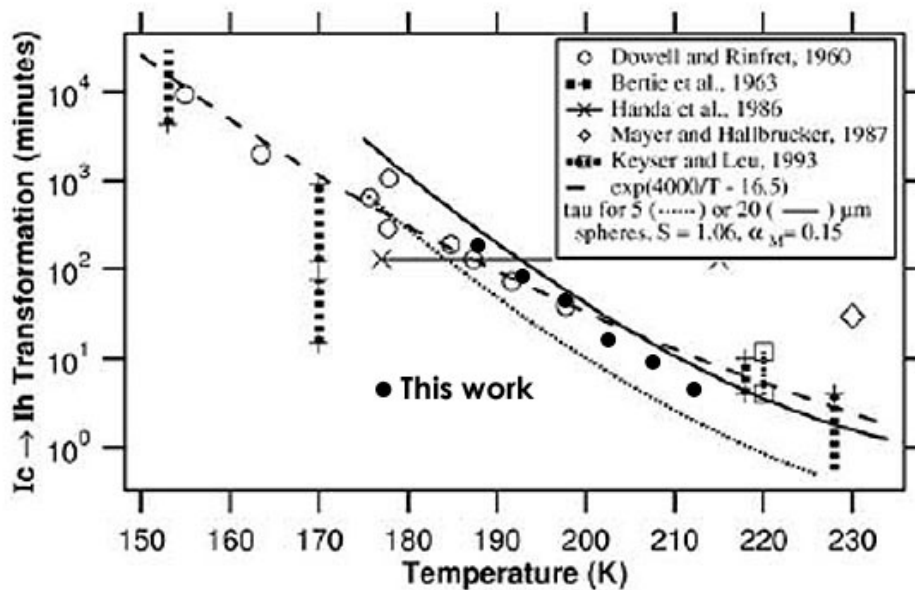
Figure 7.1. Transformation half time of cubic to hexagonal ice (Murphy, 2003).

The points on the figure express the half life time of cubic to hexagonal sites transformation. The two dotted and bold lines were calculated by edges of the cubic crystal, of 5 and 20 μm, respectively. The black dots present calculated (chapter 5.4.2) points of our work with cubic crystals size of 15 μm i.e. ice thickness corresponds to a coating time of about 1 hour.

The results of our study have not unravelled all of the discrepancies / inconsistencies in the set of available literature studies on the adsorption behaviour of acetone on ice surfaces. These discrepancies are thought to be jointly caused by insufficient experimental control over parameters such as surface morphology, total available surface area, number of active adsorption sites, crystallographic phases and their imperfections etc.

8. Summary of numerical results

The results in table 8.1 present our kinetic rate coefficient as calculated adsorption from the application of a kinetic model for acetone on ice. The activation energy for desorption is also presented for both cubic and hexagonal sites, calculated form the Arrhenius dependence of $\ln(k_{des})$ versus $1/T$.

	Cubic Ice		Hexagonal Ice	
T	k_{des} / s^{-1}	$k_{ads} / 10^{-13} \, cm^3 s^{-1}$	k_{des} / s^{-1}	$k_{ads} / 10^{-14} \, cm^3 s^{-1}$
193	0.04	5.30	-	-
198	0.09	5.37	0.31	4.03
203	0.18	5.44	0.55	4.08
208	0.39	5.50	0.64	4.13
213	0.67	5.57	1.08	4.18
218	-	-	1.66	4.22
γ	$(8\pm1) \, 10^{-2}$		$(6\pm1) \, 10^{-3}$	
	$E_{act, \, des} / kJ \, mol^{-1}$		$E_{act, \, des} / kJ \, mol^{-1}$	
	48 ± 3		29 ± 6	

Table 8.1. Summary of kinetic rate coefficients for the interaction of acetone (adsorption, desorption) with ice surfaces in the temperature range T = 193 – 218 K differentiated for cubic (I_c) and hexagonal (I_h) ice.

	Cubic Ice		Hexagonal Ice	
	$K_L / 10^{-12} \, cm^3$ (Th)	$K_L / 10^{-12} \, cm^3$ (Km)	$K_L / 10^{-14} \, cm^3$ (Th)	$K_L / 10^{-14} \, cm^3$ (Km)
193	11.6	13.3	-	-
198	6.7	6.0	15.1	13.0
203	3.4	3.0	7.4	7.4
208	1.2	1.4	6.4	6.5
213	0.7	0.8	3.2	3.9
218	-	-	2.5	2.5
	$E_{act} / kJ \, mol^{-1}$ (Th)		$E_{act} / kJ \, mol^{-1}$ (Km)	
	49 ± 3		32 ± 6	
	$c_{s,max} / cm^{-2}$		$c_{s,max} / cm^{-2}$	
	$\leq 1 \, 10^{14}$		$6\pm1 \, 10^{14}$	

Table 8.2. Summary of adsorption constants (KL, $c_{s,max}$) for the interaction of acetone (adsorption, desorption) with ice surfaces in the temperature range T = 193 – 218 K differentiated for cubic (I_c) and hexagonal (I_h) ice. Th = Thermodynamics, Km=Kinetic Model

Table 8.2 summarizes the calculated adsorption constants using both thermodynamical (Th) and kinetic model (Km) with respect to hexagonal and cubic sites.

Table 8.3 presents the calculated lifetimes of cubic to hexagonal ice transformation for an ice thickness corresponding to a coating time of 1 hour.

T [K]	Half time [min]
213	4
208	8
203	17
198	50
193	89
188	178

Table 8.3. Transformation of cubic to hexagonal ice for ice depth corresponding to 1 hour of coating time

9. References

Abbatt, J. P. D., K. D. Beyer, A. F. Fucalaro, J. R. McMahon, P. J. Wooldridge, R. Zhang, M. J. Molina, (1992), "Interaction of HCl Vapor with Water-Ice: Implications for the Stratosphere" J. Geophys. Res. 97, 15819.

Abbatt, J. P. D., (2003), "Interactions of Atmospheric Trace Gases With Ice Surfaces: Adsorption and Reaction", Chem. Rev., 103, 4783-4800.

Arnold, F., J. Schneider, K. Gollinger, H. Schlager, P. Schulte, D. E. Hagen, P. D. Whitefield, P. Vanvelthoven, (1997), "Observation of Upper Tropospheric Sulfur Dioxide- and Acetone-Pollution: Potential Implications for Hydroxyl Radical and Aerosol Formation", Geophys. Res. Lett., 24, 57-60.

Bartels-Rausch, T., C. Guimbaud, H. W. Gaggeler, M. Ammann, (2004), "The Partitioning of Acetone to Different Types of Ice and Snow Between 198 and 223 K", Geophys. Res. Lett., 31.

Bartels-Rausch, T., T. Huthwelker, H. W. Gaggeler, M. Ammann, (2005), "Atmospheric Pressure Coated-Wall Flow-Tube Study of Acetone Adsorption on Ice", J. Phys. Chem. A, 109, 4531-4539.

Batista, E. R. H. Jonsson, (2001), "Diffusion and Island Formation on the Ice Ih Basal Plane Surface", Comput. Mater. Sci., 20, 325-336.

Bedjanian, Y. and Poulet, G. (2003), "Kinetics of Halogen Oxide Radicals in the Stratosphere", Chem. Rev., 103, 4639-4655.

Behr, P., J. R. Morris, M. Antman, B. R. Ringeisen, J. R. Splan, G. M. Nathanson, (2001), "Reaction and Desorption of HCl and HBr Following Collisions With Supercooled Sulfuric Acid", Geophys. Res. Lett., 28, 1961-1964.

Behr, P., U. Scharfenort, A. Terziyski, K. Demiral, R. Zellner, (2003), "Thermodynamics and kinetics of the interaction of acetone and acetic acid with ice surfaces at temperatures between 190-220 K", International Symposium on Combustion and Atmospheric Pollution, 575-578.

Behr, P., A. Terziyski, R. Zellner, (2004), "Reversible Gas Adsorption in Coated Wall Flow Tube Reactors. Model Simulations for Langmuir Kinetics", Z. Phys. Chemie-Int. J. Res. Phys. Chem. Chem. Phys., 218, 1307-1327.

Bertie, J. E, L. D. Calvert, E. Whalley., (1963), "Transformations of ice II, ice III, and ice V at atmospheric pressure", J. Chem. Phys. 38, 840-846. .

Blyth, A. M., H. J. Christian, K. Driscoll, A. M. Gadian, J. Latham, (2001), "Determination of Ice Precipitation Rates and Thunderstorm Anvil Ice Contents From Satellite Observations of Lightning", Atmos. Res., 59, 217-229.

Braun, J., A. Glebov, A. P. Graham, A. Menzel, J. P. Toennies, (1998), "Structure and phonons of the ice surface", Phys. Rev. Lett. 80, 2638-263841.

Burton, E. F., W. F. Oliver, (1935), "The crystal structure of ice at low temperatures", Procedings of the Royal Society, Ser A 153, 166-172.

Chaix, L., H. Van Den Bergh, M. J. Rossi, (1998), "Real-Time Kinetic Measurements of the Condensation and Evaporation of D_2O Molecules on Ice at 140K < T < 220K", J. Phys. Chem. A, 102, 10300-10309.

Cox, R. A., M. A. Fernandez, A. Symington, M. Ullerstam, J. P. D. Abbatt, (2005), "A Kinetic Model for Uptake of HNO_3 and HCL on ice in a Coated Wall Flow System", Phys. Chem. Chem. Phys., 7, 3434-3442.

Crutzen, P. J., J. Lelieveld, (2001), "Human Impacts on Atmospheric Chemisty", Annu. Rev. Earth Planet. Sci., 29, 17-45.

Dankwerts, T., (1951), Faraday Soc. 47, 1014.

Dash, J. G., J. S. Wettlaufer, (2003), "The Surface Physics of Ice in Thunderstorms", Can. J. Phys., 81, 201-207.

Davy, J. G., G. A. Somorjai., (1971), "Studies of the Vaporization Mechanism of Ice Single Crystals", J. Chem. Phys. 55, 3624-3636.

Devlin, J. P., V. Buch, (1995), "Surface of Ice as Viewed From Combined Spectroscopic and Computer Modeling Studies", J. Phys. Chem., 99, 16534-16548.

Domine, F., L. Rey-Hanot, (2002), "Adsorption Isotherms of Acetone on Ice Between 193 and 213 K", Geophys. Res. Lett., 29.

Dowell, L. G., A. P. Rinfret., (1960), Low-Temperature Forms of Ice as Studied by X-RAY Diffraction. Nature 188, 1144-1148.

Duke, C. B., Surface Science, The first 30 years, North Holland, Amsterdam. 1994.

Enright, W. H., K. R. Jackson, S. P. Norsett, P. G. Thomsen, (1986), "Interpolants for Runge-Kutta Formulas", ACM TOMS 12, 193-218.

Ertl, G., "Oscillatory kinetics and spatio-temporal self-organization in reactions at solid surfaces", Science 254, 1750-1755. 1991.

Fahey, D. W., K. K. Kelly, G. V. Ferry, L. R. Poole, J. C. Wilson, D. M. Murphy, R. Loewenstein, K. R. Chan, (1989), "In situ measurements of total reactive nitrogen, total water and aerosols in a polar stratospheric cloud in Antarctica", J. Geophys. Res. 94, 11299-11315.

Farman, J. C., B. J. Gardiner, G. G. Chanklin, (1985), "Large losses of total ozone in Antarctica reveal seasonal ClO_x/NO_x interaction", Nature 315, 207-210.

Fehlberg, E., (1970), „Klassische Runge-Kutta-Formeln vierter und niedrigerer Ordnung mit Schrittweiten-Kontrolle und ihre Anwendung auf Waermeleitungsprobleme", Computing 6, 61-71.

Forsythe, G. E., M. A. Malcolm, C. B. Moler, (1977), "Computer Methods for Mathematical Computations", Prentice Hall, Englewood Cliffs, NJ.

Galashev, A. E., G. L. Pozharskaya, V. N. Chukanov, (2002), "Physicochemical Properties of Water Clusters in the Presence of Hcl and Hf Molecules. Molecular Dynamic Simulation", J. Struct. Chem., 43, 458-466.

Gierens, K. (2003), "On the Transition Between Heterogeneous and Homogeneous Freezing", Atmos. Chem. Phys., 3, 437-446.

Girardet, C. and C. Toubin, (2001), "Molecular Atmospheric Pollutant Adsorption on Ice: a Theoretical Survey", Surf. Sci. Rep., 44, 163-238.

Gleitsmann, G. and R. Zellner, (1998), "The Effects of Ambient Temperature and Relative Humidity on Particle Formation in the Jet Regime of Commercial Aircrafts: a Modelling Study", Atmos. Env., 32, 3079-3087.

Golden, D. M., G. N. Spokes, and S. W. Benson, (1973), "Pyrolyse bei sehr kleinem Druck (VLPP); eine vielseitige kinetische Methode", Angewandte Chemie 85, 602–614.

Grassian, V. H., (2001), "Heterogeneous uptake and reaction of nitrogen oxides and volatile organic compounds on the surface of atmospheric particles including oxides, carbonates, soot and mineral dust: implications for the chemical balance of the troposphere", Int. Rev. Phys. Chem 20, 467-548.

Groen, J. C., L. A. A. Peffer, J. Perez-Ramirez, (2003), "Pore size determination in modified micro- and mesoporous materials. Pitfalls and limitations in gas adsorption data analysis", Mirco. and Meso. Mat. 60, 1-17.

Guimbaud, C., T. Bartels-Rausch, M. Ammann, (2003), "An Atmospheric Pressure Chemical Ionization Mass Spectrometer (Apci-Ms) Combined With a Chromatographic Technique to Measure the Adsorption Enthalpy of Acetone on Ice", Int. J. Mass Spectrom., 226, 279-290.

Hanson, D. R., A. R. Ravishankara, (1992), Investigation of the reactive and nonreactive processes involving $ClONO_2$ and HCl on water and nitric acid doped ice. J. Phys. Chem. 96, 2682-2691.

Hobbs, P. V., (1974), Ice Physics. Clarendon Press, Oxford, 44-60.

Howard, C. J., (1979), Kinetic Measurements using Flow Tubes. J. Phys. Chem 83, 3-9. .

Huang, J. F., L. S. Bartell, (1995), "Kinetics of Homogeneous Nucleation in the Freezing of Large Water Clusters", J. Phys. Chem., 99, 3924-3931.

Hudson, P. K., M. A. Zondlo, M. A. Tolbert, (2002), "The Interaction of Methanol, Acetone, and Acetaldehyde With Ice and Nitric Acid-Doped Ice: Implications for Cirrus Clouds", J. Phys. Chem. A, 106, 2882-2888.

Ikeda-Fukazawa, T., S. Horikawa, T. Hondoh, K. Kawamura, (2002), "Molecular Dynamics Studies of Molecular Diffusion in Ice Ih", J. Chem. Phys., 117, 3886-3896.

Isakson, M. J., G. O. Sitz, (1999), "Adsorption and Desorption of Hcl on Ice", J. Phys. Chem. A, 103, 2044-2049.

Jaegle, L., D. J. Jacob, W. H. Brune, P. O. Wennberg, (2001), "Chemistry of HO_x radicals in the upper troposphere", Atmos. Env. 35, 469.

Journet, E., S. Le Calve, P. Mirabel, (2005), "Adsorption Study of Acetone on Acid-Doped Ice Surfaces Between 203 and 233 K", J. Phys. Chem. B, 109, 14112-14117.

Keyser, L. F. and M. T. Leu, (1993), "Morphology of Nitric-Acid and Water Ice Films", Microsc. Res. Tech., 25, 434-438.

Klassen, J. K., K. M. Fiehrer, G. M. Nathanson, (1997), "Collisions of Organic Molecules With Concentrated Sulfuric Acid: Scattering, Trapping, and Desorption", J. Phys. Chem. B, 101, 9098-9106.

Kolb, C. E., D. R. Worsnop, M. S. Zahniser, P. Davidovits, L. F. Keyser, M. T. Leu, M. J. Molina, D. R. Hanson, A. R. Ravishankara, L. R. Williams, M. A. Tolbert, (1995), "Laboratory Studies of Atmospheric Heterogeneous Chemistry, In Progress and problems in atmospheric chemistry", Barker J. R., Ed., Advanced Series in Physical Chemistry 3, World Scientific: River Edge, NJ, 771.

Kumai, M., (1968), "Hexagonal and Cubic Ice at Low Temperatures", J. Glaciol. 7.

Larsen, N., S. H. Svendsen, B. M. Knudsen, C. Voigt, C. Weisser, A. Kohlmann, J. Schreiner, K. Mauersberger, T. Deshler, C. Kroger, J. M. Rosen, N. T. Kjome, A. Adriani, F. Cairo, G. Di Donfrancesco, J. Ovarlez, H. Ovarlez, A. Dornbrack, T. Birner, (2002), "Microphysical Mesoscale Simulations of Polar Stratospheric Cloud Formation Constrained by in Situ Measurements of Chemical and Optical Cloud Properties", J. Geophys. Res. -Atmos., 107.

Lass, K., M. Binetti, O. Weisse, C. Wesenberg, E. Hasselbrink, (2004), "Evidence for oxygen abstraction from NO2 upon thermal scattering from an Al(111) surface", Applied Physics A-Materials Science & Processing 78, 201-204.

Lelieveld, J., A. Bregman, H. A. Scheeren, J. Strom, K. S. Carslaw, H. Fischer, P. C. Siegmund, F. Arnold, (1999), "Chlorine Activation and Ozone Destruction in the Northern Lowermost Stratosphere", J. Geophys. Res. -Atmos., 104, 8201-8213.

Leu, M. T., L. F. Keyser, R. S. Timonen, (1997a), "Morphology and Surface Areas of Thin Ice Films", J. Phys. Chem. B, 101, 6259-6262.

Leu, M. T., R. S. Timonen, L. F. Keyser, (1997b), "Kinetics of the Heterogeneous Reaction $HNO_3(g)+NaBr(s)<->HBr(g)+NaNO3(s)$", J. Phys. Chem. A, 101, 278-282.

Liang, T. Chu, M. T. Leu, L. F. Keyser, (1993), "Uptake of HCl in Water Ice and Nitric Acid Ice Films", J. Phys. Chem. 97, 7779-7785.

Livingston, F. E., S. M. George, (2001), "Diffusion Kinetics of Hc1 Hydrates in Ice Measured Using Infrared Laser Resonant Desorption Depth-Profiling", J. Phys. Chem. A, 105, 5155-5164.

Livingston, F. E., J. A. Smith, S. M. George, (2002), "General Trends for Bulk Diffusion in Ice and Surface Diffusion on Ice", J. Phys. Chem. A, 106, 6309-6318.

Livingston, F. E., G. C. Whipple, S. M. George, (1998), "Surface and Bulk Diffusion of Hdo on Ultrathin Single-Crystal Ice Multilayers on Ru(001)", J. Chem. Phys., 108, 2197-2207.

Lorenzen-Schmidt, H., S. Wessel, W. Unold, S. Solberg, , H. Gernandt, F. Stordal, U. Platt, (1998), "Ozone Measurements in the European Arctic During the Arctoc 1995 Campaign", Tellus Ser. B-Chem. Phys. Meteorol., 50, 416-429.

Marinelli, F., A. Allouche, (2001), "An Ab Initio Study of Acetone and Formaldehyde Monolayers Adsorbed on Ice", Chem. Phys., 272, 137-147.

Marx, D. J. H., (2000), "Modern methods and algorithms of quantum chemistry", J. Grotendorst (Ed.) Publications of the John von Neumann Institute for Computing (NIC), NIC Series, Juelich 1.

Materer, N., U. Starke, A. Barbieri, M. A. Vanhove, G. A. Somorjai, G. J. Kroes, C. Minot, (1997), "Molecular Surface Structure of Ice(0001): Dynamical Low-Energy Electron Diffraction, Total-Energy Calculations and Molecular Dynamics Simulations", Surf. Sci., 381, 190-210.

Mayer, E., A. Hallbrucker., (1987), "Cubic ice from liquid water", Nature 325, 601– 602.

McCarty, R. D., V. D. Arp, (1990), "A New Wide Range Equation of State for Helium", Adv. Cryo. Eng. 35, 1465-1475. .

Mckeen, S. A., T. Gierczak, J. B. Burkholder, P. O. Wennberg, T. F. Hanisco, E. R. Keim, R. S. Gao, S. C. Liu, A. R. Ravishankara, D. W. Fahey, (1997), "The Photochemistry of Acetone in the Upper Troposphere: a Source of Odd-Hydrogen Radicals", Geophys. Res. Lett., 24, 3177-3180.

Morris, J. R., P. Behr, M. D. Antman, B. R. Ringeisen, J. Splan, G. M. Nathanson, (2000), "Molecular Beam Scattering From Supercooled Sulfuric Acid: Collisions of HCl, HBr, and HNO_3 With 70 Wt % D_2SO_4", J. Phys. Chem. A, 104, 6738-6751.

Murphy, D. M. (2003), "Dehydration in Cold Clouds Is Enhanced by a Transition From Cubic to Hexagonal Ice", Geophys. Res. Lett., 30.

Nathanson, G. M., P. Davidovits, D. R. Worsnop, C. E. Kolb, (1996), "Dynamics and Kinetics at the Gas-Liquid Interface", J. Phys. Chem., 100, 13007-13020.

NIST Chemistry WebBook, (2005), . http://webbook. nist. gov/chemistry.

Petrenko, V. F., R. W. Whitworth., (1999), Physics of Ice. Oxford University Press.

Peybernes, N., C. Marchand, S. Le Calve, P. Mirabel, (2004), "Adsorption Studies of Acetone and 2, 3-Butanedione on Ice Surfaces Between 193 and 223 K", Phys. Chem. Chem. Phys., 6, 1277-1284.

Picaud, S., P. N. M. Hoang, (2000), "Adsorption of Acetone Molecules on Proton Ordered Ice. A Molecular Dynamics Study", J. Chem. Phys., 112, 9898-9908.

Picaud, S., C. Toubin, C. Girardet, (2000), "Monolayers of Acetone and Methanol Molecules on Ice", Surf. Sci., 454, 178-182.

Platt, U., G. Honninger, (2003), "The Role of Halogen Species in the Troposphere", Chemosphere, 52, 325-338.

Pruppacher, H. R., J. D. Klett, (1996), "Microphysics of Clouds and Precipitation", Atmospheric and Oceanographic Sciences Library, Vol 18, Kluwer Academic Pub.

Reid, R. C., J. M. Prausnitz, B. E. Poling, (1987), "The properties of gases and liquids, 4. ed.", New York [u.a.].

Reinhardt, H., M. Fida, R. Zellner, (2003), "DRIFTS-studies of the interactions of HNO_3 with ice and HCl-(HNO_3)-hydrate surfaces at temperatures around 165 K", J. Molec. Struc. 661, 567-577.

Rudich, Y., R. K. Talukdar, T. Imamura, R. W. Fox, A. R. Ravishankara, (1996), "Uptake of NO_3 on KI solutions: Rate coefficient for the NO_3 reaction and gas-phase diffusion coefficients for NO_3", Chem. Phys. Lett. 261, 467-473.

Schaff, J. E., J. T. Roberts, (1994), "Structure Sensitivity in the Surface-Chemistry of Ice - Acetone Adsorption on Amorphous and Crystalline Ice Films", J. Phys. Chem., 98, 6900-6902.

Schaff, J. E., J. T. Roberts, (1996), "Toward an Understanding of the Surface Chemical Properties of Ice: Differences Between the Amorphous and Crystalline Surfaces", J. Phys. Chem., 100, 14151-14160.

Schaff, J. E., J. T. Roberts, (1998), "The Adsorption of Acetone on Thin Films of Amorphous and Crystalline Ice", Langmuir, 14, 1478-1486.

Van Bramer, S. E., (1998), "An Introduction to Mass Spectrometry", Department of Chemistry, Widener University.

Seinfeld, J. H., S. N. Pandis, (1998), "Atmosperic chemistry and physics: From air pollution to climate change", John Wiley & Sons, Inc. (USA).

Shampine, L. F., R. M. Corless, (2000), "Initial Value Problems for ODEs in Problem Solving Environments", J. Comp. Appl. Math 125, 31-40. .

Singh, H., Y. Chen, A. Tabazadeh, Y. Fukui, I. Bey, R. Yantosca, D. Jacob, F. Arnold, K. Wohlfrom, E. Atlas, F. Flocke, D. Blake, N. Blake, B. Heikes, J. Snow, R. Talbot, G. Gregory, G. Sachse, S. Vay, Y. Kondo, (2000), "Distribution and Fate of Selected Oxygenated Organic Species in the Troposphere and Lower Stratosphere Over the Atlantic", J. Geophys. Res. -Atmos., 105, 3795-3805.

Slovak, J., H. Tanaka, K. Koga, X. C. Zeng, (2003), "Computer Simulation of Bilayer Ice: Structures and Thermodynamics", Physica a, 319, 163-174.

Sokolov, O., J. P. D. Abbatt, (2002), "Adsorption to ice of n-alcohols (ethanol to 1-hexanol), acetic acid, and hexanal", J. Phys. Chem A 106, 775-782.

Solomon, S. (1999), "Stratospheric Ozone Depletion: a Review of Concepts and History", Rev. Geophys., 37, 275-316.

Toon, O. B., R. P. Turco, J. Jordan, J. Goodman, G. Ferry, (1989), "Physical processes in polar stratospheric ice clouds", J. Geophys. Res. 94, 11359-11380.

Wagner, S., E. P. Röth, R. Zellner, (2004), "Resolution of physical-chemical fundamentals in phase transfer processes". to be published.

Wang, Y., K. Jacobi, G. Ertl, (2003), "Interaction of NO with the stoichiometric RuO_2(110) surface", J. Phys. Chem. B 107, 13918-13924.

Wessel, S., S. Aoki, P. Winkler, R. Weller, A. Herber, H. Gernandt, O. Schrems, (1998), "Tropospheric Ozone Depletion in Polar Regions - a Comparison of Observations in the Arctic and Antarctic", Tellus Ser. B-Chem. Phys. Meteorol., 50, 34-50.

Winkler, A. K., N. S. Holmes, J. N. Crowley, (2002), "Interaction of Methanol, Acetone and Formaldehyde With Ice Surfaces Between 198 and 223 K", Phys. Chem. Chem. Phys., 4, 5270-5275.

Yates, J. T. J., (1985), Methodes Exp. Phys. 22, 425-465.

Zambelli, T., J. V. Barth, J. Wintterlin, G. Ertl, (1997), "Complex pathways in dissociative adsorption of oxygen on platinum", Nature, 390, 495-497.

Zellner, R., (1999), "Chemistry of the Stratosphere, in Global Aspects of Atmospheric Chemistry", Topics in Physical Chemistry, Edited by Baumgärtel H., Grünbein W., Hensel F., Guest Editor Zellner R., Steinkopff / Springer, Darmstadt, 6, 181-247.

Zondlo, M. A., S. B. Barone, M. A. Tolbert, (1998), "Condensed-Phase Products in Heterogeneous Reactions: N_2O_5, $ClONO_2$, and HNO_3 Reacting on Ice Films at 185 K", J. Phys. Chem. A, 102, 5735-5748.

Curriculum vitae

Name	*Atanas Tanov TERZIYSKI*
Born	*October, 04, 1974 in Plovdiv, Bulgaria*
Nationality	*Bulgarian*
Sex	*Male*
Address	*University of Plovdiv*
	Faculty of Chemistry
	Tsar Assen 24, Str
	4000 Plovdiv
	Bulgaria
E-mail	*atanas@uni-plovdiv.bg*
Education	*1981 - 1988 Base Education*
	1988 - 1992 School of mathematics in Plovdiv
	1992 - 1997 University of Plovdiv - Master's degree in chemistry
	1997 – 1998 Army hospital assistant - Military hospital Ruse
	2001 – 2006 A Ph.D. student at the University of Duisburg - Essen
Experience	*Heterogeneous reactions*
	Flow reactors
	Chemometrics and modelling
	MASS, IR, UV/VIS spectroscopy
Computer skills	*Office, Graphical and data analysis applications*
	Programming and Internet design
	Operating systems: Windows, Linux and BSD
	Network administration and management

List of publications

Papers

Kochev, N. T., P. N. Penchev, A. Terziyski, G. N. Andreev, Software Approaches for Structure Information Acquisition and Training of Chemistry Students. Intern. J. Information Theories&Applications, 8(4), 199-206(2001).

Behr, P., U. Scharfenort, A. Terziyski, K. Demiral, R. Zellner, International Symposium on Combustion and Atmospheric Pollution, (2003), 575-578.

Behr, P., A. Terziyski, R. Zellner, Z., Reversible Gas Adsorption in Coated Wall Flow Tube Reactors. Model Simulations for Langmuir Kinetics. Z. Phys. Chem. 218 (2004) 1307

Behr, P., U. Scharfenort, A. Terziyski, R. Zellner, Thermodynamics of the interaction of acetone and acetic acid with ice surfaces at temperatures between 190 and 223 K, Torus-pess (2004)

Terziyski, A, P. Behr, R. Zellner, Modeling of adsorption and desorption processes in coated wall flow tube reactors, Faculty of Chemistry, University of Plovdiv, Scientific Works - Chemistry, vol. 32, book 5, (2004), 31-38

Behr, P., A. Terziyski, R. Zellner, Z., Acetone Adsorption on Ice Surfaces in the Temperature Range T=190-220 K. Evidence for Ageing Effects due to Changes of the Adsorption Sites, J. Phys. Chem. (2006) in print

Conferences

A. Terziyski, P. Behr, U. Scharfenort and R. Zellner, The interaction of acetic acid with ice surfaces at 198-223K,17th International Symposium on Gas Kinetics, Essen (Germany), August (2002)

U. Scharfenort, P. Behr, A. Terziyski and R. Zellner, Heterogeneous interactions of acetone, ethanol and n-propanol with ice surface between 190-250K, 17th International Symposium on Gas Kinetics, Essen (Germany), August (2002)

P. Behr, K. Demiral, U. Scharfenort, A. Terziyski, and R. Zellner, Uptake Kinetics of Oxygenated Organics on Ice Surfaces (HEP), EC / EUROTRAC-2 Joint Workshop "Shaping the Future of Atmospheric Chemistry Research in Europe", 9-11 September, Paris, (2002)

P. Behr, A. Terziyski, U. Scharfenort, K. Demiral und R. Zellner, HeterogeneWechselwirkung von Aceton und Essigsaeure mit Eisoberflaechen, Bunsentagung Meeting, Kiel, Germany, (2003)

P. Behr, U. Scharfenort , A. Terziyski , R. Zellner, Adsorptions/Desorptions-Kinetik von Aceton auf Eisoberfl¨achen bei Temperaturen um 200 K. Experiment und nummerische Simulation., Bunsentagung Meeting, Dresden, Germany, (2004)

P. Behr, U. Scharfenort, A. Terziyski, G.M. Nathanson, R. Zellner, Dynamik der Streuung monoenergetischer HClund HBr-Molekuele an fluessigen Schwefelsaeure/Wasser-Oberflaechen zwischen 213 und 238 K, Bunsentagung Meeting, Frankfurt, Germany, (2005)

A. Terziyski, P. Behr , U. Scharfenort , R. Zellner, Adsorption of Acetone on Ice at Temperatures between 188 and 223 K: Thermodynamic Data and Kinetic Model Simulation, Bunsentagung Meeting, Frankfurt, Germany, (2005)